INDOLENINE – DIBENZOTETRAAZA[14]ANNULENE NICKEL COMPLEXES AS SENSITIZERS FOR DYE – SENSITIZED SOLAR CELLS

ABDUL QAIYUM BIN RAMLE

FACULTY OF SCIENCE
UNIVERSITY OF MALAYA
KUALA LUMPUR

2018

INDOLENINE-DIBENZOTETRAAZA[14]ANNULENE NICKEL COMPLEXES AS SENSITIZERS FOR DYE – SENSITIZED SOLAR CELLS

ABDUL QAIYUM BIN RAMLE

DISSERTATION SUBMITTED IN FULFILMENT
OF THE REQUIREMENTS FOR THE DEGREE OF
MASTER OF SCIENCE

DEPARTMENT OF CHEMISTRY
FACULTY OF SCIENCE
UNIVERSITY OF MALAYA
KUALA LUMPUR

2018

UNIVERSITY OF MALAYA
ORIGINAL LITERARY WORK DECLARATION

Name of Candidate: ABDUL QAIYUM BIN RAMLE

Matric No: SGR150079

Name of Degree: MASTER OF SCIENCE

Title of Thesis: INDOLENINE – DIBENZOTETRAAZA[14]ANNULENE NICKEL COMPLEXES AS SENSITIZERS FOR DYE – SENSITIZED SOLAR CELLS

Field of Study: INORGANIC CHEMISTRY

I do solemnly and sincerely declare that:

(1) I am the sole author/writer of this Work;
(2) This Work is original;
(3) Any use of any work in which copyright exists was done by way of fair dealing and for permitted purposes and any excerpt or extract from, or reference to or reproduction of any copyright work has been disclosed expressly and sufficiently and the title of the Work and its authorship have been acknowledged in this Work;
(4) I do not have any actual knowledge nor do I ought reasonably to know that the making of this work constitutes an infringement of any copyright work;
(5) I hereby assign all and every rights in the copyright to this Work to the University of Malaya ("UM"), who henceforth shall be owner of the copyright in this Work and that any reproduction or use in any form or by any means whatsoever is prohibited without the written consent of UM having been first had and obtained;
(6) I am fully aware that if in the course of making this Work I have infringed any copyright whether intentionally or otherwise, I may be subject to legal action or any other action as may be determined by UM.

Candidate's Signature Date:

Subscribed and solemnly declared before,

Witness's Signature Date:

Name:

Designation: Professor Dr. at the Department of Chemistry, University of Malaya.

INDOLENINE – DIBENZOTETRAAZA[14]ANNULENE NICKEL COMPLEXES AS SENSITIZERS FOR DYE – SENSITIZED SOLAR CELLS

ABSTRACT

A new series of macrocyclic nickel complexes having indolenine and dibenzotetraaza[14]annulene (DBTAA) moieties were synthesized and tested for their application as sensitizers in dye-sensitized solar cells (DSSCs). The structures are furnished with anchoring groups of ethyl ester (**8a**, **8b**, and **8c**) or carboxylic acid (**9c**) on the indolenine moiety and hexyloxy (**8b**) or neopentyloxy (**8c**, **9c**) groups on the DBTAA moiety. The best performance was exhibited by dye **9c**, which under constant AM 1.5G solar simulation (100 mW cm^{-2}) using I^-/I_3^- electrolyte gave a short-circuit current J_{sc} = 0.43 mA cm^{-2}, an open-circuit voltage V_{oc} = 0.41 V and a fill factor FF = 0.528, corresponding to an overall conversion efficiency of η = 0.093%. The dyes **8c** and **9c** were studied by electrochemical impedance spectroscopy (EIS) and incident-photon-to-current-conversion efficiency (IPCE). This is the first investigation of anti-aromatic (4n π-electrons) macrocyclic DBTAA derivatives as sensitizers for DSSCs applications.

Keywords: Indolenine, DBTAA dyes, Anchoring groups, DSSCs.

KOMPLEKS NIKEL INDOLININ – DIBENZOTETRAAZA[14]ANULENA SEBAGAI BAHAN PEMEKAAN UNTUK PEMEKAAN PEWARNA SEL SURIA

ABSTRAK

Satu siri baru kompleks nikel makrosiklik yang mempunyai kumpulan indolinin dan dibenzotetraaza[14]anulena (DBTAA) telah disintesis dan diuji sebagai bahan pemekaan untuk aplikasi Pemekaan Pewarna Sel Suria (DSSCs). Struktur pemekaan telah dilengkapi oleh kumpulan berlabuh ester etil (**8a**, **8b** dan **8c**) atau asid karbosilik (**9c**) pada kumpulan indolenin dan kumpulan heksosil (**8b**) atau neopentosil (**8c**, **9c**) pada DBTAA. Pencapaian terbaik telah ditunjukkan oleh pemekaan **9c**, dibawah stimulasi solar AM 1.5G yang sekata dengan menggunakan I^-/I_3^- sebagai elektrolit telah memberikan aliran litar pendek, J_{sc} = 0.43 mA cm^{-2}, voltan litar buka, V_{oc} = 0.41 V dan faktor isi, FF = 0.528, menunjukkan keseluruhan penukaran kecekapan, η = 0.093%. Pemekaan **8c** dan **9c** telah dikaji dengan spektroskopi impedans elektrokimia (EIS) dan kecekapan penukaran pelanggaran-foton-kepada-aliran (IPCE). Ini adalah kajian pertama makrosiklik anti-aromatik (4n π-elektron) DBTAA sebagai bahan pemekaan untuk aplikasi DSSCs.

Katakunci: Indolinin, Pemekaan DBTAA, Kumpulan berlabuh, DSSCs.

ACKNOWLEDGEMENTS

First and foremost, I would like to express my thankful to the God for giving me opportunities to carry out this project successfully. Special thank goes to my supervisors, Professor Dr. Hapipah Mohd Ali and Professor Dr. Wan Jeffrey Basirun for their invaluable time and inspiring guidance throughout the course of this work.

My sincere thanks are extended to Professor Dr. Abdul Kariem Mohd Arof and his Ph.D student, Muhammad Ammar Mingsukang for their helpful assistance in DSSCs experiments at Department of Physics, Faculty of Science, University of Malaya.

My appreciation is also extended to former Senior Research fellow, Dr Hamid Khaledi, for the X-ray Crystallographic lessons and assistance in solving many experimental problems especially for designing the new sensitizers for DSSCs.

Special thanks to my close friend, Mr Ameerul Hazeeq Hashim, who helped me in theoretical evaluation by performing computational analysis. Besides, I would like to convey my gratefulness to the Ministry of Higher Education for financially supporting me throughout my studies under MyBrainSc scholarship program. I also appreciate the (FRGS Grant FP005-2014) and (PPP Grant PG111-2016A) for funding the project.

Last but not least, I would like to thank my family members and all my friends for their great moral support to accomplish my dissertation.

TABLE OF CONTENTS

LIST OF FIGURES

LIST OF TABLES

LIST OF SYMBOLS AND ABBREVIATIONS

&	:	And
Å	:	Angstrom
$\approx$	:	Approximation
δ	:	Chemical shifts
^{o}	:	Degree
^{o}C	:	Degree celsius
=	:	Equals
>	:	Greater than
<	:	Less than
m	:	Medium
μ	:	Micro
$\neq$	:	Not equal
%	:	Percentage
η	:	Photo-conversion efficiency
s	:	Small
λ	:	Wavelength
w	:	Weak
^{13}C NMR	:	Carbon Nuclear Magnetic Resonance
^{1}H NMR	:	Proton Nuclear Magnetic Resonance
AcOH	:	Acetic acid
Aliquot 336	:	Tri - octylmethylammonium chloride
br	:	Broad
bs	:	Broad small
c	:	Concentration
CB	:	Conduction Band

$CDCl_3$	Deuterated chloroform
CHN	Carbon, Hydrogen, Nitrogen elemental analysis
CHNS/O	Carbon, Hydrogen, Nitrogen, Sulphur / Oxygen elemental analysis
d	Doublet
DCM	Dichloromethane
dd	Doublet of doublet
DFT	Density functional theory
DMF	Dimethylformamide
DSSCs	Dye-sensitized solar cells
EIS	Electron impedance spectroscopy
EtOAc	Ethyl acetate
EtOH	Ethanol
Fc	Ferrocene
FF	Fill factor
FT-IR	Fourier - transform infrared
FTO	Fluorine Tin Oxide
GC	Glassy carbon
H_2SO_4	Sulphuric acid
HCl	Hydrochloric acid
HMBC	Heteronuclear multiple bond correlation
HMPA	Hexamethylphosporamide
HNO_3	Nitric acid
HOMO	Highest occupied molecular orbital
HSQC	Heteronuclear single quantum correlation
Hz	Hertz

IPCE : Incident to Photon Conversion Efficiency

IR : Infrared

J : Coupling constant

J_{sc} : Short-circuit current

K : Kelvin

K_2CO_3 : Potassium carbonate

KI : Potassium iodide

KOH : Potassium hydroxide

LHE : Light - Harvesting Efficiency

LUMO : Lowest Unoccupied Molecular Orbital

m.p : Melting point

$MgSO_4$: Magnesium sulphate

MHz : Megahertz

mL : Milliliter

mM : Millimolar

M_w : Molecular weight

$NaHCO_3$: Sodium hydrogen carbonate

NaOH : Sodium hydroxide

$Ni(OAc)_2.4H_2O$: Nickel(II) acetate tetrahydrate

$POCl_3$: Phosphorus oxychloride

ppm : Parts per million

Pt : Platinum

q : Quartet

quin : Quintet

rpm : Revolutions per minute

s : Singlet

t : Triplet

$TBAPF_6$: Tetrabutylammonium hexafluorophosphate

THF : Tetrahydrofuran

TiO_2 : Titanium dioxide

TLC : Thin layer chromatography

UV-Vis : Ultraviolet - visible spectroscopy

VB : Valence band

V_{oc} : Open - circuit voltage

CHAPTER 1: INTRODUCTION

In view of the increasing demand for energy consumption based on renewable sources and serious global warming issues due to depletion of ozone layer contributed to the production of renewable energy technologies to overcome the problems (Jacobson, 2009). The photovoltaic cell is considered as the best candidate because our Earth is exposed to sunlight radiation throughout the year.

The first solar cell was introduced in the early of 19th century by Edmond Becquerel based on a simple photovoltaic cell using a dilution of AgCl in acidic solution and a Pt plate as the counter electode to generate the voltage and the current (Guarnieri, 2015). However, the energy produced was < 1% and considered very poor. Therefore, many approaches were attempted to improve the cell efficiency. The intensive works on the photovoltaic cell technology began in year 1954 after the first generation of solar cell based - crystalline silicone was successfully developed and found to achieve 6% of power conversion efficiency (Chapin *et al.*, 1954), followed by a continuous work on the modification from the previous structural device components. As a result, the 2nd generation of solar cell of a polycrystalline silicon thin film had shown an impressive improvement on its cell efficiency up to 25% (Green, 2009; Masuko *et al.*, 2014). Owing to its high manufacturing cost, this type of solar cell has not been widely employed as an altenative technology for energy production in spite of its excellent performance and stability. However, an incredible achievement by a 3rd generation of photovoltaic cells based on the small molecules or polymer materials has emerged in the late of 1990s. There are dye - sensitized solar cell (DSSC), organic solar cell, quantum dots solar cell, and perovskite solar cell (Wu *et al.*, 2015). Among them, the DSSC has attracted a considerable attention to be used an alternative and a promising candidate to replace the existing conventional silica-based solar cells compared to other photovoltaic cells. This is because the DSSC requires only cheap material to fabricate the cell and it's exhibits high stability for a long period of time (O'Regan & Grätzel, 1991). Basically, the DSSC is a simple solar cell which is composed of four major components, typically a mesoporous TiO_2, a dye, an electrolyte and a platinized counter electrode all arranged in a sandwich structure (Theerthagiri *et al.*, 2015).

One of the crucial factors affecting the efficiency of the cell is the structure of the dye sensitizer (Ragoussi & Torres, 2015). According to the operating principle, the dye sensitizer must be able to excite electrons from the ground state (HOMO) to the excited state (LUMO), followed by an electron transfer process to the conduction band (CB) of the TiO_2. From the CB, the electrons travel to the counter electrode through external external circuit. The regeneration of electrons in the CB of TiO_2 is through the absorption of sunlight which release photoelectrons from the valence band (Grätzel, 2003).

Today, many intensive research are interested on designing new sensitizers based on the porphyrin derivatives dyes owing to their high photocurrent efficiency (PCE) resulting from excellent light-harvesting property and strong absorption coefficient in the Soret band region (400-500 nm) and moderate absorption coefficient in the Q band region (500-600 nm) (Zhang *et al.*, 2015). The special characteristics of porphyrin with the presence of aromatic conjugation ensures the high efficient electronic transfer process from the donor to the acceptor units (Krishna *et al.*, 2017). In 2014, S. Mathew's and co-workers successfully developed a Zn-porphyrin **SM315** (**Figure 1.1)** and achieved a remarkable photoelectron conversion efficiency (PCE) of more than 13% using $[Co(bpy)_3]^{2+/3+}$ as the redox couple (Mathew *et al.*, 2014). However, the synthesis of porphyrin derivatives is not simple, expensive as it involves multiple-steps routes, requires tedious purification steps and the product yield is usually low (Zwolinski & Eilmes, 2016).

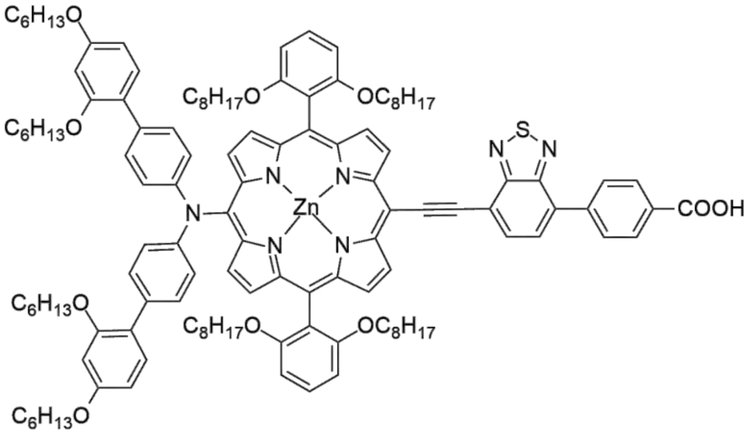

Figure 1.1: Molecular structure of SM315 (Mathew *et al.*, 2014).

One of the most important factors which influences the dye efficiency is the type of the anchoring group. The COOH is the most commonly used of anchoring group due to its strong binding property with metal oxide semiconductor, excellent electron withdrawing ability and superior stability compared to other types of anchoring groups (Zhang & Cole, 2015). Ester groups have also been used as anchoring group which can sensitize TiO_2 through a transesterification process (Sepehrifard *et al.*, 2013), but their binding ability is not straightforward (Kee *et al.*, 2016) and less effective than COOH. However, the efficiency of the cell incorporated with ethyl ester anchoring group can be improved by soaking the TiO_2 photoanode at higher temperature (Sepehrifard *et al.*, 2008).

Practically, most of the planar dye structures have strong tendency to form π-π stacking aggregation (Urbani *et al.*, 2014). To avoid this phenomena, various types of alkyl chains have been used to disrupt the planarity of the dyes as well as to improve the solubility in common solvents (Chen *et al.*, 2015; Magnano *et al.*, 2016). Another strategy to avoid the aggregation is to use co-adsorbents such as chenodeoxycholic acid (CDCA) (Jungsuttiwong *et al.*, 2017), deoxycholic acid (DCA) (Wang *et al.*, 2007) and hexadecylmalonic acid (Wang *et al.*, 2003) as shown in **Figure 1.2**. However, the addition do not always increase the performance of DSSCs and may reduce the amount of dye coverage and injected electrons on the TiO_2 (Ning *et al.*, 2010; Prachumrak *et al.*, 2017; Vinayak *et al.*, 2016; Wan *et al.*, 2012).

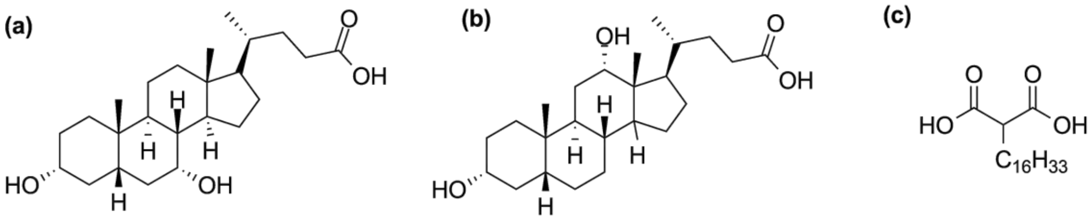

Figure 1.2: Molecular structure of **(a)** CDCA, **(b)** DCA, **(c)** hexadecylmalonic acid.

The present study introduces a new class of sensitizers based on indolenine structures and DBTAA moieties for DSSCs applications. All dyes as depicted in **Figure 1.3** are fully characterized by Nuclear Magnetic Resonance (NMR), Infrared (IR) and elemental analyses. The physical properties of these dyes were investigated with UV-Vis spectroscopy and cyclic voltammetry (CV). Moreover, computational studies using DFT method was performed to investigate the relationship between the electronic distributions of the dyes and their performances. The influence of the linear hexoxyl or the branched neopentoxyl substituents on the macrocyclic system furnished with ethyl ester anchoring group was also investigated towards the overall efficiencies of DSSC. The EIS, IPCE and electron lifetimes of **8c** and **9c** dyes were compared with each other to find out the photo-injection properties associated with different types of anchoring groups of the dyes.

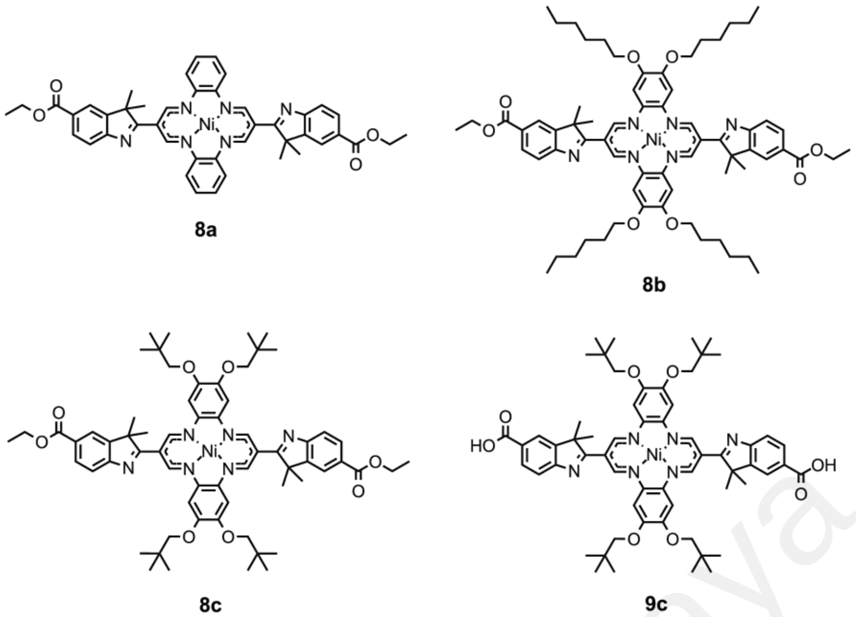

8a

8b

8c

9c

Figure 1.3: Molecular structures of the dyes used in this study.

1.1 Aims and objectives of this study

Generally, the aims of this research include synthesis, characterization, and determination of the efficiency of the dyes based on macrocyclic DBTAA nickel complexes as new sensitizers for DSSC.

Specifically, the objectives of the research are:

1. To synthesize and characterize a new class of sensitizers based on the indolenine – DBTAA nickel complexes for DSSCs application.
2. To study the properties of new sensitizers based on NMR, UV, electrochemistry, and computational (DFT) analyses.
3. To determine the efficiency of the DBTAA sensitizers on DSSCs application.
4. To compare the effectiveness of electron injection between COOH and ethyl ester anchoring groups based on the Incident - Photon to Current Efficiency (IPCE), Electrochemical Impedance Spectroscopy (EIS), and electron lifetime measurements.

CHAPTER 2: LITERATURE REVIEW

2.1 General

Undeniably, a dramatic growth of world human population has become a major contributor to global warming, owing to the increased production of greenhouse gases as humans increasingly use non-renewable resources, such as fossil fuels, petroleum oil, coal, and natural gas for energy production (Wu *et al.*, 2015). Many efforts have been taken in seeking alternatives for energy production from renewable resources, such as solar energy (Schiermeier *et al.*, 2008). For example, the third generation of photovoltaic cells, Dye Sensitized Solar Cells (DSSCs) as shown in **Figure 2.1** was found to be one of the most promising solar cell for clean energy production with high efficiency in converting electrical energy from sunlight (Dresselhaus & Thomas, 2001).

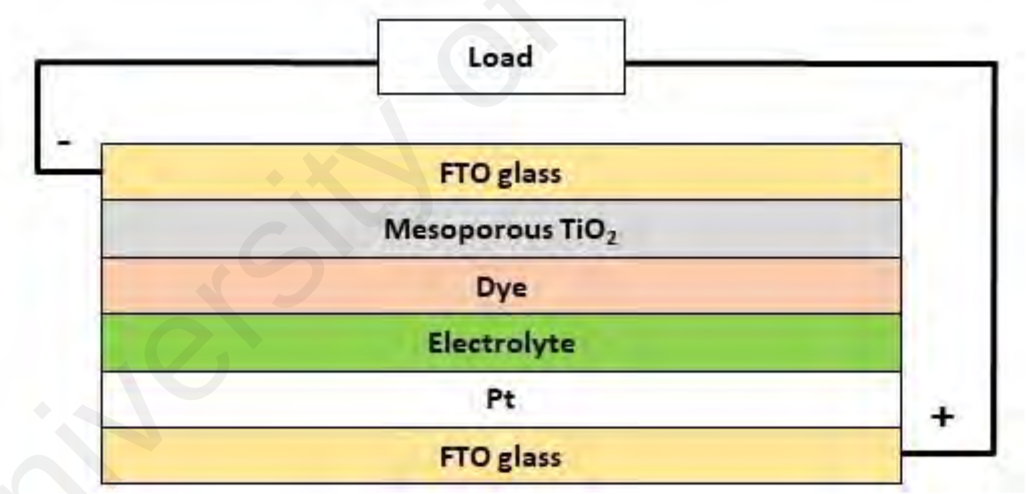

Figure 2.1: The schematic layers of DSSC components.

Among of the DSSC's components, a structural design of dye molecules has gained significant attention for modifying the cell structure. The dye based on ruthenium complex is one of the widely explored in the beginning as it is found as the most effective sensitizers, which exhibits high conversion electrical energy, long-term stability and easy to be synthesized (Keita *et al.*, 2010). In 2012, Ozawa's developed the 'black dye' (N749) as depicted in **Figure 2.2** and achieved an overall efficiency of 11.6% under full illumination of the cell (Ozawa *et al.*, 2012).

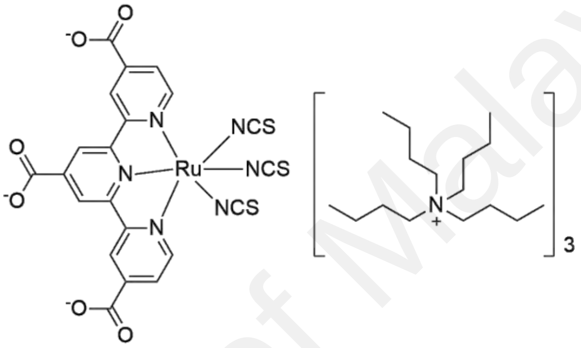

Figure 2.2: Molecular structure of 'Black Dye' (Ozawa *et al.*, 2012).

However, the production of ruthenium metal is expensive and not economic to be used for the conventional solar cell. An alternative way, based on a research from the Gratzel's group in 1993, had found the highly potential dye based on Zn-porphyrin as a new sensitizer for the replacement of the ruthenium dye. The great discovery of this structure was inspired by the chlorophyll molecules as shown in **Figure 2.3**, which was derived from the Mg-porphyrin that demonstrated an incredible photon energy captures form the sunlight for photosynthesis process (Kay & Graetzel, 1993). Therefore, the porphyrin derivatives have gained significant attention today for the structural design of new sensitizer in order to improve the cell efficiency. Regrettably, the porphyrin are still not suitable to be applied in a conventional solar cell, due to the expensive raw materials, average efficiency obtained again ruthenium dyes, and low production yield. Eventually it leads to another class of macrocyclic, dibenzotetra[14]annulene (DBTAA) which was found to be suitable and a potential candidate to replace the porphyrin dye as synthetic sensitizers for DSSCs application.

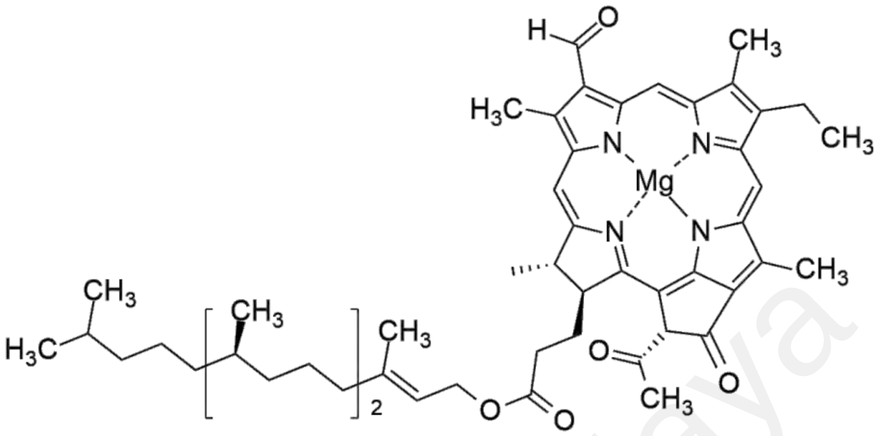

Figure 2.3: Molecular structure of chlorophyll (Kay & Graetzel, 1993).

2.2 Background of dibenzotetraaza[14]annulene

Dibenzotetraaza[14]annulenes (DBTAAs) is a well-known compound and first introduced in 1969 (Chave & Honeybourne, 1969) but is less studied. The DBTAA compound is close structural resemblance to porphyrins as depicted in **Figure 2.4**. Similar to porphyrins, they have a π-conjugated framework with four nitrogen atoms in the core ring which can be deprotonated to form a dianionic ligand for metal ions. The π-electrons in the DBTAA structure are delocalized over the entire 1,3-propanediiminato linkages only, unlike the porphyrin ring the π-electrons are found delocalized over the whole entire ring system (Mountford, 1998). In addition, the DBTAA is Huckel anti-aromatic (4n) π compound (Huang *et al.*, 2012), containing 12 π-electrons over the entire ring, whereas the aromatic (4n + 2) π porphyrin consists of 18 π–electrons.

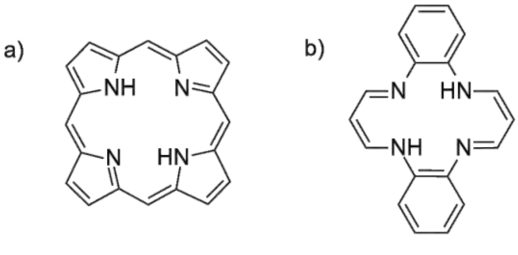

Figure 2.4: Chemical structure of **a)** porphyrin and **b)** DBTAA.

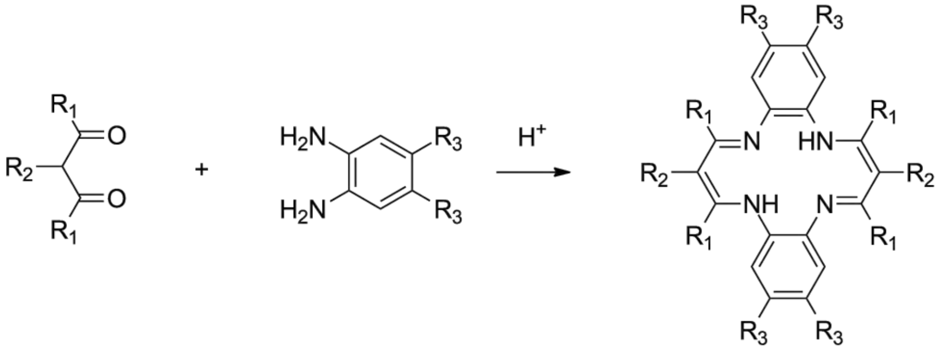

Figure 2.5: Synthesis of DBTAA (Reichardt & Scheibelein, 1978).

DBTAAs ligands are usually prepared using a non-template method through a condensation reaction between 1,3-dicarbonyl and various types of *o*-phenylene diamine in [2:2] equimolar ratio (Reichardt & Scheibelein, 1978) in the presence of acid as catalyst. The general synthesis of DBTAA is shown in **Figure 2.5.** The formation of the ligands is confirmed based on the presence of NH protons signal resonances at downfield region typically around 14 - 15 ppm in the ^{1}H NMR spectrum, depending on the ring substituents. The appereance of NH at deshielded region in the ^{1}H NMR spectrum are caused by the strong anti-aromatic ring current effect of π-electrons, and the induced magnetic field is same direction to the applied magnetic field as shown in **Figure 2.6** (Zwolinski *et al.*, 2018). Additionally, the structure has two conjugated indolic fragments of NH protons on the inner ring which exhibited imine – enamine tautomeric forms between 1,3-propanediminato linkages (Azuma *et al.*, 1995).

In contrast, the NH protons of porphyrin ligands are more shielded, as the result the signal appears as a broad peak in the range of -1 to -3 ppm in the ^{1}H NMR spectrum (Pareek *et al.*, 2014).

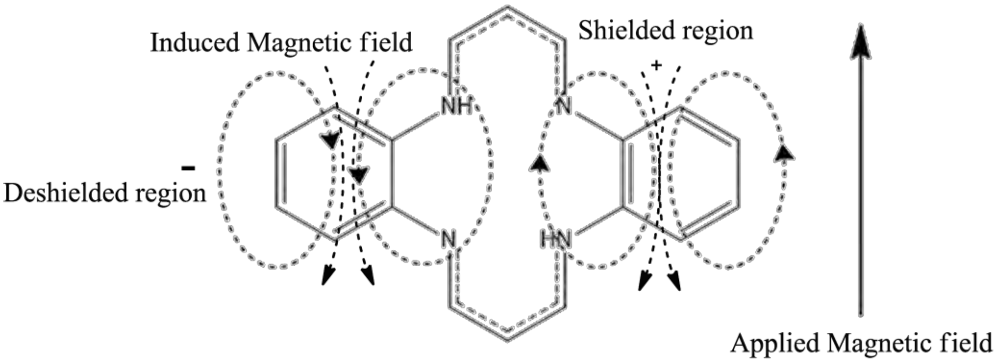

Figure 2.6: The magnetic anisotropic effect of NH on the DBTAA ring.

In the ^{1}H NMR spectrum, the NH proton peak of inner core is usually observed as a triplet with $^{3}J_{\mathrm{NH}} = 6.0$ Hz when (R_1 = H) (Dudek *et al.*, 2011; Zwolinski & Eilmes, 2016), due to the bridging and the *trans* – coupling interactions as shown in **Figure 2.7**. The produced signals of each interaction are collapsed equally with [1:1] integral ratio, thus producing a triplet peak of NH (Honeybourne, 1974). Interestingly, the appearance of $^{3}J_{\mathrm{trans}}$ of NH is found half of the normal $^{3}J_{\mathrm{trans}}$ value (≈12 Hz) which is caused by the elongation of NH bond. Consequently, the electron charge density at the *s*-atomic orbital on the N and H atoms are reduced by 50% due to imine – enamine tautomerism characters (Honeybourne, 1974). However, the NH proton will appear as a broad small singlet signals when (R_1 ≠ H) (Sakata & Itoh, 1992).

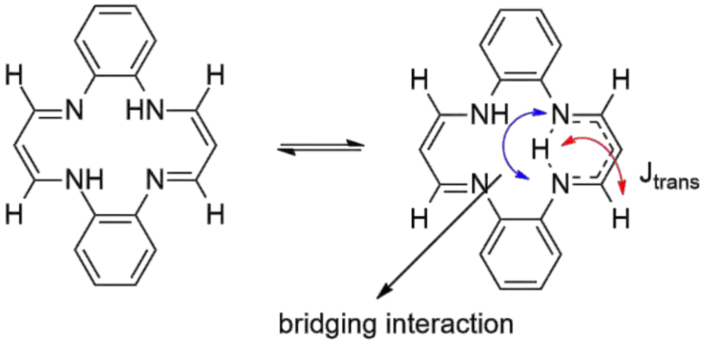

Figure 2.7: The imine - enamine tautomeric of DBTAA with the NH bridging and *trans* - coupling interactions.

Furthermore, the DBTAA ligands are more flexible compared to the porphyrin. They are able to adopt different structural conformations depending on the ring substituent at R_1 position. The ligands tend to form a planar shape conformation when (R_1 = H) (Sister *et al.*, 1988). Moreover, the structure is adopt a slight saddle-shaped conformation when *β*-subsituted ($R_1 \neq$ H) due to steric interactions between the R_1 substituents and H-atoms of the *o*-phenylene rings (Cotton & Czuchajowska, 1990). The solid state structure of these two mentioned conformations is shown in **Figure 2.8**.

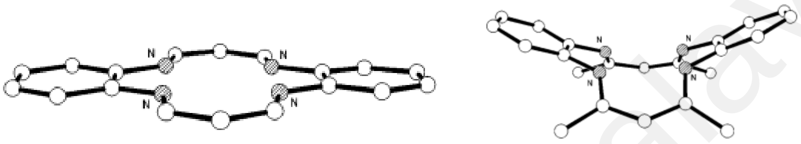

Figure 2.8: The planar (left) and saddle-shaped (right) solid state structures of DBTAA (Mountford, 1998).

Additionally, the insertion of a transition metal ion such as (Ni^{2+}, Cu^{2+}, Co^{2+}) into the core ligand tends to form a square - planar complex as shown in **Figure 2.9** with linear stacking patterns in the solid state arrangement. However, it is challenging to work with Cu-DBTAA and Co-DBTAA complexes because most of the complexes are paramagnetic (Whyte *et al.*, 2012), or in other words they are NMR inactive. Therefore, the complex structures are usually confirmed based on the crystallography, UV, IR or CHN analyses. While, the Ni-DBTAA complexes are diamagetic, thus NMR measurement can be used to elucidate its structure (Bonadies *et al.*, 1989).

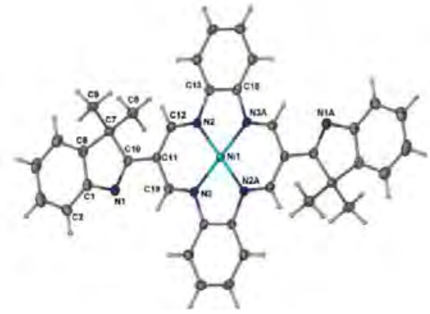

Figure 2.9: The crystal structure of Ni-DBTAA (Khaledi *et al.*, 2013).

Among the transition metal ions, Zn^{2+} was found coordinating to the DBTAA core by forming a square – pyramidal complex as shown in **Figure 2.10** (Mulyana *et al.*, 2011). From the structure, the pyridyl group located on the adjacent sites of the Zn-DBTAA complex is axially coordinated to the centrosymmetric centre on the $[N_4]$ plane to another Zn-DBTAA complex through the Zn metal.

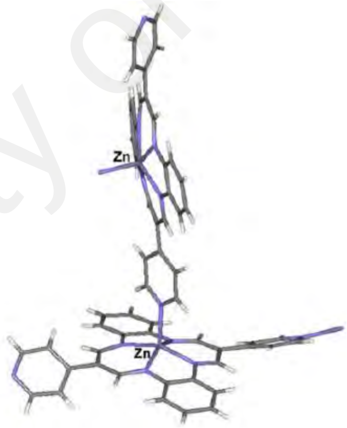

Figure 2.10: The crystal structure of Zn-DBTAA (Mulyana *et al.*, 2011).

The non-planarity of the DBTAA metal complex was caused by the larger – sized metal ion used, owing to the limited space at the metal coordination site in the ligand and the effect of electron count in the *d*-orbitals (Mountford, 1998). The remarkable flexibility the ligands offer a few unusual coordination modes of certain metal complexes. As shown in **Figure 2.12,** the gallium (Ga) metal ion coordinated to the ligand with a NH group of inner core remained in the complex structure (Cannadine *et al.*, 1995).

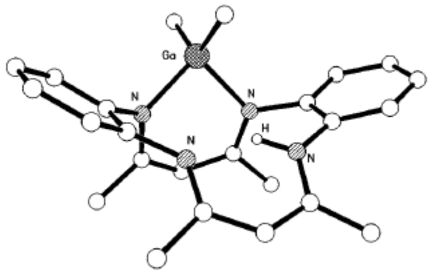

Figure 2.11: The crystal structure of Ga-DBTAA (Cannadine *et al.*, 1995).

Furthermore, the characteristics of DBTAA ligand or complex having a high molecular weight with planar geometrical structure, often leads to solubility issues that will limit their studies in various potential applications. However, the solubility of DBTAA compound in low boiling point of organic solvents can be improved by introducing suitable alkyl chains or bulky organic groups to disrupt its π-π stacking aggregation (Cutler *et al.*, 1985).

The special features of DBTAA having a strong light absorption in the range of 400 nm and 600 nm with high molar extinction coefficient in the solution (Sakata *et al.*, 1996) shows that the DBTAA has similar properties as porphyrin molecules. Although there are numerous reports of DBTAA derivatives in various studies such as liquid crystallinity (Grolik *et al.*, 2012), catalysis mimics (Sustmann *et al.*, 2007), electrochemistry (Keita *et al.*, 1994), field effect transisitors (Whyte *et al.*, 2012), and biological activity (Reddy *et al.*, 2012; Stojkovic *et al.*, 2010), the potential of DBTAA molecules as sensitizers in DSSCs remains unexplored.

2.3 DSSC working principle

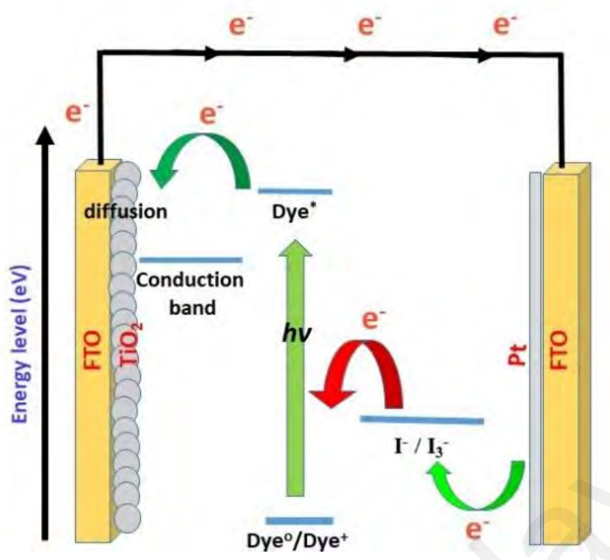

Figure 2.12: Schematic diagram illustrating the working principle of a dye sensitized solar cell.

A schematic operating principle of a DSSC is shown in **Figure 2.12**. The FTO/TiO_2 photoanode is sensitized by dye molecules as electrons source in the cell. Firstly, the dye undergo photoexcitation, whereby the dye is excited from HOMO to LUMO energy states upon receiving the photon energy (Le Bahers *et al.*, 2013). At the excited state, the electron is then injected and transferred into the nanocrystalline TiO_2 through diffusion process, and the work done by the electron is delivered externally in the form of electrical energy. The oxidized dye will undergo a dye generation process to restore its stable original state by receiving an electron from the iodine electrolyte through redox reaction (Grätzel, 2003). The triiodide ions (I_3^-) formed by the oxidation of (I^-) is then regenerated by accepting electrons at the surface platized cathode (a FTO glass coated with platinum catalyst) (Wu *et al.*, 2015). Finally, the electrical circuit is complete *via* electron migration through the external load to generate V_{oc} and J_{sc} in the cell. All the photochemical processes occur in a DSSCs can be expressed as the following equations (Ladomenou *et al.*, 2014).

$TiO_2 \mid Dye^{o}$ (HOMO) + photon energy ($h\nu$) → $TiO_2 \mid Dye^{*}$ (LUMO) (Photoexcitation)

$TiO_2 \mid Dye^{*} \rightarrow e^{-} + TiO_2 \mid Dye^{+}$ (Electron injection)

$TiO_2 \mid Dye^{+} + 3I^{-} \rightarrow TiO_2 \mid Dye + I_3^{-}$ (Regeneration of dye)

$I_3^{-} + 2e^{-}$ (Pt) → $3I^{-}$ (Regeneration of electrolyte)

2.4 Sensitizers

2.4.1 The roles of anchoring group

One of the essential parts in the sensitizers of DSSCs is type of anchoring groups incorporated into the dye framework such as -COOH, pyridine, pyridine-N-oxide, -OH, -PO_3H, -SO_3H, cyanoacrylic acid, ester, salicylic acid, catechol, and $B(OH)_3$. The presence of the anchoring group not only enables the dye to be absorb onto a TiO_2 but also provides a strong linkage for electron transfer from the donors to the acceptors moiety. Among all the anchoring group which have been tested for DSSCs, COOH and cyanoacrylic acid are always found exhibiting excellent electron withdrawing ability, enabling a good surface contact between TiO_2 and the dye, and providing superior stability for DSSCs (Campbell *et al.*, 2004). A COOH containing dye is adsorped onto the TiO_2 through six possible binding linkages as shown in **Figure 2.13**, which are monodentate ester, bidentate chelating, bidentate bridging, monodentate and bidentate H-bonding, and monodentate coordinating of C=O (Zhang & Cole, 2015). These remarkable number of possible binding linkages has provided a strong binding ability of the COOH group to the TiO_2, compared to the other anchoring groups, such as pyridyl anchoring group, leading to a more dye loaded on the working electrode photoanode and believed to bring a great improvement of DSSCs efficiency.

A study by Harima's and his co-workers revealed that the COOH containing dyes had improved the absorption amount of dyes onto the TiO_2 surface compared to pyridine anchoring group, owing to the different in their adsorption behaviours onto the TiO_2 (Harima *et al.*, 2013). The COOH anchoring group was found preferably to be adsorped at the Bronsted acidic sites, whereas the pyridyl preferably at the Lewis acidic sites of the TiO_2 surface. Furthermore, a recent study by Lun Mai's in 2015 has shown that the employment of several types of anchoring groups in the dye, greatly improves the DSSCs efficiency. In the study, they found that the dye containing an additional of COOH or OH group on the pyridyl anchoring groups exhibited improvement of electrons transport due to strong binding communication of the dye on TiO_2 surface compared to single pyridyl anchoring group only (Mai *et al.*, 2015). Besides that, the use of strong anchoring groups in the dye framework will lead to a bathchromic shift in the optical spectra after sensitizing the dye onto the photoanode TiO_2 and this helps in exciting the electrons to the conduction band of TiO_2 more effectively (Xue *et al.*, 2014).

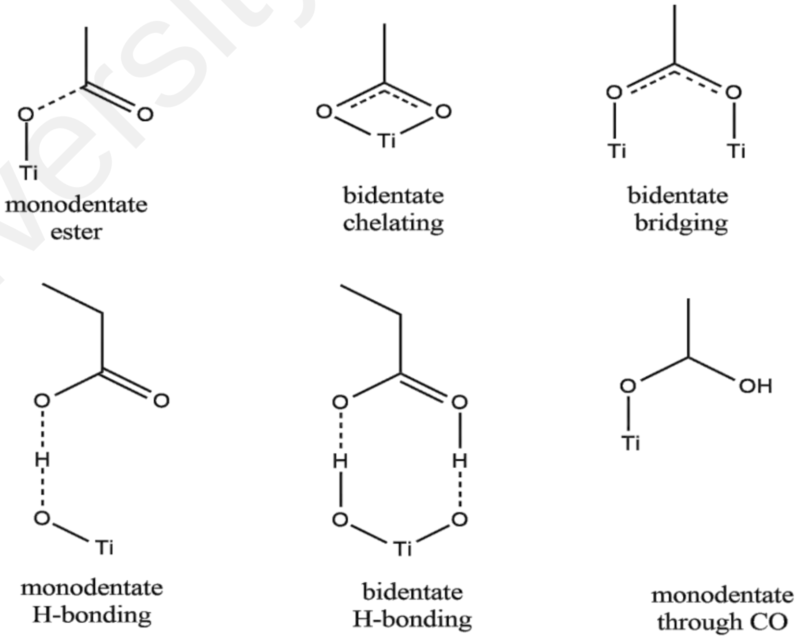

Figure 2.13: The possible binding modes of COOH anchored on TiO_2 surface (Zhang & Cole, 2015).

2.4.2 Position of anchoring group

The substitution position of the anchoring group is very important to design the dye molecule in order to achieve high efficiency of DSSC. In the case of porphyrin dye, the COOH anchoring group at *ortho*, *meta*, and *para* positions of the phenyl rings significantly affect the DSSC performance by changing the geometric shape of the dye's attachment onto the TiO_2 surface as depicted in **Figure 2.14**. A research outcome from the D'Sauza and his co-workers revealed that the dye with COOH substituted at *meta*-position exhibited more effective Intramolecular Charge Transfer (ICT) and rate of electron injection than other substitution positions (Hart *et al.*, 2013). The effect of the anchoring positions on the DSSC efficiency is due to the higher energy level of the LUMO *meta*-substituted of porphyrin dye than the CB of TiO_2, therefore the probability for charge recombination to take place is lower than charge injection.

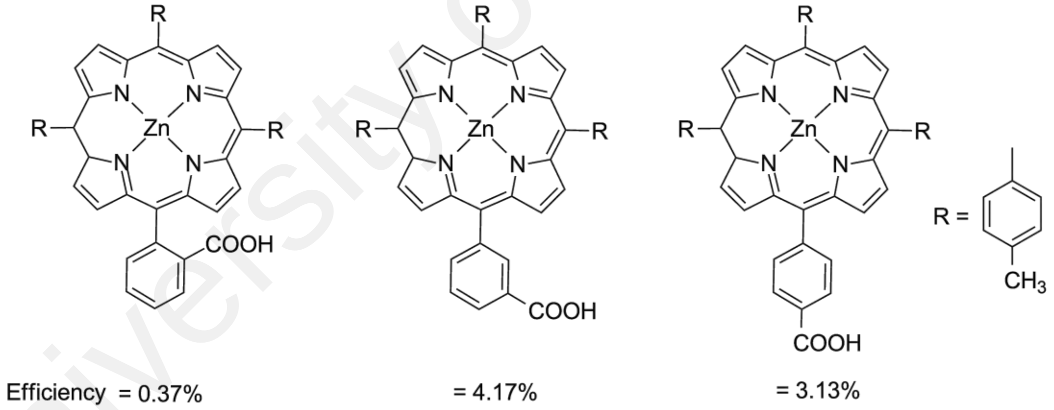

Figure 2.14: Porphyrin dyes with COOH group anchoring at *ortho* (left), *meta* (middle) and *para* (right) positions, respectively.

Additionally, the different substitution position on the dye will lead to various binding orientation modes between the dyes and the TiO_2 surface. The *meta*-substituted dye usually adopts a titled orientation modes as depicted in **Figure 2.15**, thus give an advantages in term of electron injection and dye loaded onto the TiO_2 surface compared to other positions (Ambre *et al.*, 2015).

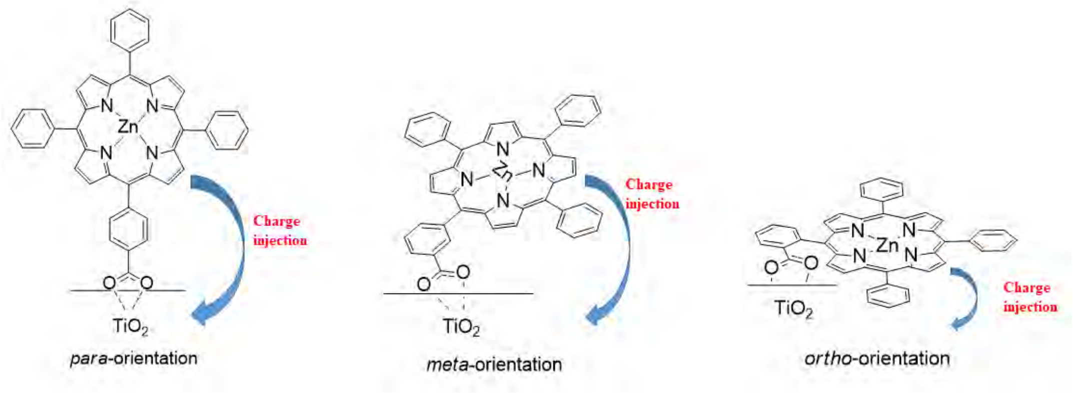

Figure 2.15: Possible orientation of dye to TiO_2 (Hart *et al.*, 2013).

2.4.3 Number of anchoring group

The number of anchoring group in the dye framework is also a factor determining the DSSC performance. As shown in **Figure 2.16**, an investigation done by Ambre's research team revealed that the DSSCs performance was greatly improved in terms of its several parameters like J_{sc}, V_{oc} and *FF* by increasing the number of COOH anchoring group in the dye. This was due to the increased number of interaction sites of the dye molecule with TiO_2, thus increasing the amount and rate of electron injection. However, the limited availability of the TiO_2 surface area, porphyrin-based ligand with di-anchoring groups was found to have higher dye loaded amount onto the TiO_2, in comparison to the mono- and tri- anchoring groups (Ambre *et al.*, 2015).

Contradictorily, a research outcome from Shang's group showed that the increased number of anchoring group did not always improve the DSSC efficiency, as they found that triphenylamine derivative-based dye with mono-anchoring group of rhodamine-3-acetic acid exhibited higher efficiency compared to di- and tri- anchoring group (Shang *et al.*, 2010). In conclusion, as increasing number of anchoring groups is not promising to increase the cell efficiency.

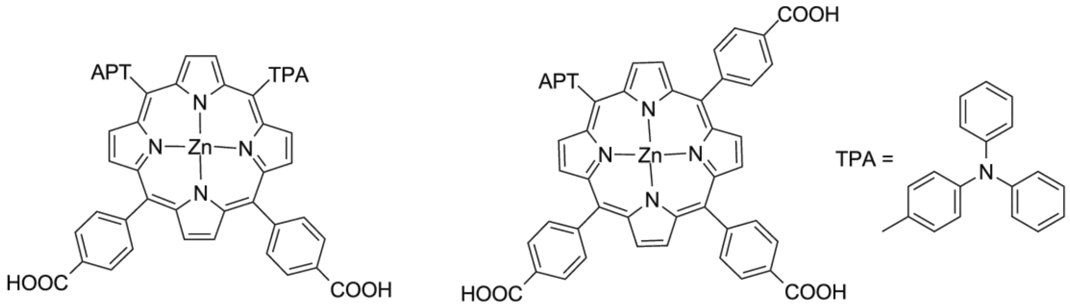

Efficiency = 4.02%

Efficiency = 5.36%

Figure 2.16: The di- (left) and tri- (right) anchoring group of Zn-porphyrin.

2.5 The effect of substitute π – conjugated linkers

Although the current porphyrin dyes are well-known of their ability in achieving a promisingly high efficiency in the DSSCs, yet many efforts have been taken to improve the cell performance through structural modifications on the dyes. The common substituted π–conjugated linkers like phenyl (Kitamura *et al.*, 2004), anthracene (Teng *et al.*, 2010), thiophene (Liu *et al.*, 2009), thienyl (Chen *et al.*, 2007), oligothiophene (Liu *et al.*, 2010), carbozale (Jungsuttiwong *et al.*, 2012), etc., will broaden and extend the absorption spectra of the dyes until IR region. The extension of π-conjugated system of the dye molecule is not only to increase the amount of electron injection to the CB TiO_2 but also reduce the energy gap between the HOMO and the LUMO energy levels (Song *et al.*, 2018). Additionally, π–conjugated linkers help in reducing the recombination of electron between the dye and electrolyte in the cell (Li *et al.*, 2010).

For instance, a study by Jungsuttiwong's research team in 2016 on investigating the effects of thiophene derivatives as a π-linkers as depicted in **Figure 2.17**, achieved a good efficiency in between of 1.14% to 3.51% (Jungsuttiwong *et al.*, 2017) as increasing the π-conjugation in the dye structures. The dye containing more π-conjugated system will lead to higher light-harvesting efficiency (LHE) properties as improving the J_{sc} and *FF* parameters of DSSCs (Feng *et al.*, 2017).

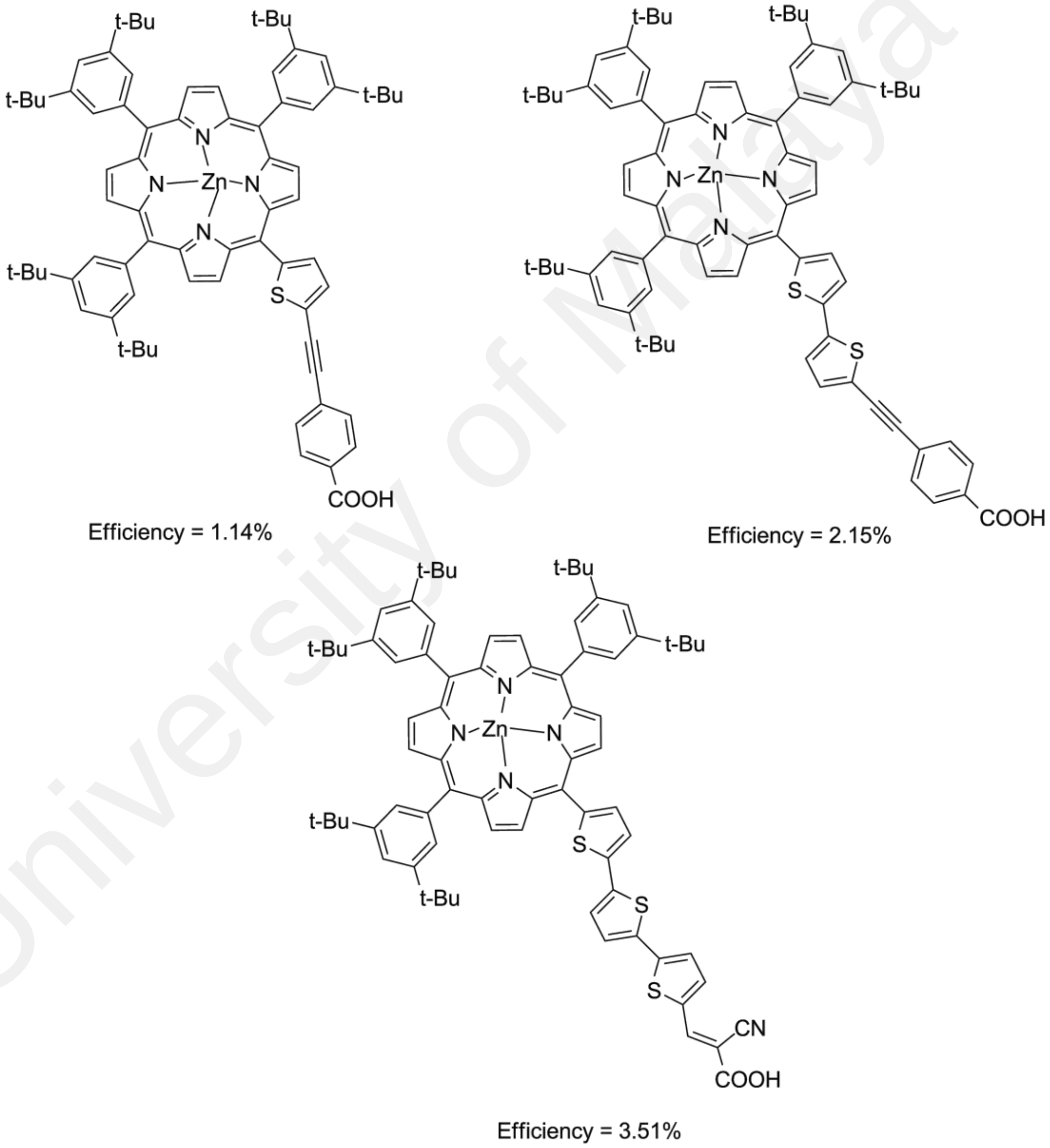

Figure 2.17: Molecular structures of porphyrin dyes containing different substituent of π - conjugated linker.

2.6 The importance of alkyl chains substitution

Alkyl chains substituent plays a crucial role in enhancing the solubility of the dye molecule in the organic solvents for easy characterization. The substitution is used to prevent the dye from π–π stacking aggregation on the photoanode surface, which can impair the DSSCs performance. The introduction of longer alkyl chain into the dye helps to increase the electron lifetime of the dye by acting as an effective blocking spacer between the TiO_2 layer and electrolyte. Thus, it suppresses the recombination of electron in the TiO_2 film and decreases the rate constant for electron captured by the electrolyte. The substitution is not only lengthening the electron lifetime but also improving the J_{sc} and V_{oc} parameters of the cell (Yu *et al.*, 2011). Besides, the alkyl chain substituents were also found able to tune the gap between the HOMO and the LUMO energy levels. As illustrated in **Figure 2.18**, the example of organic dyes furnishing with linear or branched alkyl chains significantly improved the dye's performance as compared to the unsubstituted alkyl chain (Feng *et al.*, 2013).

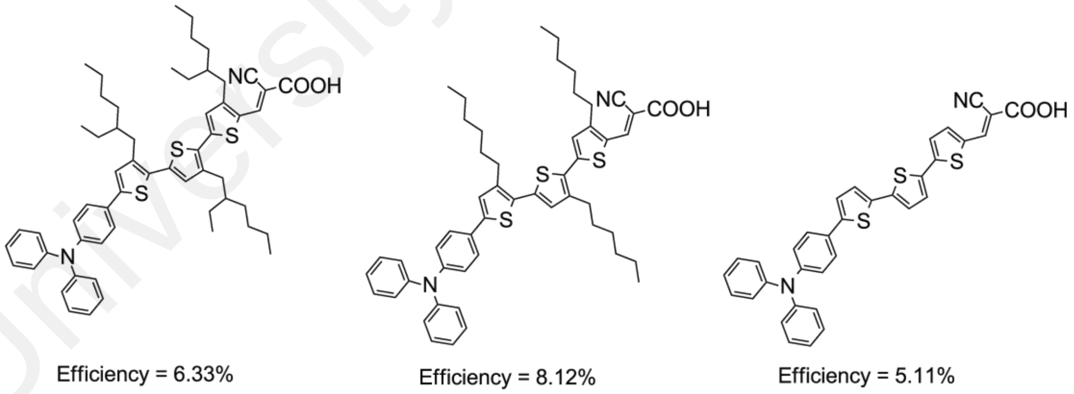

Figure 2.18: The chemical structures of thiophene-based dyes with various alkyl chain substituents (Feng *et al.*, 2013).

2.7 Electrolyte

The choice of electrolyte used is one of the important factors that influenced the performance of the DSSCs. The electrolytes are responsible as charge transport carriers, which supply electrons to form the ground state dyes from their oxidized state form during the DSSCs operations. The use of iodide/triiodide (I^-/I_3^-) - based liquid electrolyte in the DSSCs has been widely employed, owing to its notably advantages such as easy preparation, high conductivity, low viscosity, high redox stability, good mobility and it also provide a good interface contact with the counter electrode (Wu *et al.*, 2015). Typically, a liquid electrolyte consists of several components such as solvent, ionic liquid, and additives to achieve the optimum performance of dye in the cell (Kusama & Arakawa, 2004).

Acetonitrile is considered as the best solvent for liquid electrolyte because of its impressive iodine-solubilizing ability, low viscosity and excellent chemical stability (Grätzel, 2009). However, acetonitrile is not suitable for long-term use in DSSCs, as it is quite volatile solvent, leakage and evaporation may happen over time. Therefore, the polymer-typed electrolyte is then introduced as a replacement for the former solvent (Hagfeldt *et al.*, 2010). Among of them, imidazolium derivatives such as methyl-hexyl-imidazolium iodide, is one of the most frequently used as ionic liquid in an electrolyte mixture to improve the stability of dyes in DSSCs (Bai *et al.*, 2008). However, it slightly reduced the cell efficiency due to the high viscosity attributing low ionic mobility that is caused by the low diffusion coefficient and mass-transport limitations factors (Gorlov & Kloo, 2008). Furthermore, compound 4-tert-butylpyridine is typically added as an additive into the electrolyte mixture to reduce the chance of electron recombination between the TiO_2 and electrolyte, which reduce the overall DSSCs performance. In 1993, a study by Gratzel's group revealed that the effect addition of 4-tert-butylpyridine dramatically increased the V_{oc} parameter of DSSCs (Bella *et al.*, 2014).

2.8 Counter electrode

Platinum (Pt) is one of the least reactive elements that widely employed in electrochemistry applications. In DSSCs, the FTO glass coated with Pt element is extensively used as counter electrode for completing the electron circulation in the cell (Klfout *et al.*, 2017). The platinum electrode is also acts as a positive terminal which collects electrons from the external circuit that come from the negative terminal of working electrode (dye/TiO_2/FTO) (Thomas *et al.*, 2014). Moreover, the Pt counter electrode can also acts as a mirror to reflect the unabsorbed light illuminated on the cell, thus improving the light-harvesting properties (Wu *et al.*, 2017). The platinum electrode exhibits low charge transfer resistance that can help to achieve a good catalytic activity for triiodide reduction in the cell (Wu *et al.*, 2015). Moreover, the minimum thickness of Pt element coated on the FTO glass is must be greater than 2.0 nm in order to achieve optimum performance of the cell (Fang *et al.*, 2004).

Despite of its good conductivity and resistance to corrosion, the Pt electrode possesses several weaknesses that impair the DSSC performance. The electrode was found able to undergo oxidation and dissolution processes forming the PtI_4 or H_2PtI_6 as the side-products when interacting with I^-/I_3^- electrolyte for prolonged period of time in the cell (Gang *et al.*, 2013). The electrode is also ineffective to be used as a counter electrode if the cobalt-complexes or polysulfide electrolyte used in the cell due to their energy level is similar to energy level of Pt counter electrode. Consequently, the redox electrolyte was difficult to receive or accept electron at the Pt electrode surface for generation process (Wu *et al.*, 2012). Finally, the use of platinum electrode is still not economic, since its extraction is a very expensive process.

2.9 Nanostructured of TiO_2

TiO_2 is widely employed as semiconductor metal oxide, due to its abundantly available, cheap, non-toxic, resist to corrosion and having good chemical and physical stabilities. The nanostructured TiO_2 deposited onto the transparent FTO glass can be obtained through an annealing process. The morphology of TiO_2 film obtained depends on the annealing temperature as shown in **Figure 2.19**. The TiO_2 film sintered at the optimum temperature, 400 ^{o}C provides the fastest transport and slowest recombination kinetics of electrons on the film (Zhu *et al.*, 2010). Increasing the annealing temperature will create a rutile and more defects sites on the nanocrystalline TiO_2 which will affect the amount of electron to be injected for external work done as electrical energy. For instance, the electron transport using the photoanode annealing at 600 ^{o}C gave more recombination effect to the dyes and decreased the amount of available electron used for generating electrical energy in DSSCs (Taib *et al.*, 2016). Moreover, the TiO_2 has always been maintained at thickness below 20 μm in order to achieve the optimum dyes efficiency for greater diffusion rate of electron injection (Jasim, 2011) and to reduce the electron losses in the cell (Choi *et al.*, 2012). The annealing process has provided sufficiently large surface area for dye to be absorbed on the TiO_2 film, thus helps improving the LHE profile and efficiency of the cell.

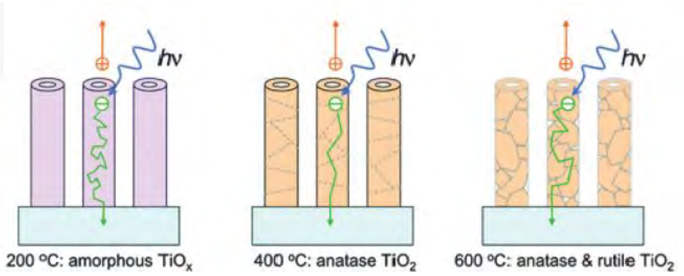

Figure 2.19: The effect of annealing temperature on the light-harvesting efficiency of TiO_2.

2.10 Relationships between *J*sc, *V*oc and *FF* parameters

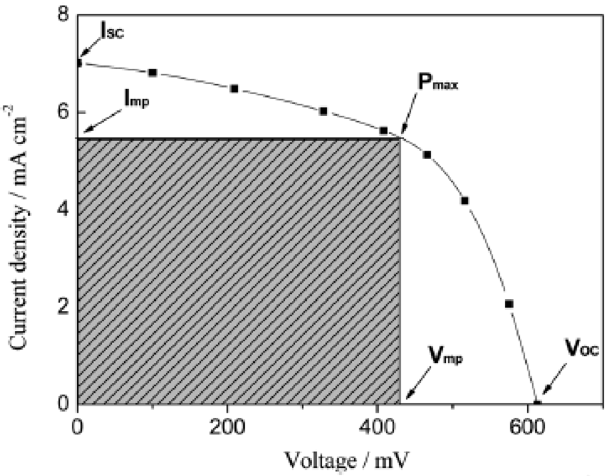

Figure 2.20: Example of *J-V* curve measurement.

The performance of the complete fabricated DSSCs can be evaluated based on the relationship between the current density, J_{sc} and voltage (V) under stimulated standard conditions. As shown in **Figure 2.20**, the maximum value of J_{sc} can be obtained when $V = 0$ mV, and the interception at $J_{sc} = 0$ mA cm^{-2} indicated the highest V_{oc} value achieved by the cell. The J_{sc} value is strongly related to the energy difference between HOMO and LUMO of the dyes, total of electron transfers to the CB of TiO_2, and the potential (V_{oc}) difference between the TiO_2/dye/electrolyte interfaces (Zhang & Cole, 2015). The magnitude of the J_{sc} obtained in the *J-V* measurement can be further explained by the IPCE analysis which the spectrum provides information about the percentage of photon convert to electrical energy at different light wavelength. The formula of IPCE is defined as:

Equation **(1)**

$$IPCE\ (\lambda) = \frac{1240\ \ (eV.nm)\times J_{sc}\ (\mu A\ /cm^{2})}{\lambda(nm)\times I\ (\mu W/cm^{-2})}$$

where λ is the wavelength of the absorbed photon, *I* is the light intensity at specific wavelength, and 1240 *e*V = Plank constant × speed of light (3.0×10^{8} ms^{-1}).

The V_{oc} value as shown in the J-V curve is related to the differences of energy levels between redox electrolyte and quasi-Fermi of the semiconductor (Qi & Wang, 2012).

The equation is described as below:

Equation **(2)**

$$Voc = \frac{E_{CB}}{q} + \frac{kT}{q}\ln\left[\frac{n}{N_{cb}}\right] - \frac{E_{redox}}{q}$$

where n is the number of the electrons in TiO_2, N_{cb} is the effective density of states in TiO_2, E_{CB} is the energy level of the lower end of the CB in TiO_2, E_{redox} is the potential level of the redox couple, and q is the unit charge. From the equation (**2**), the V_{oc} value is increased if the electron recombination from the conduction band of TiO_2 to the electrolyte, and electron recombination from the conduction band of TiO_2 to the oxidized sensitizer are reduced. The E_{redox} should be lowered in order to achieve a greater V_{oc} value (Ning *et al.*, 2010).

The fill factor, FF is the series resistance related to the charge recombination reaction in the cell. The value is defined as the ratio between P_{max}, which is obtained from the J-V curve, to the product of V_{oc} and J_{sc} values. The calculated FF parameter is in the range 0 to 1, and it's unitless.

Therefore, the overall cell efficiency, η is calculated according to equation (**3**).

Equation **(3)**

$$\eta = \frac{J_{sc}\ (mA\ cm^{-2})\ \times\ V_{oc}\ (V)\ \times\ FF}{P_{in}\ (mW\ cm^{-2})} \times 100\ \%$$

Additionally, the V_{oc} value from the *J-V* curve can be further explained by Electrochemical Impedance Spectroscopy (EIS) Nyquist plot. The spectrum is one of the powerful tools to provide information and evaluate the mobility of charge carriers (holes and electrons) at different applied voltages during DSSCs operation (Chulkin *et al.*, 2018; Sarker *et al.*, 2014). Generally, the spectrum is derived from the curve fitting calculation using a Z-view software which involved the complicated mathematical expression (Liao *et al.*, 2017; Mingsukang *et al.*, 2017). The R_s, CPE1 and CPE2 are the series resistance, and parameters of constant phase on each interfacial phase, respectively. All these three parameters are essential in order to obtain the curve fitting results. Basically, the spectrum will appears as two semicircles which are corresponding to the interfacial resistance in DSSCs components of R_1 and R_2 as shown in **Figure 2.21**.

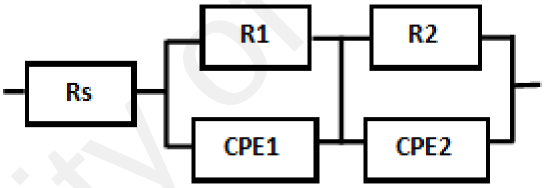

Figure 2.21: Circuit description code (CDC).

The first semicircle on the left, R_1 occur at the high frequency level in the spectrum, associated to the interfacial resistance between the Pt counter electrode and the electrolyte. The middle semicircle in the spectrum is represented by R_2, indicated the interfacial resistance between dye/TiO_2/electrolyte interspaces (Zervaki *et al.*, 2014). The larger resistance of both R_1 and R_2 values indicated the small charge recombination rate, thus improving the V_{oc} and FF parameters of the devices (Xue *et al.*, 2014; Yum *et al.*, 2012).

2.11 The causes of low efficiency of DSSC

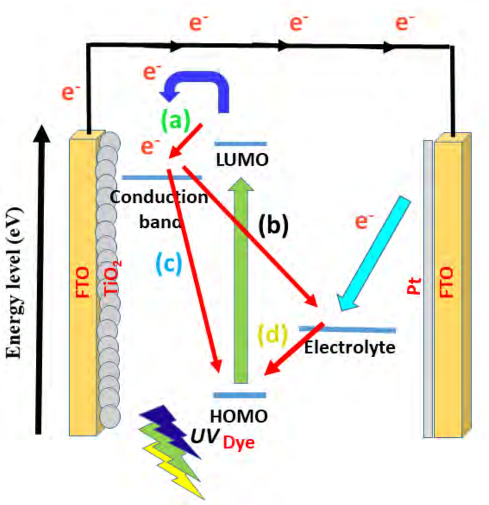

Figure 2.22: Schematic DSSC components for the explanation of electron transportation loss during operation.

There are four possibilities of low efficiency of DSSC as shown in **Figure 2.22** (Listorti *et al.*, 2011). Process **(a)** is explains the low charge injection of electron from the LUMO energy level to the CB TiO_2. The low charge injection is caused by weak binding attachment of dye onto the TiO_2 which may reduce the amount of excited electron at LUMO energy levels upon exposed to UV light (Zhang & Cole, 2015). The low charge injection is also due to the LUMO energy levels is more negative than the energy level of CB TiO_2 (-4.00 *e*V). To overcome the problem, the LUMO energy level must be more positive than the CB TiO_2 to ensure that the electron has sufficiently driving force for electron transfer from the LUMO energy level to the CB TiO_2 (Yu *et al.*, 2014).

Furthermore, a research outcome from Thalluri's group was investigated that the low efficiency of DSSC is due to weak regeneration of redox mediator electrolyte in the cell as shown in process **(b)**. The electron at the CB TiO_2 is used for regeneration process of electrolyte which is caused by the slower electron transfer from the Pt counter electrode to the triiodide ($3\ I^-$) electrolyte (Thalluri *et al.*, 2013).

Furthermore, the regeneration process of the dye occurs by accepting an electron from the redox mediator of electrolyte. The short regeneration time of dye cation has a high chance that the electron at CB TiO_2 is used to restore the original state of the oxidized dye. Consequently, less electron is being delivered through the cell for photoelectrochemical process. This situation is called as recombination of electrons between the TiO_2 and the dye cation (Omata *et al.*, 2015) as illustrated in process **(c).**

Finally, process **(d)** is the weak regeneration of dye cation from redox electrolyte (Zhang *et al.*, 2010). This phenomenon happens when electron from the electrolyte has insufficient thermodynamically energy of electron transfer for regeneration dye cation to its original state, due to the HOMO energy level of dye located more positive than the energy level of redox electrolyte (-4.90 *e*V) (Funaki *et al.*, 2014).

CHAPTER 3: EXPERIMENTAL

3.1 Materials

All materials and solvents were purchased from suppliers without further purification. Isopropyl methyl ketone, potassium iodide (KI), potassium carbonate (K_2CO_3), catechol, phosphoryl chloride ($POCl_3$), 65% HNO_3, pyridine, 2-propanol, hexane, acetonitrile (MeCN), deuterated chloroform ($CDCl_3$), and thin layer chromatography (TLC) film gel F254, silica gel (60 mm) were purchased from Merck Millipore Company.

4-hydrazinobenzoic acid, Tricaprylylmethylammonium chloride (Aliquot 336), hexamethylphosphoramide acid (HMPA), 4-tert-butylpyridine, tetrabutylammonium hexafluorophosphate ($TBAPF_6$), 1-methyl-3-propylimidazolium iodide (PMII), Ferrocene (Fc), 1-bromohexane, neopentyl iodide, potassium hydroxide (KOH), o-phenylenediamine, nickel acetate ($Ni(OAc)_2.4H_2O$), titanium oxide (TiO_2), Fluorine doped Tin Oxide (FTO) glass, Polyethylene glycol tert-octylphenyl ether (Triton – X – 100), iodine (I_2) beads, and lithium iodide (LiI) were purchased from Sigma Aldrich Company. Ethanol, ether, concentrated sulphuric acid (H_2SO_4), tetrahydrofuran (THF), glacial acetic acid (AcOH), dimethylformamide (DMF), methanol (MeOH) were purchased from Friendemann Schmidt Company.

Deuterated pyridine (C_5D_5N), Chloroform ($CHCl_3$), ethyl acetate (EtOAc), dichloromethane (DCM), sodium hydrogen carbonate ($NaHCO_3$), sodium hydroxide (NaOH), 37% hydrochloric acid (HCl), tin chloride dihydrate ($Tin(II)Cl_2.\ 2H_2O$), and magnesium sulphate ($MgSO_4$) were purchased from Fisher Scientific company.

3.2 Instruments and sample preparations

3.2.1 Nuclear Magnetic Resonance (NMR) spectra

The NMR spectra for all synthesized compounds were recorded either on a JEOL ECXII 400 MHz or a JOEL 500 MHz using deuterated chloroform ($CDCl_3$) or pyridine (C_5D_5N) as solvent. The ^{13}C NMR spectra of some compounds could not be recorded due to solubility issues in deuterated solvent. The HSQC and HMBC spectra were recorded for compound **7c** only. The coupling constant (J) in the aromatic region of ^1H NMR spectra were reported in Hertz (Hz) units. All chemical shifts in the spectra are quoted as parts per million (ppm).

3.2.2 Elemental analyses and melting point.

The microanalysis of carbon, hydrogen and nitrogen elements for all synthesized compounds were done using a Pelkin Elmer 2400 II CHNS/O Elemental Analyzer. Acetanilide was used as an internal standard for all analyses. All measurements were taken under a constant flow of pure O_2 gas. The weight of sample used for analysis was ~ (1.5-2.0) mg. The melting point of all solid compounds were determined in an open thin glass capillary tube on a Mel-Temp II (LABORATORY DEVICES, USA) instrument and were not corrected.

3.2.3 Fourier Transform – Infrared (FT –IR) spectroscopy

The infrared spectra for all synthesized compounds were recorded using an ATR-FTIR Pekin - Elmer Spectrum 400 IR spectrophotometer in the range of wavenumber 4000 – 400 cm^{-1} at ambient temperature. The peaks observed in the spectrum were correlated to the possible functional group present in the compound.

3.2.4 Ultraviolet-Visible

The UV absorption spectra of all dyes were recorded in the region of 300 – 800 nm in 5.0 µM of DCM or AcOH solution at a slow scan rate measurements. The spectra were measured at room temperature using a Shimadzu UV-2600 UV-Vis Spectrophotometer in a 1.0 cm of quartz cuvette. All results are presented in terms of Absorbance (A) versus wavelength (λ, nm) units.

3.2.5 Crystallographic Analysis.

The diffraction data of compound **3** was collected on an Agilent Supernova Dual diffractometer (graphite-monochromated Mo- K_α radiation, λ = 0.71073 Å) at 293 K. The structure was solved using with the direct method by SHELXL-2014/7 and refined by the full-matrix least-square method on F^2 with SHELXL-2014/7. All the non-hydrogen atoms were refined anisotropically and all the C-bound hydrogen atoms were placed at calculated positions and refined isotropically. The XSEED was used for drawing the high-resolution image of the molecule. The Crystallographic Information File (CIF) was deposited in The Cambridge Crystallographic Data Centre (CCDC = 1574642) and free access *via* http://www.ccdc.cam.ac.uk.

3.2.6 Cyclic Voltammetry

Cyclic voltammetry (CV) was carried out on an AUTOLAB POTENTIOSTAT PGSTAT 12 (Ecochemie Netherlands) at room temperature. The high quality grade of DCM solvent (purity = 99.5%) was further pre-dried over 3 Å molecular sieve before used (Williams & Lawton, 2010). The dye **8a**, **8b** and **8c** were evaluated in DCM solution (c = 5×10^{-5} M) using a three basic compartments of electrochemical cell which are; a glassy carbon (GC) disc as the working electrode with a diameter of 2.0 mm size (A = 3.14×10^{-6} m^2), a Pt wire as the counter electrode and a normal Ag/AgCl as the reference electrode. The GC working electrode was first polished with alumina slurry, followed by washing several times with distilled water and acetone to remove any impurities on the electrode surface before used. The dye-sensitized photo-anode (FTO/TiO_2 /dye) of **9c** was replaced with GC as the working electrode due to solubility issues. The supporting electrolyte was 0.1 M of $TBAPF_6$ in DCM solution for all analyses. Before the voltammetry measurements, the solution was bubbled with N_2 gas for 10 minutes to displace dissolved oxygen. The oxidation potential value obtained in cyclic voltammetry measurement was calibrated with 1.0 mM of (Fc/Fc^+) as the external reference to determine the HOMO energy level value of the dyes.

3.2.7 DFT calculations

All computations analysis were done using the Gaussian 09 program suite. The structure was fully optimized at the ground state using hybrid Density Functional Theory (DFT) with B3LYP level of theory. All calculations were carried out in the gas phase using the 6-31G(d) basis set for C, H, N and O atoms while the LANL2DZ basis set was used for Ni atom which is includes an effective core potential (ECP). No imaginary frequency confirms that the geometry optimized corresponds to a stationary point with a virial theorem of -2.

3.2.8 DSSC Fabrication and Characterization

A FTO glass (14 $\Omega\ m^{-2}$) with dimension (3.0 cm × 2.5 cm) was pre-cleaned with acetone and EtOH before fabricating the film. The TiO_2 (P90) (0.5 g) powder was ground thoroughly in 0.1 M HNO_3 (2 mL) solution to form a slurry paste and then spin coated at 2650 rpm for 1 minute on the FTO substrates. The resulting first compact layer of photoanode film was sintered at 450 ^oC for 30 minutes in a furnace. Afterwards, a mixture of TiO_2 (P25) (0.5 g), 0.1 M HNO_3 (2 mL), carbowax (0.1 g) and 2 drops of Triton-X-100 was ground to form a homogeneous mixture. Subsequently, the paste was coated onto the first compact layer using a doctor-blade technique to obtain a second porous layer of

TiO_2 (Theerthagiri *et al.*, 2016). The film was sintered again at 450 °C for 30 minutes and then was left cooled to room temperature. Then, the prepared TiO_2 film was immersed in 0.2 mM in ($CHCl_3$ / MeOH = 2:1 ratio) solution of the **8a**, **8b** and **8c** dyes, whereas for dye **9c** it was immersed in 0.2 mM in (pyridine / MeOH = 3:7 ratio) solution for 24 hours respectively, at ambient temperature. All electrodes were rinsed several times with acetonitrile followed by drying of hot air-flow. The counter electrode, Pt coated FTO glass was prepared by drop casting a plasticol solution onto the cleaned FTO glass substrate and then was sintered at 450 °C for 30 minutes. To assemble DSSCs, each of the dye absorbed on the TiO_2 film electrode was placed on top of a Pt-coated electrode and tightly clipped together to form a sandwich structure. The electrolyte consisting of 0.1 M lithium iodide (LiI), 0.05 M iodide (I_2), 0.8 M 1-methyl-3-propylimidazolium iodide (PMII), and 0.5 M 4-tert-butylpyridine in acetonitrile solution (Huang *et al.*, 2015) was injected into the interspace between the two electrodes in the cell. The effective area of the fabricated dyes for analysis was 0.196 cm^2.

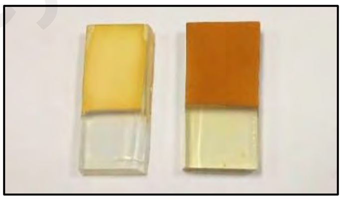

Figure 3.1: Comparison between the dyes **8c** (left) and **9c** (right) after attaching to photoanode (FTO / TiO_2) electrode.

The photovoltaic performance was measured using a solar simulator (Oriel LCS-100) irradiated under light intensity of 100 mW m^{-2} (AM 1.5G) sun illumination to obtain photocurrent density - voltage (*J*-V) curves for all devices. The solar to electricity conversion efficiency (PCE), η is calculated using the **Equation (3)** on page 26. Differences of Incident Photon to Current Efficiency (IPCE) between device **8c** and **9c** were evaluated using an optical power meter (Newport 1918-R) using a monochromator illumination (Newport Oriel Apex 70528). The Electrochemical Impedance Spectroscopy (EIS) analyses were obtained at open circuit voltage of 0.3V using the Potentiostat-Galvanostat (Metroohm Autolab PGSTAT128N, FRA32M) instrument at 100 mW cm^{-2} illumination.

3.3 Synthesis and characterizations

3.3.1 Synthesis of 2,3,3-trimethyl-3H-indole-5-carboxylic acid (1)

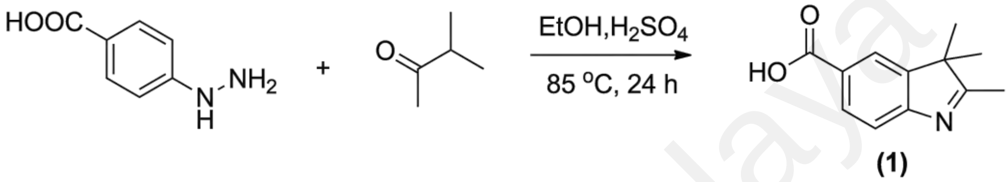

A mixture of 4-hydrazinobenzoic acid (4.01 g, 26.56 mmol), isopropyl methyl ketone (4.55 g, 52.91 mmol), and concentrated H_2SO_4 (0.8 mL) in freshly distilled EtOH (90 mL) was heated at 85 °C for 24 hours. After cooled to room temperature, the white crystalline solid was removed by filtration. Then, the solvent was evaporated into half from its original volume. Distilled water (40 mL) was added and the pH was changed to 10 - 11 with 1 M NaOH. The mixture was extracted with DCM (3×50 mL) for removal of by-products. The aqueous layer was collected and acidified to pH = 2-3 with 1 M HCl slowly. The precipitate formed was collected by extraction with DCM (5×100 mL). The organic extracts were washed with distilled water (3×100 mL), dried over anhydrous $MgSO_4$, filtered off, and concentrated under reduced pressure. The product was dried in an oven at 70 °C overnight to afford **(1)** (4.72 g, 89%) as a red – brownish solid. m.p. = 192-194 °C. ^{1}H NMR (400 MHz, $CDCl_3$): δ (ppm) = 1.34 (s, 6H, CH_3), 2.37 (s, 3H, CH_3), 7.67 (d, 1H, J = 8.0 Hz, Ar-H), 8.04 (d, 1H, J = 1.2 Hz, Ar-H), 8.12 (dd, 1H, J = 1.6, 8.2 Hz, Ar-H), 9.59 (bs, 1H, COOH). ^{13}C NMR (100 MHz, $CDCl_3$): δ (ppm) = 15. 49, 22.90, 53.96, 119.61, 123.30, 127.45, 130.85, 145.45, 156.81, 170.97, 192.73. IR (ATR): υ (cm^{-1}) = 2968*w*, 1684*m*, 1577*m*, 1423m, 1230*s*, 782*m*, 671*w*. Calcd for $C_{12}H_{13}NO_2$ = C, 70.92; H, 6.45; N, 6.89. Found: C, 70.65; H, 6.24; N, 6.73%. M_w = 202 gmol^{-1}.

3.3.2 Synthesis of 2,3,3-trimethyl-3H-indole-5-carboxylate ethyl ester (2)

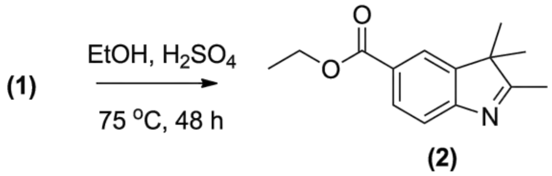

A mixture of 2,3,3-trimethylindolenine-5-carboxylic acid **(1)** (5.84 g, 28.73 mmol), concentrated H_2SO_4 (5.0 mL) in absolute EtOH (100 mL) was heated at 85 °C for 48 hours. After cooled to room temperature, the solvent was distilled off and distilled water (50 mL) was added into the mixture. The pH of aqueous solution was changed to 4 -5 by the slow addition of saturated $NaHCO_3$. Afterthat, the solution was extracted with EtOAc (3×50 mL). The organic layers were washed with distilled water (2×100 mL), dried over anhydrous $MgSO_4$, filtered and concentrated under reduced pressure. The crude product was further purified *via* silica gel column chromatography using a mixture of hexane and EtOAc (6:1, v/v) as eluent to afford **(2)** (3.83 g, 57%) as a purple sticky solid. m.p. = 68-70 °C. ^1H NMR (400 MHz, $CDCl_3$): δ (ppm) = 1.32 (s, 6H, CH_3), 1.37 (t, 3H, CH_3), 2.30 (s, 3H, CH_3), 4.34 (q, 2H, CH_2), 7.53 (d, 1H, J = 8 Hz, Ar-H), 7.95 (d, 1H, J = 2.0 Hz, Ar-H), 8.02 (dd, 1H, J = 2.0, 8.0 Hz, Ar-H). ^{13}C NMR (100 MHz, $CDCl_3$): δ (ppm) = 14.48, 15.81, 22.98, 53.95, 61.04, 119.65, 122.76, 127.36, 130.12, 145.76, 157.70, 166.93, 191.73. IR (ATR): υ (cm^{-1}) = 3048*w*, 2968*w*, 2935*w*, 1710*s*, 1571*m*, 1614*w*, 1571*m*, 1283*s*, 1235*s*, 1021*m*, 751*m*. Calcd for $C_{14}H_{17}NO_2$ = C, 72.70; H, 7.41; N, 6.06. Found: C, 72.30; H, 7.43; N, 6.43%. M_w = 231 $gmol^{-1}$.

3.3.3 Synthesis of 2-(diformylmethylidene)-3,3-dimethyl-2,3-dihydro-1H-indole-5-carboxylate ethyl ester (3).

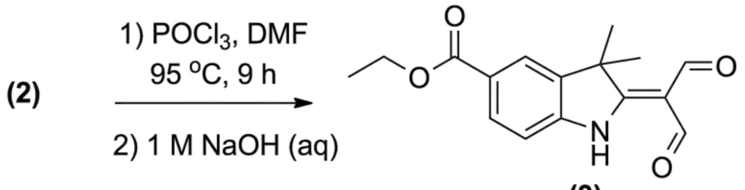

(3)

In an ice bath, a mixture of $POCl_3$ (4.64 mL, 50 mmol) and DMF (7.80 mL, 100 mmol) was stirred for 1 hour until the solution turned pale pink in colour. Then, the reagent was added slowly to another round bottom flask containing **(2)** (3.83 g, 16.56 mmol) in DMF (9 mL) for over 30 minutes at 0 °C. The mixture was heated at 95 °C for 9 hours. After the reaction was completed, the mixture was poured into 100 g of crushed ice. The resulting aqueous solution was slowly adjusted to pH = 9-10 with 2 M NaOH (aq). An excess amount of the latter will promote the ester hydrolysis. The purple sticky solid was filtered off and removed. The filtrate was left overnight at room temperature. The precipitate was obtained by filtration, then washed with hot distilled water, followed by drying in an oven at 70 °C to afford **(3)** (2.38 g, 50%) as an orange powder. A quality crystal for X-ray analysis was obtained from a DMF solution after 6 days at room temperature. m.p. = 166 °C. ^{1}H NMR (400 MHz, $CDCl_3$): δ (ppm) = 1.38 (t, 3H, CH_3), 1.77 (s, 6H, CH_3), 4.36 (q, 2H, CH_2), 7.19 (d, 1H, J = 7.7 Hz, Ar-H), 8.00 (d, 1H, J = 1.6 Hz, Ar-H), 8.03 (dd, 1H, J = 1.6, 6.6 Hz, Ar-H), 9.83 (s, 2H, CHO), 13.50 (bs, 1H, NH). ^{13}C NMR (100 MHz, $CDCl_3$): δ (ppm) = 14.46, 23.82, 51.15, 61.39, 110.09, 112.14, 123.70, 127.88, 130.84, 140.65, 143.24, 165.97, 180.06, 187.69, 192.65. IR (ATR): υ (cm^{-1}) = 3156*w*, 2981w, 1700*s*, 1600*s*, 1607*s*, 1531*s*, 1466*m*, 1353*m*, 1286*s*, 1215*s*, 1101*s*, 760*s*. Calcd for $C_{16}H_{17}NO_4$ = C, 66.89; H, 5.96; N, 4.88. Found: C, 66.63; H, 6.04; N, 4.80%. M_w= 287 gmol^{-1}.

3.3.4 Synthesis of 1,2-bis(hexyloxy) benzene (4b)

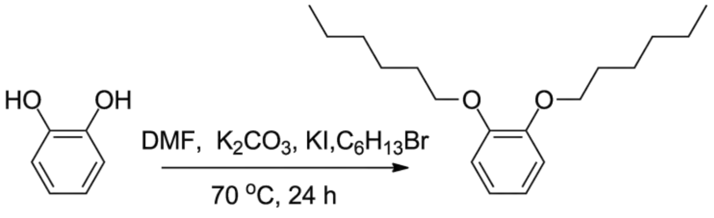

(4b)

A mixture of catechol (1.50 g, 13.64 mmol), anhydrous K_2CO_3 (4.71 g, 34.10 mmol), 1-bromohexane (5.63 g, 34.10 mmol), and 1 small spoon of KI in dry DMF (5 mL) was heated at 70 °C for 24 hours. The completion of the reaction was monitored by TLC until all reactants were consumed. After cooled to room temperature, distilled water was added (100 mL) into the mixture. The aqueous solution was extracted with EtOAc (3×50 mL). The combined extracts were washed with distilled water (3×100 mL), dried over anhydrous $MgSO_4$, filtered and concentrated under reduced pressure. The crude product was purified by flash column chromatography on silica gel using a mixture of hexane and ether (19:1, v/v) as eluent to afford (**4b**) (0.98 g, 26%) as a colorless liquid product. ^{1}H NMR (400 MHz, $CDCl_3$): δ (ppm) = 0.88 (t, 6H, CH_3), 1.31 (m, 8H, CH_2), 1.44 (quin, 4H, CH_2), 1.77 (quin, 4H, CH_2), 3.97 (t, 4H, CH_2), 6.87 (s, 4H, Ar-H). ^{13}C NMR (100 MHz, $CDCl_3$): δ (ppm) = 14.10, 22.71, 25.81, 29.41, 31.70, 69.37, 114.21, 121.09, 149.34. IR (ATR): υ (cm^{-1}) = 2953*m*, 2929*m*, 2859*m*, 1593*m*, 1501*m*, 1251*s*. 1221*m*, 737*s*. Elemental analysis could not be measured because of the difficulty for packing the sample in the liquid form. M_w = 278 gmol^{-1}.

3.3.5 Synthesis of 1,2- bis(neopentyloxy) benzene (4c)

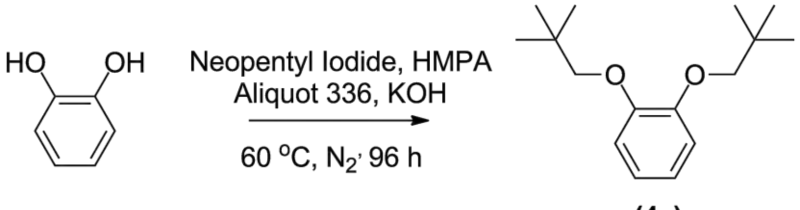

(4c)

In the dark condition, a mixture of HMPA (11 mL), KOH (2.30 g, 41 mmol), catechol (1.50 g, 13.64 mmol), Aliquot 336 (0.6 mL) and neopentyl iodide (4.2 mL, 31.68 mmol) was heated at 70 °C for 96 hours under N_2 atmosphere. The completion of the reaction was monitored by TLC until all reactants were consumed. After being cooled down to room temperature, distilled water (200 mL) was added into the mixture. The aqueous solution was extracted with EtOAc (3×100 mL), washed with distilled water (3×100 mL) and brine solution. The combined extracts were dried over anhydrous $MgSO_4$, filtered and dried under reduced pressure. The crude product was further purified by flash column chromatography using a mixture of hexane and ether (19:1, v/v) as eluent to give (**4c**) (2.04 g, 60%) as a colourless liquid product. ^{1}H NMR (400 MHz, $CDCl_3$): δ (ppm) = 1.06 (s, 18H, CH_3), 3.61 (s, 4H, CH_2), 6.85 (s, 4H, Ar-H). ^{13}C NMR (100 MHz, $CDCl_3$): δ (ppm) = 26.77, 32.21, 78.77, 113.37, 120.73, 149.68. IR (ATR): υ (cm^{-1}) = 2954*m*, 2927*m*, 2867*m*, 1592*m*, 1492*m*, 1251*s*, 1224*m*, 1017*m*, 738*m*. Elemental analysis could not be measured because of the difficulty for packing the sample in the liquid form. M_w = 250 gmol^{-1}.

3.3.6 Synthesis of 1,2-bis(hexyloxy)-4,5-dinitrobenzene (5b)

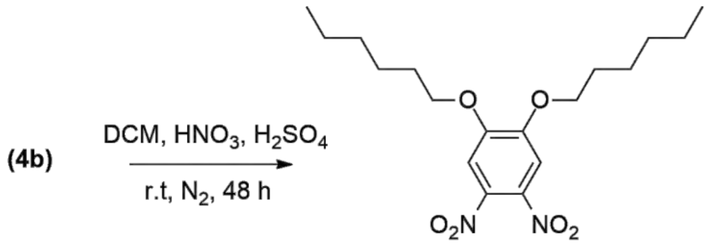

(5b)

In an ice-cooled bath, a mixture of 1,2-bis(hexyloxy) benzene **(4b)** (6.30 g, 22.64 mmol) and concentrated HNO_3 (30 mL) in DCM (40 mL) was stirred under N_2 atmosphere within 30 minutes. Then, a catalytic amount of concentrated H_2SO_4 (15 mL) was added slowly to the reaction mixture within 15 minutes. The mixture was stirred vigorously at room temperature for 48 hours. After completion, the mixture was poured into ice water followed by extraction with DCM (3×100 mL). The combined extracts were washed with saturated $NaHCO_3$ (aq) (50 mL) and several times with distilled water. The organic phase was dried over anhydrous $MgSO_4$, filtered off and evaporated to dryness. The crude product was further recrystallized from hot EtOH to afford **(5b)** (4.60 g, 44%) as a bright yellow precipitate. m.p = 92 – 94 °C. ^{1}H NMR (500 MHz, $CDCl_3$): δ (ppm) = 0.87 (t, 6H, CH_3), 1.30 (m, 8H, CH_2), 1.45 (quin, 4H, CH_2), 1.80 (quin, 4H, CH_2), 4.05 (t, 4H, CH_2), 7.26 (s, 2H, Ar-H) ^{13}C NMR (125 MHz, $CDCl_3$): δ (ppm) = 14.00, 22.57, 25.52, 28.71, 31.42, 70.26, 107.94, 136.50, 151.87. IR (ATR): υ (cm^{-1}) = 3070*w*, 2932*m*, 2860*m*, 1528*s*, 1464*m*, 1371*m*, 1353*m*, 1224*m*, 1038*m*, 872*m*, 720*w*. Calcd for $C_{18}H_{28}N_2O_6$ = C, 58.68; H, 7.66; N, 7.60. Found = C, 58.46; H, 7.53; N, 7.56%. M_w = 368 $gmol^{-1}$.

3.3.7 Synthesis of 1,2-bis(neopentyloxy)-4,5-dinitrobenzene (5c)

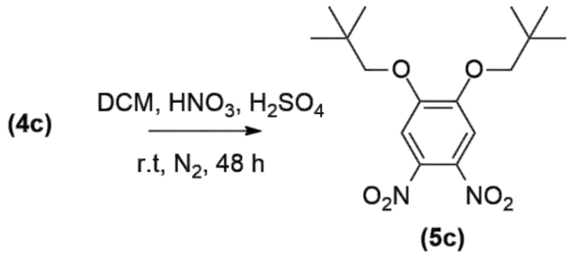

In an ice-cooled bath, a mixture of 1,2- bis(neopentyloxy) benzene **(4c)** (2.04 g, 8.15 mmol) and concentrated HNO_3 (20 mL) in DCM (15 mL) was stirred under N_2 atmosphere within 30 minutes. Then, a catalytic amount of concentrated H_2SO_4 (7 mL) was added slowly to the reaction mixture within 15 minutes. The mixture was stirred vigorously at room temperature for 48 hours. After completion, the solution was poured into ice water, followed by extraction with DCM (3×50 mL). The combined organic phases were washed with saturated $NaHCO_3$ (aq) (20 mL) once and several times with distilled water. The organic phase was dried over anhydrous $MgSO_4$, filtered and evaporated under reduced pressure. The crude product was further recrystallized from hot EtOH to afford **(5c)** (2.35 g, 85%) as a large yellow needle crystal. m.p = 165-166 ^{o}C. ^{1}H NMR (400 MHz, $CDCl_3$): δ (ppm) = 1.07 (s, 18H, CH_3), 3.71 (s, 4H, CH_2), 7.25 (s, 2H, Ar-H). ^{13}C NMR (100 MHz, $CDCl_3$): δ (ppm) = 26.49, 32.21, 79.41, 107.41, 136.47, 152.15. IR (ATR): υ (cm^{-1}) = 3072*w*, 2959*m*, 2872*m*, 1520*s*, 1477*w*, 1364*m*, 1335*m*, 1043*m*, 1226*s*, 816*s*, 718*w*. Calcd for $C_{16}H_{24}N_2O_6$ = C, 56.46; H, 7.11; N, 8.23. Found: C, 56.43; H, 7.08; N, 8.18%. M_w = 340 gmol^{-1}.

3.3.8 Synthesis of macrocyclic ligand 7a

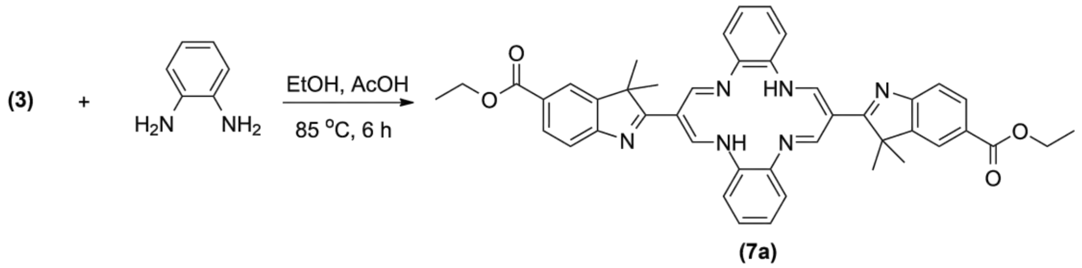

A mixture of **(3)** (100 mg, 0.35 mmol), *o*-phenylene-diamine (40 mg, 0.37 mmol), AcOH (0.1 mL) and EtOH (10 mL) was refluxed for 6 hours. After being cooled to room temperature, the precipitate was filtered off, washed with hot 50% EtOH (aq) and dried in an oven at 70 °C to yield (**7a**) (137 mg, 88%) as an orange powder. m.p = 324 °C. ^1H NMR (400 MHz, $CDCl_3$): δ (ppm) = 1.39 (t, 6H, CH_3), 1.61 (s, 12H, CH_3), 4.36 (q, 4H, CH_2), 7.16 (m, 4H, Ar-H), 7.36 (m, 4H, Ar-H), 7.49 (d, 2H, J = 8.4 Hz, Ar-H), 7.96 (d, 2H, J = 1.2 Hz, Ar-H), 8.03 (dd, 2H, J = 2, 8 Hz, Ar-H), 8.96 (d, 4H, J = 6.4 Hz, CNH), 14.62 (t, 2H, J = 6.4 Hz, NH). ^{13}C NMR (100 MHz, $CDCl_3$): δ (ppm) = 14.55, 26.30, 52.48, 60.95, 104.48, 115.57, 118.46, 122.16, 126.04, 126.49, 130.47, 137.39, 146.54, 150.59, 157.60, 167.06, 185.28. IR (ATR): υ (cm^{-1}) = 2960*w*, 1707*m*, 1635*s*, 1611*m*, 1488*m*, 1312*m*, 1291*s*, 1230*s*, 777*m*, 727*m*. Calcd for $C_{44}H_{42}N_6O_4$ = C, 73.52; H, 5.89; N, 11.69. Found: C, 73.42; H, 5.87; N, 11.88%. M_w = 719 $gmol^{-1}$.

3.3.9 Synthesis of macrocyclic ligand 7b

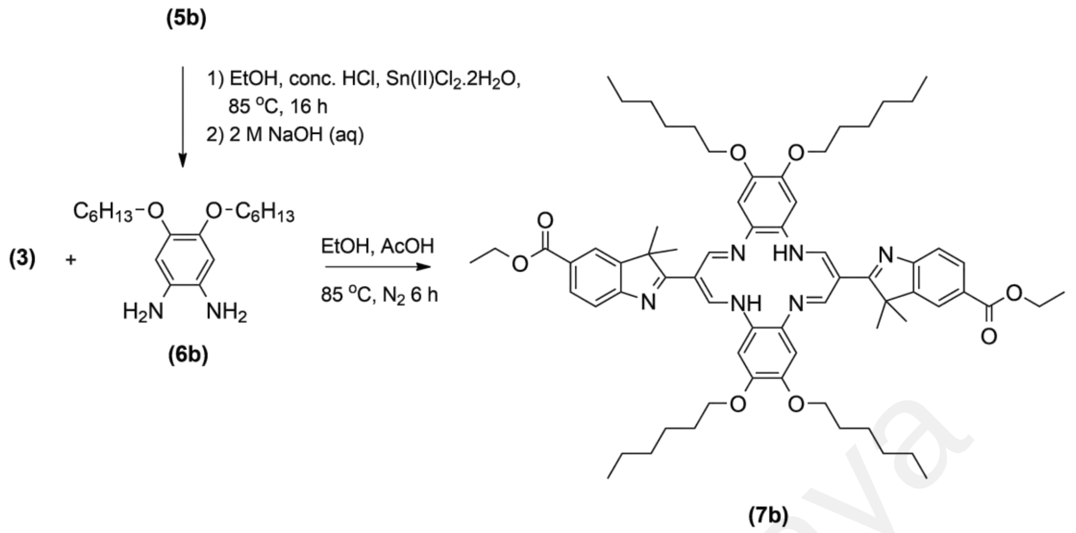

In a two neck round-bottom flask, 1,2-bis(hexyloxy)-4,5-dinitrobenzene **(5b)** (934 mg, 2.78 mmol) was dissolved in freshly distilled EtOH (40 mL) under N_2 atmosphere. After 15 minutes, 37% HCl (18.0 mL) and Sn(II)Cl_2.2H_2O (5.02 g, 22.24 mmol) in 10 mL of EtOH were added to the mixture. The clear orange solution was refluxed for 16 hours. Upon cooling to 40 °C, 100 mL of DCM was added and the mixture was slowly adjusted to pH = 10 - 11 with 2 M NaOH (aq) under vigorous stirring. The organic layer was separated and the resulting white suspension in the aqueous layer was further extracted with DCM (2×100 mL). The combined organic extract was washed with distilled water (100 mL) once, dried over anhydrous $MgSO_4$, filtered off and concentrated under reduced pressure to obtain **(6b)** as a yellow - greenish liquid. Owing to its instability, the impure product was used directly in the next step without purification to react with **(3)** (400 mg, 1.39 mmol) in absolute EtOH (50 mL) in the presence of glacial AcOH (0.2 mL) under N_2 atmosphere. After 6 hours of reflux, the precipitate was filtered off, washed with hot 50% EtOH (aq) and dried at 70 °C to afford **(7b)** (590 mg, 76%) as a red-brownish powder. The percentage yield was calculated based on **(3)** as the limiting reagent. m.p = 270-271°C. ^{1}H NMR (400 MHz, $CDCl_3$): δ (ppm) = 0.92 (t, 12H, CH_3), 1.35-1.38 (quin, 16H, CH_2), 1.39-1.42 (t, 6H, CH_3-ester), 1.47 (quin, 8H, CH_2), 1.61 (s, 12H, CH_3), 1.81 (quin, 8H, CH_2), 4.05 (t, 8H, CH_2), 4.36 (q, 4H, CH_2-ester), 6.86 (s, 4H, Ar-H), 7.50 (d, 2H, *J* = 8.4 Hz, Ar-H), 7.94 (d, 2H, *J* = 1.2, Ar-H), 8.02 (dd, 2H, *J* = 1.6, 8.2 Hz, Ar-H), 8.76 (s, 4H, CHN), 15.05 (bs, 2H, NH). ^{13}C NMR (125 MHz, $CDCl_3$): δ (ppm) = 14.17, 14.54, 22.74, 25.88, 26.44, 29.47, 31.77, 52.26, 60.88, 69.93, 101.25, 103.93, 117.88, 122.02, 125.61, 130.44, 130.72, 146.22, 148.37, 148.76, 157.55, 167.11, 185.19. IR (ATR): υ (cm^{-1}) = 2954*w*, 2928*w*, 2861*w*, 1706*m*, 1634*m*, 1608*m*, 1465*m*, 1291*s*, 1227*s*, 835*m*, 776*m*. Calcd for $C_{68}H_{90}N_6O_8$ = C, 72.96; H, 8.10; N, 7.51. Found: C, 73.04; H, 8.32; N, 7.28%. M_w = 1119 gmol^{-1}.

3.3.10 Synthesis of macrocyclic ligand 7c

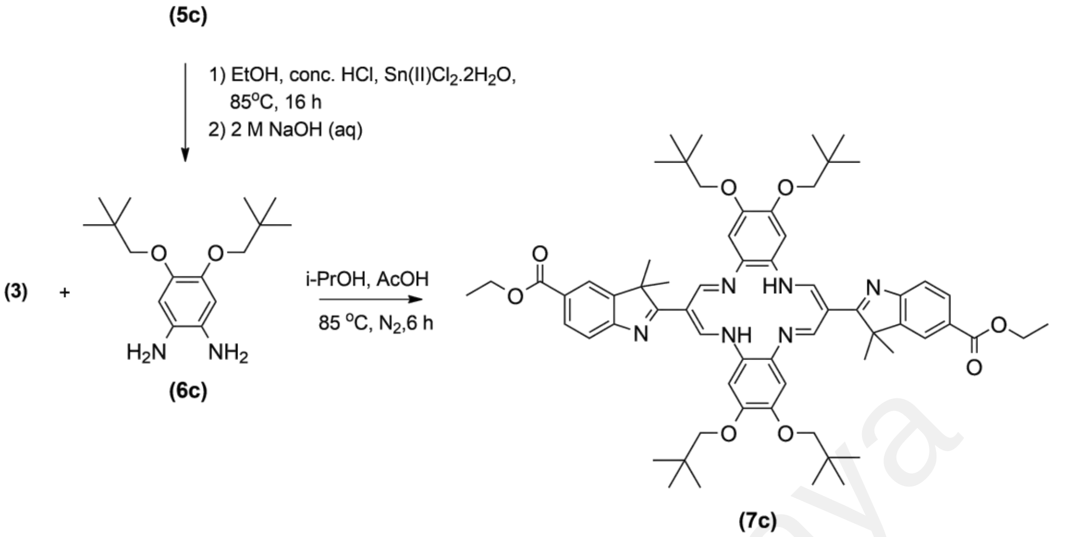

In a two neck round-bottom flask, 1,2-bis(neopentyloxy)-4,5-dinitrobenzene **(5c)** (356 mg, 1.05 mmol) was dissolved in freshly distilled EtOH (25 mL) under N_2 atmosphere. After 15 minutes, 37% HCl (7.32 mL) and Sn(II)Cl_2.$2H_2O$ (1.89 g, 8.38 mmol) in EtOH (10 mL) were added to the reaction mixture. The clear orange solution was refluxed for 16 hours. Upon cooling to 50 °C, 100 mL of DCM was added and the mixture was slowly adjusted to pH = 10 – 11 with 2 M NaOH (aq) under vigorous stirring. The organic layer was separated and the resulting white suspension in the aqueous layer was further extracted with DCM (2×100 mL). The combined organic extract was washed with 100 mL of distilled water once, dried over anhydrous $MgSO_4$, filtered off and concentrated under reduced pressure to obtain **(6c)** as a yellow-greenish liquid. Owing to its instability, the impure product was used directly in the next step without purification to react with **(3)** (150 mg, 0.52 mmol) in *i*-PrOH (20 mL) in the presence of glacial AcOH (0.2 mL) under N_2 atmosphere. After 6 hours of reflux, the precipitate was filtered off, washed with hot 50% EtOH (aq) and dried at 70 °C to give **(7c)** (200 mg, 72%) as a dark-red powder. m.p > 320 °C. ^{1}H NMR (400 MHz, $CDCl_3$): δ (ppm) = 1.05 (s, 36H, CH_3), 1.39 (t, 6H, CH_3-ester), 1.57 (s, 12H, CH_3), 3.66 (s, 8H, CH_2), 4.35 (q, 4H, CH_2-ester), 6.78 (s, 4H, Ar-H), 7.51 (d, 2H, J = 8.4 Hz, Ar-H), 7.94 (d, 2H, J = 1.6 Hz, Ar-H), 8.02 (dd, 2H, J = 1.6, 8.0 Hz, Ar-H), 8.67 (s, 4H, CHN), 15.08 (t, 2H, J = 6.4 Hz, NH). ^{13}C

NMR (100 MHz, $CDCl_3$): δ (ppm) = 14.54, 26.28, 26.71, 32.26, 52.38, 60.91, 79.18, 100.59, 104.01, 118.06, 122.19, 125.74, 130.52, 130.61, 146.44, 148.78, 148.92, 157.73, 167.08, 185.83. IR (ATR): υ (cm^{-1}) = 2951*w*, 2904*w*, 1708*w*, 1634*m*, 1609*m*, 1493*m*, 1317*m*, 1246*s*, 1222*s*, 1013*m*, 922*w*. Calcd for $C_{64}H_{82}N_6O_8$ = C, 72.29; H, 7.77; N, 7.90. Found: C, 71.86; H, 7.62; N, 7.77%. M_w = 1063 $gmol^{-1}$.

3.3.11 Synthesis of macrocyclic nickel complex 8a

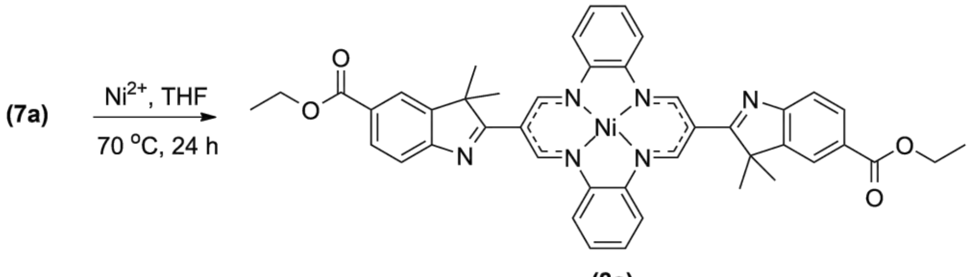

(8a)

A solution of Ni(OAc)$_2$.4H$_2$O (15.6 mg, 0.063 mmol) in a minimum amount of solvent containing glacial AcOH and water (10 : 1, v/v) was added into (30 mg, 0.042 mmol) **(7a)** in hot THF (12 mL). The mixture was heated at 70 ^{o}C for 24 hours. After cooled to room temperature, the precipitate was collected, washed with hot THF, EtOH, water and dried at 70 ^{o}C to give **(8a)** (22.2 mg, 69%) as an orange - red powder. m.p > 320 ^{o}C. ^{1}H NMR (400 MHz, CDCl$_3$): δ (ppm) = 1.40 (t, 6H, CH$_3$-ester), 1.64 (s, 12H, CH$_3$), 4.37 (q, 4H, CH$_2$-ester), 7.07 (m, 4H, Ar-H), 7.41 (d, 2H, J = 8.0 Hz, Ar-H), 7.54 (m, 4H, Ar-H), 7.97 (s, 2H, Ar-H, overlapped), 7.99 (d, 2H, J = 8.4 Hz, Ar-H, overlapped), 8.84 (s, 4H, CHN). IR (ATR): υ (cm^{-1}) = 2960*w*, 1705*m*, 1603*m*, 1581*m*, 1489s, 1374*m*, 1287*s*, 1220*s*, 737*m*, 724*m*. Calcd for C$_{44}$H$_{40}$N$_6$NiO$_4$ = C, 68.14; H, 5.20; N, 10.84. Found: C, 67.96; H, 5.28; N, 10.63%. M$_w$ = 776 gmol^{-1}. Due to its poor solubility and strong molecular aggregation in deuterated solvent, ^{13}C NMR measurement could not be recorded.

3.3.12 Synthesis of macrocyclic nickel complex 8b

(7b)

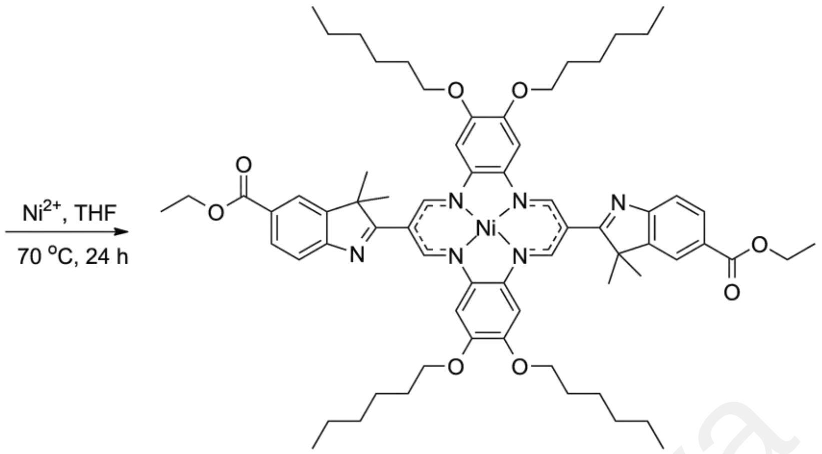

(8b)

A solution of $Ni(Oac)_2.4H_2O$ (22 mg, 0.089 mmol) in a minimum amount of solvent containing glacial AcOH and water (10 : 1, v/v) was added into **(8b)** (53 mg, 0.047 mmol) in hot THF (6 mL). The mixture was heated at 70 °C for 24 hours. After cooled to room temperature, the precipitate was collected, washed with hot THF, EtOH, distilled water and dried at 70 °C to afford **(8b)** (41.2 mg, 74%) as a brown - reddish powder. m.p = 294-296 °C. ^{1}H NMR (400 MHz, $CDCl_3$): δ (ppm) = 0.91 (br, 12H, CH_3), 1.35 (br, 30H, overlapped CH_2 & CH_3-ester), 1.61 (s, 12H, CH_3), 1.78 (br, 8H, CH_2), 3.99 (br, 8H, CH_2), 4.38 (br, 4H, CH_2-ester), 6.97 (s, 4H, Ar-H), 7.42 (br, 2H, Ar-H), 7.94 (br, 4H, overlapped Ar-H), 8.40 (s, 4H, CHN). ^{13}C NMR (125 MHz, $CDCl_3$): δ (ppm) = 14.24, 14.56, 22.78, 25.96, 26.25, 29.60, 31.93, 52.04, 60.77, 69.25, 98.62, 107.05, 116.94, 121.67, 124.77, 130.32, 137.55, 144.62, 145.56, 147.88, 156.98, 167.26, 184.08. IR (ATR): υ (cm^{-1}) = 2927*m*, 2860*m*, 1705*m*, 1603*m*, 1591*m*, 1498*s*, 1463*s*, 1375*m*, 1287*s*, 1220*s*, 1193*s*, 1102*m*, 777*m*, 545*m*. Calcd for $C_{68}H_{88}N_6NiO_8$ = C, 69.44; H, 7.54; N, 7.15. Found: C, 69.24; H, 7.32; N, 7.07%. M_w = 1176 gmol^{-1}.

3.3.13 Synthesis of macrocyclic nickel complex 8c

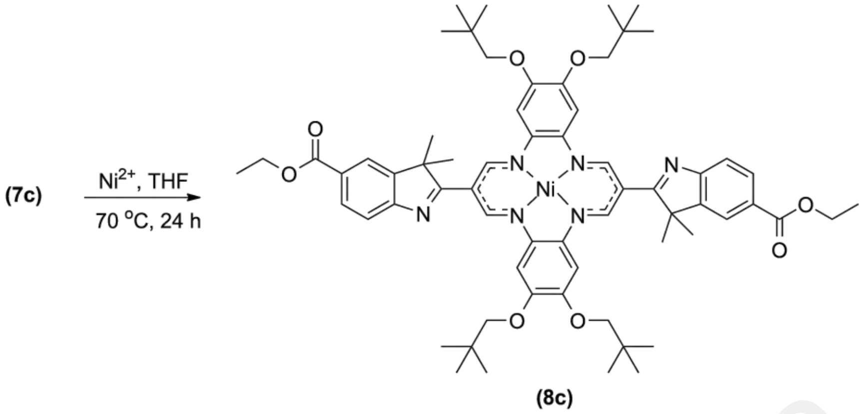

(8c)

A solution of $Ni(OAc)_2.4H_2O$ (64 mg, 0.089 mmol) in a minimum amount of solvent containing glacial acetic acid and water (1 : 1, v/v) was added into **(7c)** (200 mg, 0.047 mmol) in hot THF (12 mL). The solution was heated at 70 °C for 24 hours. After completion, the solvent was evaporated to half from original volume. The precipitate was collected after being cooled down to room temperature, then washed with hot 50% EtOH (aq) and dried at 70 °C to afford **(8c)** (187 mg, 89%) as a brown powder. m.p > 320 °C. ^{1}H NMR (400 MHz, $CDCl_3$): δ (ppm) = 0.96 (s, 36H, CH_3), 1.39 (t, 6H, CH_3-ester), 1.51 (s, 12H, CH_3), 3.59 (s, 4H, CH_2), 4.36 (q, 4H, CH_2-ester), 6.92 (br, 4H, Ar-H), 7.67 (d, 2H, *J* = 5.6 Hz, Ar-H), 7.93 (s, 2H, Ar-H), 8.04 (dd, 2H, *J* = 1.6, 7.6 Hz , Ar-H), 8.26 (br, 4H, CHN). ^{13}C NMR (100 MHz, $CDCl_3$): δ (ppm) = 14.55, 25.95, 26.50, 31.98, 52.68, 60.93, 78.57, 98.30, 107.80, 118.22, 122.24, 125.72, 130.61, 137.66, 144.95, 146.24, 148.17, 157.43, 167.12, 186.02. IR (ATR): υ (cm^{-1}) = 2952w, 2901*w*, 2865*w*, 1707*m*, 1603*m*, 1591*m*, 1491*s*, 1462*m*, 1375*m*, 1222*s*, 1193*s*, 1024*m*, 818*w*, 554*w*. Calcd for $C_{68}H_{80}N_6NiO_8$ = C, 68.83; H, 7.20; N, 7.50. Found: C, 68.47; H, 7.47; N, 7.53%. M_w = 1120 $gmol^{-1}$.

3.3.14 Synthesis of macrocyclic nickel 9c

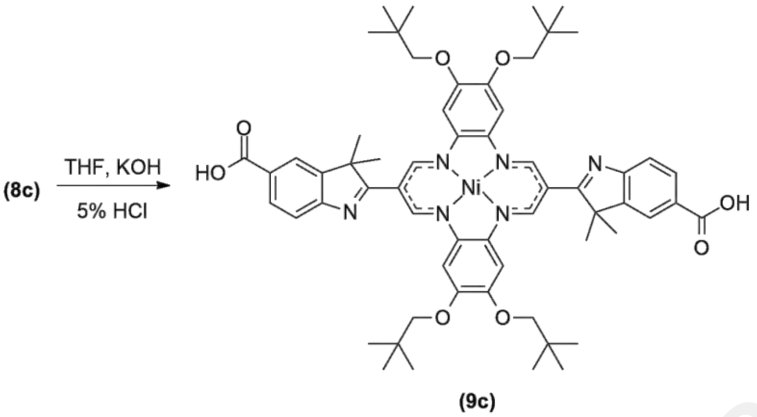

(9c)

A mixture of **(8c)** (15 mg, 0.013 mmol), methanolic KOH (1 mL) (15 mg, 0.267 mmol) in hot THF (13 mL) was refluxed for 30 hours. After completion, the solvent was partially evaporated by heating followed by addition of distilled water (3 mL) into the mixture. The dark-red clear aqueous solution was stirred at room temperature for another 30 minutes and then it was acidified with 5% HCl to pH = 2-3. The resulting precipitate formed was collected by filtration, washed with hot 50% EtOH (aq) and dried at 70 ºC to afford **(9c)** (11 mg, 77%) as a dark-brownish powder. m.p > 320 ºC. ^{1}H NMR (400 MHz, C_5D_5N): δ (ppm) = 1.08 (s, 36H, CH_3), 1.63 (s, 12H, CH_3), 3.74 (s, 8H, CH_2), 7.26 (s, 4H, Ar-H), 7.75 (d, 2H, J = 8.4 Hz, Ar-H), 8.51 (s, 2H, Ar-H), 8.52 (s, 2H, Ar-H), 8.75 (s, 4H, CHN). IR (ATR): υ (cm^{-1}) = 2955*m*, 2901*m*, 2868*m*, 1689*m*, 1603*m*, 1589*m*, 1493*s*, 1462*s*, 1374*s*, 1183*s*, 1008*m*, 749*m*. Calcd for $C_{60}H_{72}N_6NiO_8$ = C, 67.73; H, 6.82; N, 7.90. Found: C, 67.37; H, 7.03; N, 7.66%. M_w = 1064 gmol^{-1}. Due to its poor solubility and strong molecular aggregation in deuterated solvent, ^{13}C NMR measurement could not be recorded.

CHAPTER 4: RESULTS AND DISCUSSION

4.1 Synthesis

The synthesis pathway of all Ni-DBTAA dyes is illustrated in **Figure 4.1**. The Fisher - Indole cyclization of compound **1** was prepared following the procedure reported in the literature (Tomasulo *et al.*, 2007) to afford the desired product in 89% yield. Yet, the attempt to substitute the diformyl group of compound 1 *via* the Vilsmeier-Haack reaction was unsuccessful.

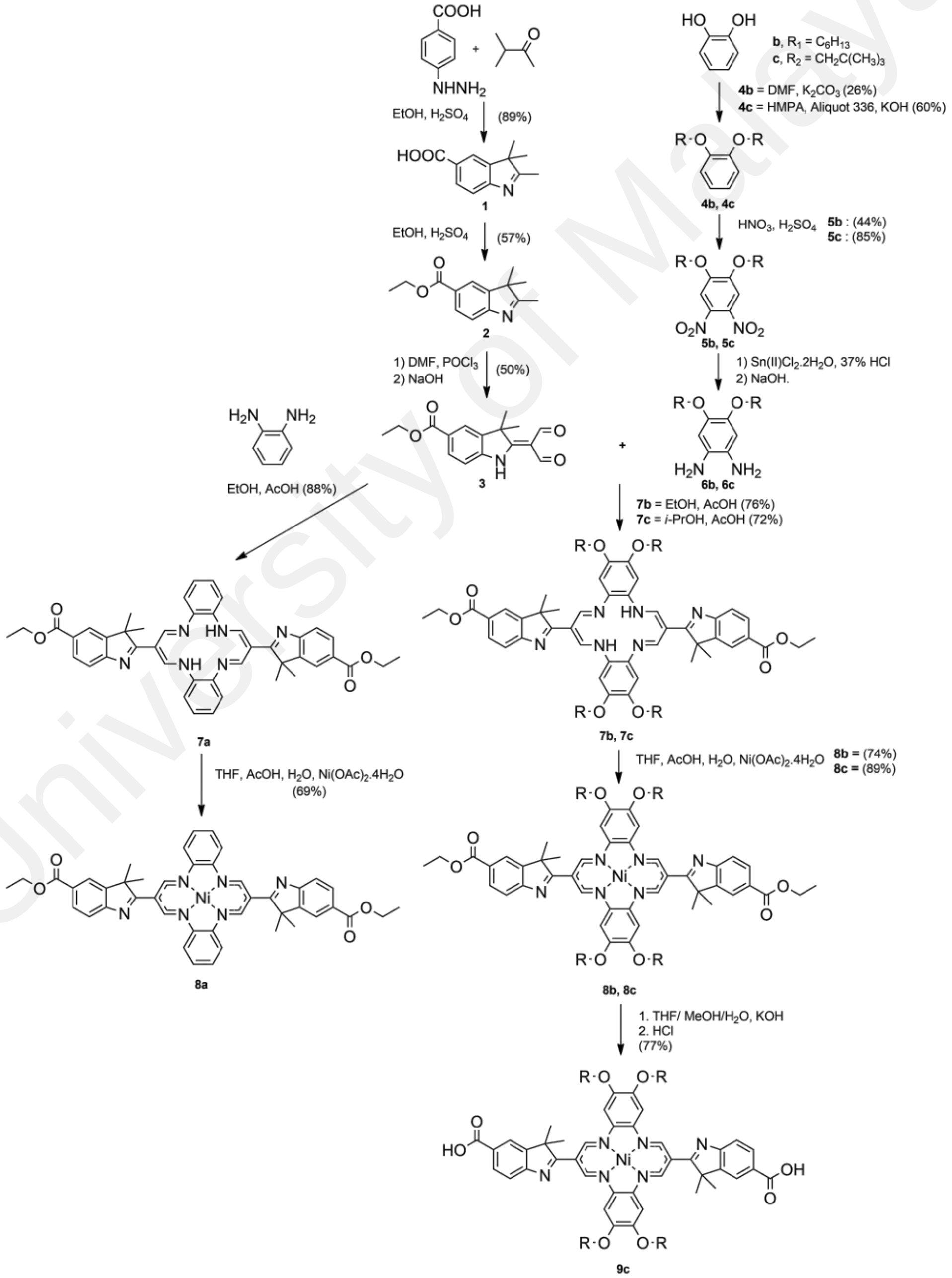

Figure 4.1: Synthesis route of all dyes.

Therefore, the carboxyl group was protected as an ethyl ester by reacting **1** with EtOH in the presence of concentrated H_2SO_4. The pure compound **2** was isolated *via* column chromatography with yield 57%. The Vilsmeier-Haack reaction of ester successfully substituted a diformyl group on the indolenine moiety (Rashidi *et al.*, 2009). Basification of the reaction mixture using NaOH was done slowly to avoid undesirable side reaction, such as hydrolysis of the NH indole or ester groups. The proposed mechanism for the formation of compound **3** is illustrated in **Figure 4.2**, showing the reaction between $POCl_3$ and DMF forming an electrophilic iminium cation. The electrophile was attacked by the nucleophilic indolium compound, substituting di–N-ethylidene-N-methylmethanaminium chloride at the methylene position. The intermediate stage of compound underwent a basic hydrolysis for the removal of two dimethylammonium chloride to give compound **3** (Baradarani *et al.*, 2006) in 50% yield.

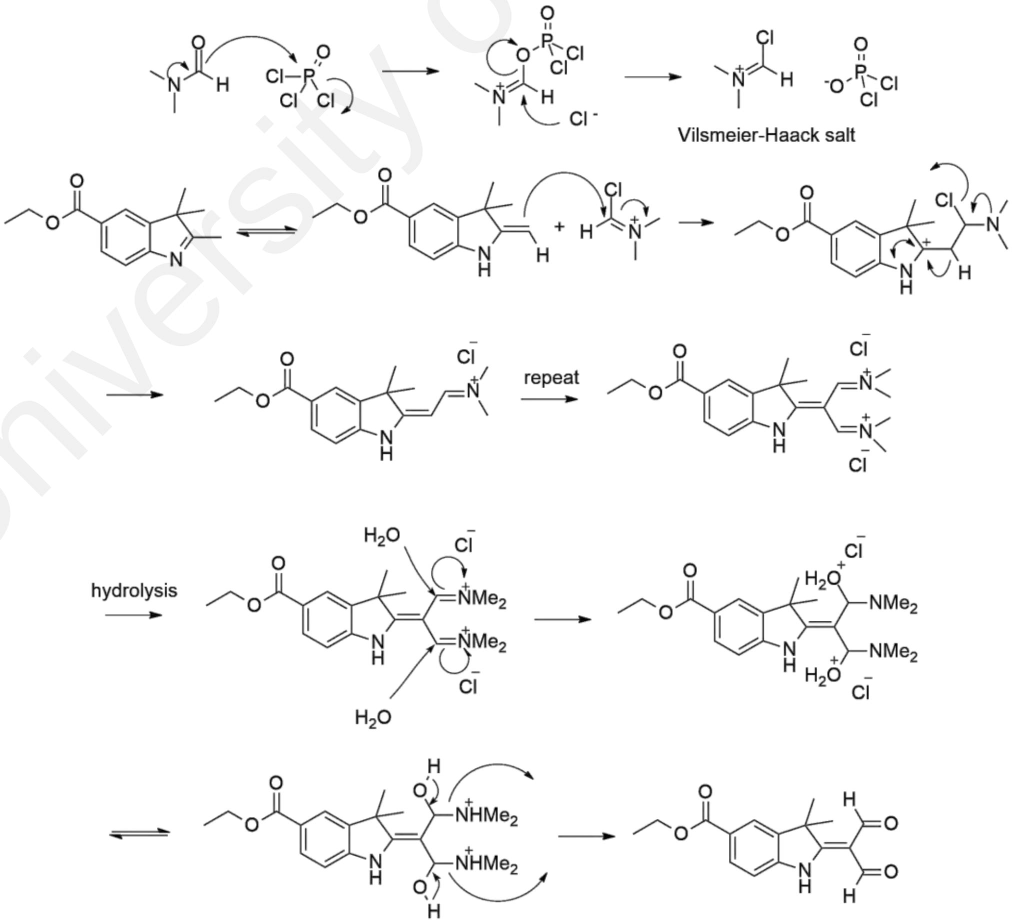

Figure 4.2: Proposed mechanism for the formation of **3**.

On the other hand, the alkylation of catechol **4b** and **4c** were synthesized following two different reported procedures. Compound **4b** was successfully synthesized using a mixture of hexyl bromide, KI, and K_2CO_3 in DMF as solvent media (Nagarjuna *et al.*, 2012). However, it was found unsuccessful when the same procedure was employed for the synthesis of compound **4c** using neopentyl iodide. Thus, a different approach which involved the use of a mixture containing HMPA, Aliquot 336, KOH and neopentyl iodide was applied to produce compound **4c** (Khanamiryan *et al.*, 2000) in 60% yield. Both compounds of **4b** and **4c** were subjected to a nitration reaction, producing compound **5b** and **5c,** respectively in good yields.

The diamines **6b** and **6c** were obtained by performing the reduction on the di-nitro compound **5b** and **5c** according to a modified procedure (Perrin & Hudhomme, 2011). As the diamines are highly unstable and easily decompose at room temperature, the compounds were used for the subsequent reaction with compound **3** in [2:2] equimolar ratios without prior purification, respectively to produce a new series of DBTAA ligand **7a** -**7c**, in 72-88 % yields. The NH protons of the inner macrocyclic appeared as a triplet within the range of δ = 14-15 ppm in the ^{1}H NMR spectra. The formation of ligands were achieved by the migration of double bonds from pyrrole ring into the inner core of macrocyclic to stabilize the whole structure as shown in **Figure 4.3** (Faraj *et al.*, 2014; Khaledi *et al.*, 2013). All ligands exhibited good solubility in chloroform, DCM, THF, dioxane, pyridine, and AcOH solvents, and high stability at room temperature.

The metalation reaction of each macrocyclic ligand with an excess amount of Ni^{2+} in THF solvent tended to form a single product of the metal complex, **8a**, **8b**, and **8c**. The successful incorporation of metal ion into the macrocyclic core by forming a square-planar complex was confirmed based on the disappearance of the characteristic NH signal in the ^1H NMR spectrum. Among of the three complexes, only compound **8c** was able to undergo ester hydrolysis reaction under a strong basic condition to yield the final compound **9c** in 77% yield**.** Regrettably, the ester cleavage for compounds **8a** and **8b** were unsuccessful due to their poor solubility in the reaction media. Structure elucidation of all intermediates and final compounds were done based on the analysis of their respective NMR and IR spectra. Unfortunately, it was unsuccessful to grow any quality single crystal of ligands or metal complexes for further characterization by X-ray crystallography analysis. Hence, microanalysis was conducted and the data obtained are consistent with the proposed structures.

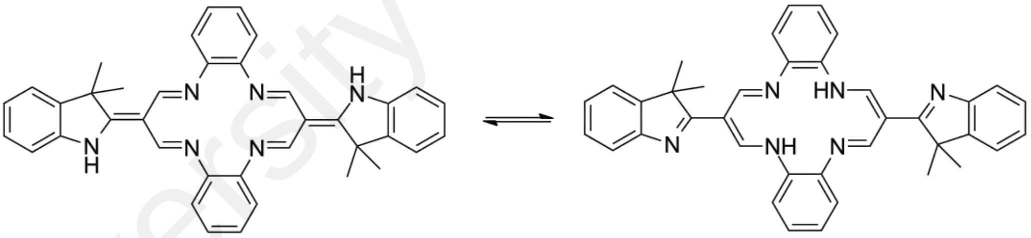

Figure 4.3: Tautomerism structures of indolenine DBTAA ligand.

4.2 Crystal structure of 3

The crystal structure of **3** as shown in **Figure 4.4** was obtained from a DMF solution at room temperature. The yellow block crystal exhibits a monoclinic crystal system with the space group, I 2/a.

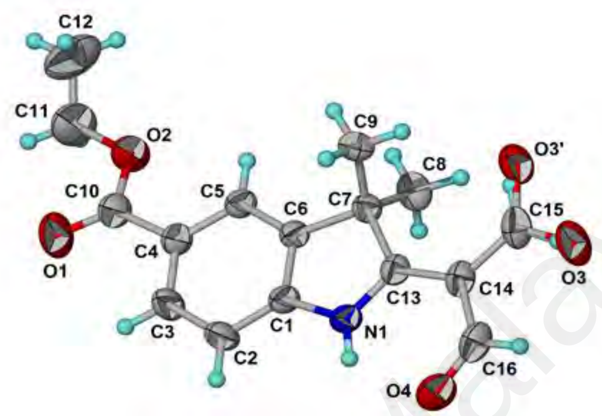

Figure 4.4: The labelled crystal structure of **3** at the 50% probability ellipsoids.

The crystal packing consists of eight molecules per unit cell with the density of 1.313 g cm^{-3} as depicted in **Figure 4.5**. The Vilsmeier-Haack reaction successfully introduced the diformyl group at the methylene position by forming a planar geometrical structure, exception of the two methyl (**C8**, **C9**) and ethyl ester (**C11**, **C12**) groups, which lie slightly above and below out of the plane.

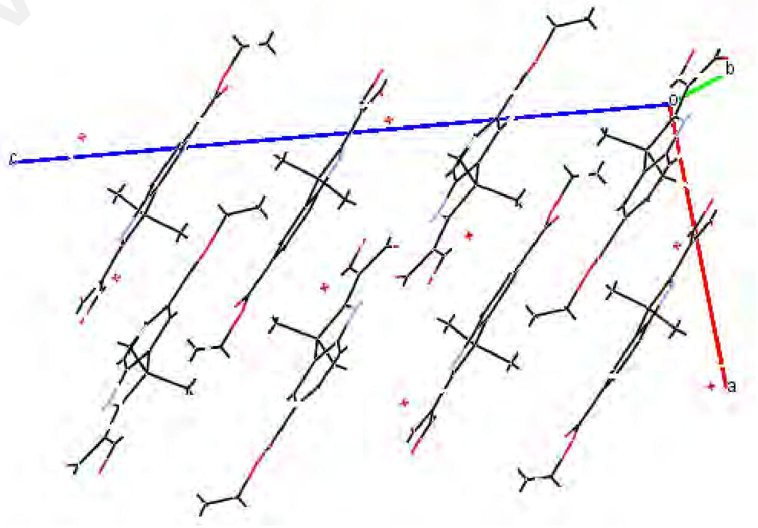

Figure 4.5: Crystal packing of **3** viewed along the *b* axis.

As shown in **Figure 4.6**, one of the formyl group at **C15** is rotated by 180° to form an another ketoamine structure (Khaledi *et al.*, 2011). While the other formyl group at **C16** is involved a strong intramolecular H-bonding interaction with the N-H to stabilize the overall structure. Thus, shortening the bond length between O(4) – C(16), in comparison with that of O(3') – C(15) and O(3) – C(15) bonds. All the selected bond lengths **(**Å), angles (°) and their refinement parameters are given in **Table 4.1** and **Table 4.2**, respectively.

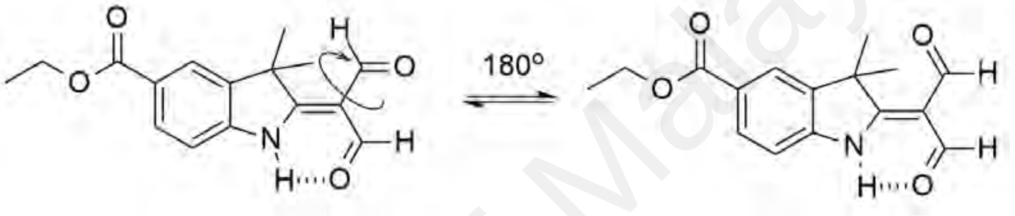

Figure 4.6: The formyl rotation of **3**. The dashed lines represent the H-bonding interaction between N-H-O bond.

Table 4.1: Selected bond lengths (Å) and angles (°) for **3**.

Bond lengths (Å)			
O(1) – C(10)	1.207(3)	C(13) – C(14)	1.410(2)
O(2) – C(10)	1.329(3)	C(14) – C(16)	1.435(3)
O(2) – C(11)	1.462(3)	C(14) – C(15)	1.464(3)
O(3) – C(15)	1.271(4)	N(1) – C(13)	1.341(2)
O(3') – C(15)	1.340(4)	N(1) – C(1)	1.408(2)
O(4) – C(16)	1.233(3)		
Bond angles (°)			
C(10)–O(2)–C(11)	116.47(19)	C(16)–C(14)–C(15)	115.76(18)
C(13)–N(1)–C(1)	112.61(15)	O(3)–C(15)–C(14)	117.7(3)
N(1)–C(13)–C(14)	121.16(17)	O(3') –C(15) –C(14)	128.7(2)
C(14)–C(13)–C(7)	130.14(17)	O(4)–C(16)–C(14)	127.19(19)
C(13)–C(14)–C(15)	124.48(19)		

Symmetry transformations used to generate equivalent atoms: #1 –x+1/2, y, -z.8

Table 4.2: Crystal data and refinement parameters for **3**.

Empirical formula	$C_{16}H_{17}NO_4$
Formula weight	287.31
Temperature (K)	293(2)
Crystal system, Space group	monoclinic, I2/a
Wavelength (Å)	MoKα ($\lambda = 0.71073$)
a (Å)	10.074(2)
b (Å)	12.587(3)
c (Å)	23.042(5)
α (°)	90
β (°)	95.67(3)
γ (°)	90
Volume (Å^3)	2907.4(10)
Z, density (calculated) (g/cm^3)	8, 1.313
F(000)	1216.0
2θ range for data collection (°)	7.108 to 55.976
Index ranges	$-11 \leq h \leq 13$, $-16 \leq k \leq 15$, $-30 \leq l \leq 23$
Reflections collected	12966
Independent reflections	3415 [$R_{int} = 0.0233$, $R_{sigma} = 0.0188$]
Data/ restraints / parameters	3415 / 8 / 205
Goodness-of-fit on F^2	1.052
Final R indexes [I > = 2σ (I)]	$R_1 = 0.0619$, $wR_2 = 0.1685$
Final R indexes (all data)	$R_1 = 0.0760$, $wR_2 = 0.1841$
Largest diff. peak and hole (e Å^{-3})	0.43 and -0.51

4.3 NMR study

Both ^{1}H and ^{13}C NMR spectra of compound **3** were recorded in $CDCl_3$ (see **Appendix A.5** and **A.6** on page 98). The characteristic indole NH showed a broad singlet peak at the most deshielded region at δ = 13.5 ppm due to the H-bonding interaction with the formyl group. The singlet peak at δ = 9.83 ppm is assigned as the two aldehydic protons, which are under the same chemical environment. The three aromatic protons resonanted at the region from δ = 7.19 to 8.06 ppm. Meanwhile, the two singlet signals found at δ = 1.77 ppm and δ = 1.38 ppm correspond to the six methyl proton of indole and three methyl proton of ester groups, respectively. The methylene proton of ester displays as a quartet peak at δ = 4.36 ppm in the spectrum.

In the ^{13}C NMR spectrum, the spectroscopic signals of two formyl carbon atoms appear at δ = 187.70 ppm and δ = 192.65 ppm. The latter is assigned to the ketoamine carbonyl group, owing to its H-bonding interaction with the NH indole, thus increasing the electronegativity of the carbon atom. The carbonyl ester peak appears at δ = 165.97 ppm.

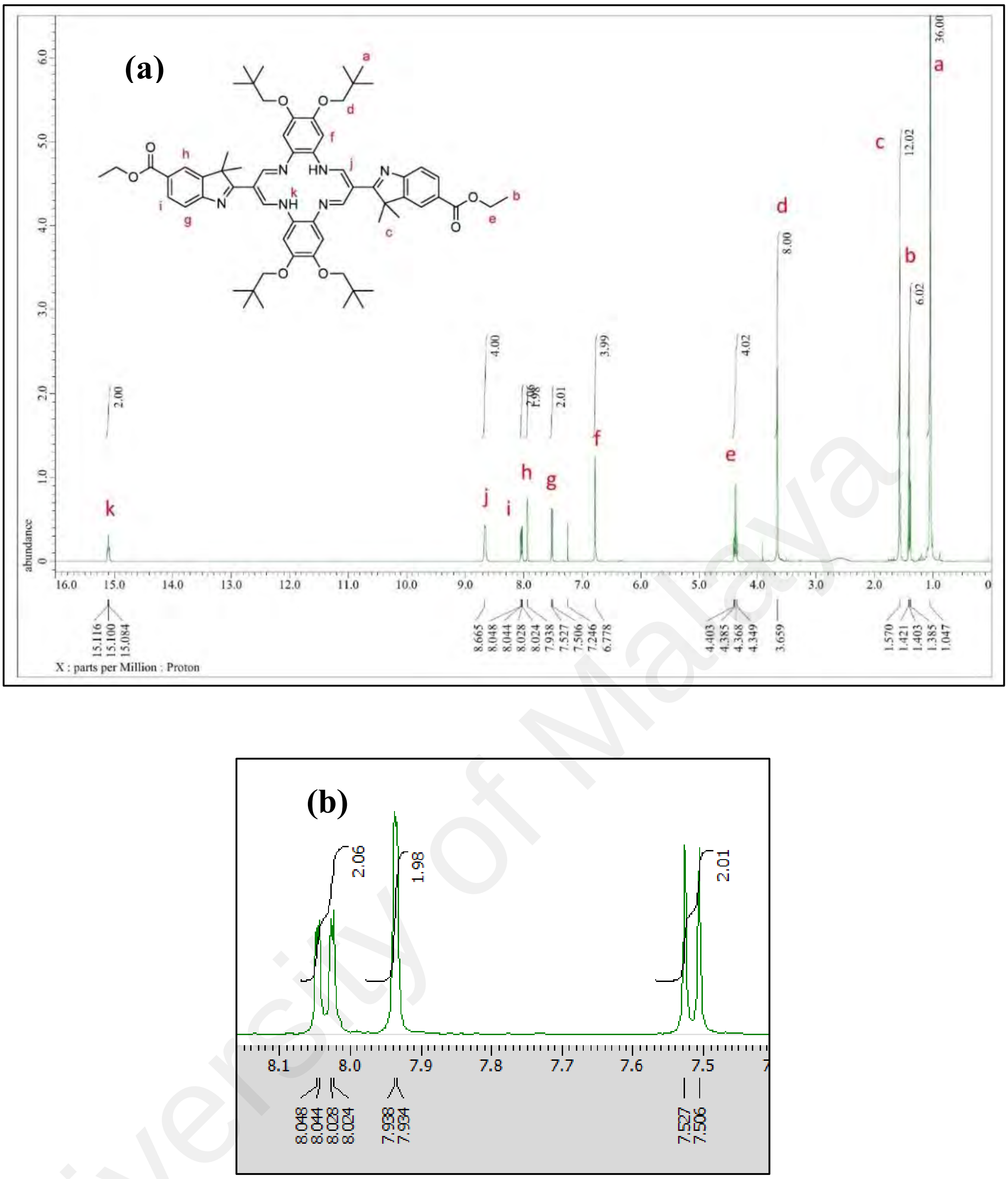

Figure 4.7: a) The labelled ^{1}H NMR spectrum of ligand **7c** and **b)** their aromatic expansion in $CDCl_3$.

As illustrated in **Figure 4.7 a)** and **b)**, the successful formation of the macrocyclic ligand is confirmed by the presence of a triplet signal at δ = 15.08 ppm with $^{3}J_{NH}$ = 6.4 Hz, typically explained due to the NH protons in the ring system which undergo rapid imine – enamine tautomerism. The effect of neopentoxyl group substitution on the ligand gives the four CHN protons, H_j appeared as a singlet at δ = 8.67 ppm, unfortunately the J value could not be measured due to overlapping peaks. However, the appearance of a doublet peak for the CHN proton is clearly seen in the ^{1}H NMR spectrum of ligand **7a** (see **Appendix A.16** on page 103) with $^3J_{\text{trans}}$ = 6.4 Hz, which is similar to the $^3J_{\text{NH}}$ value. These values are in good agreement with the literature data for formation of DBTAA ligand. At the aromatic region, the proton signal of H_g appears as a doublet at δ = 7.51 ppm with $^3J_{1,2}$ = 8.4 Hz. Meanwhile, the H_h and H_i appear at δ = 7.94 ppm and δ = 8.02 ppm, respectively. The four proton of H_f appears as a singlet peak at δ = 6.78 ppm. The peaks found in the region between δ =1.0 - 4.4 ppm are assigned to the five different types of aliphatic protons presence in the structure.

Figure 4.8 is the HSQC spectrum of ligand **7c**, showing the correlation between the carbon and its attached proton. All aromatic benzene carbon peaks are observed at δ = 100.59, 118.06, 122.19, 130.52 ppm corresponding to C_f, C_g, C_h, and C_i, respectively. The C_j peak of H-C=N is observed at 148.78 ppm in the spectrum.

As illustrated in **Figure 4.9**, the HMBC spectrum is used to detect the neighboring carbon with the correlation between carbons and protons that are separated by two and three bonds of ligand **7c**. From the spectrum, the carbonyl ester carbon peak appears at δ = 167.08 ppm. Interestingly, the additional spot observed at δ (8.67 ppm, 148.87 ppm) is represents the correlation between the four H_j proton and another C_j due to the rapid imine-enamine tautomerism of NH protons through the entire 1,3-propanediiminato linkages (Dudek *et al.*, 2011). The observed signal is very close to the actual spectroscopic signal of C_j as indicated in the HSQC spectrum. The details of full HMBC interactions is illustrated in **Figure 4.10** and the result of chemical shift for the quaternary carbons is well establish in **Figure 4.11**.

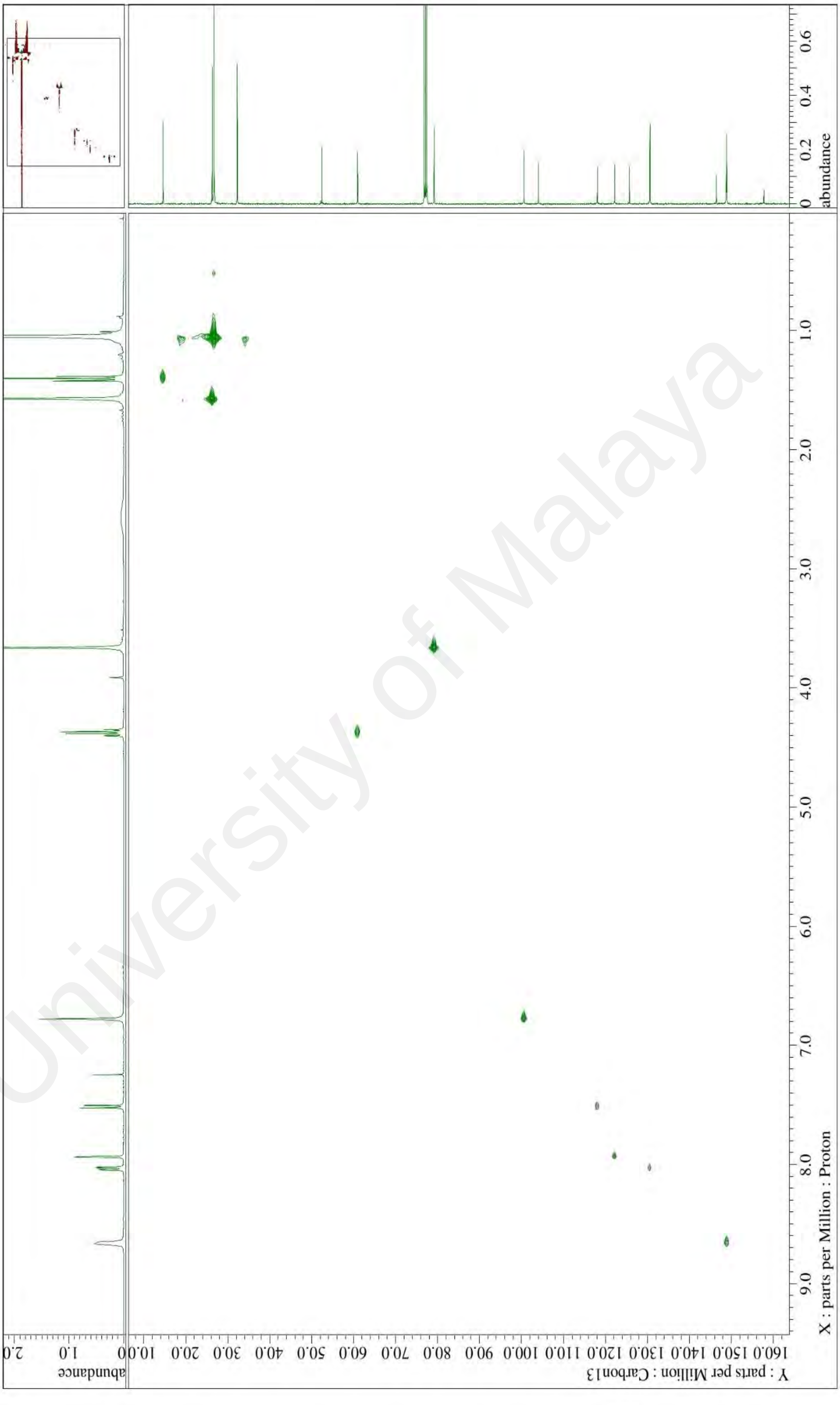

Figure 4.8: The HSQC spectrum of **7c**.

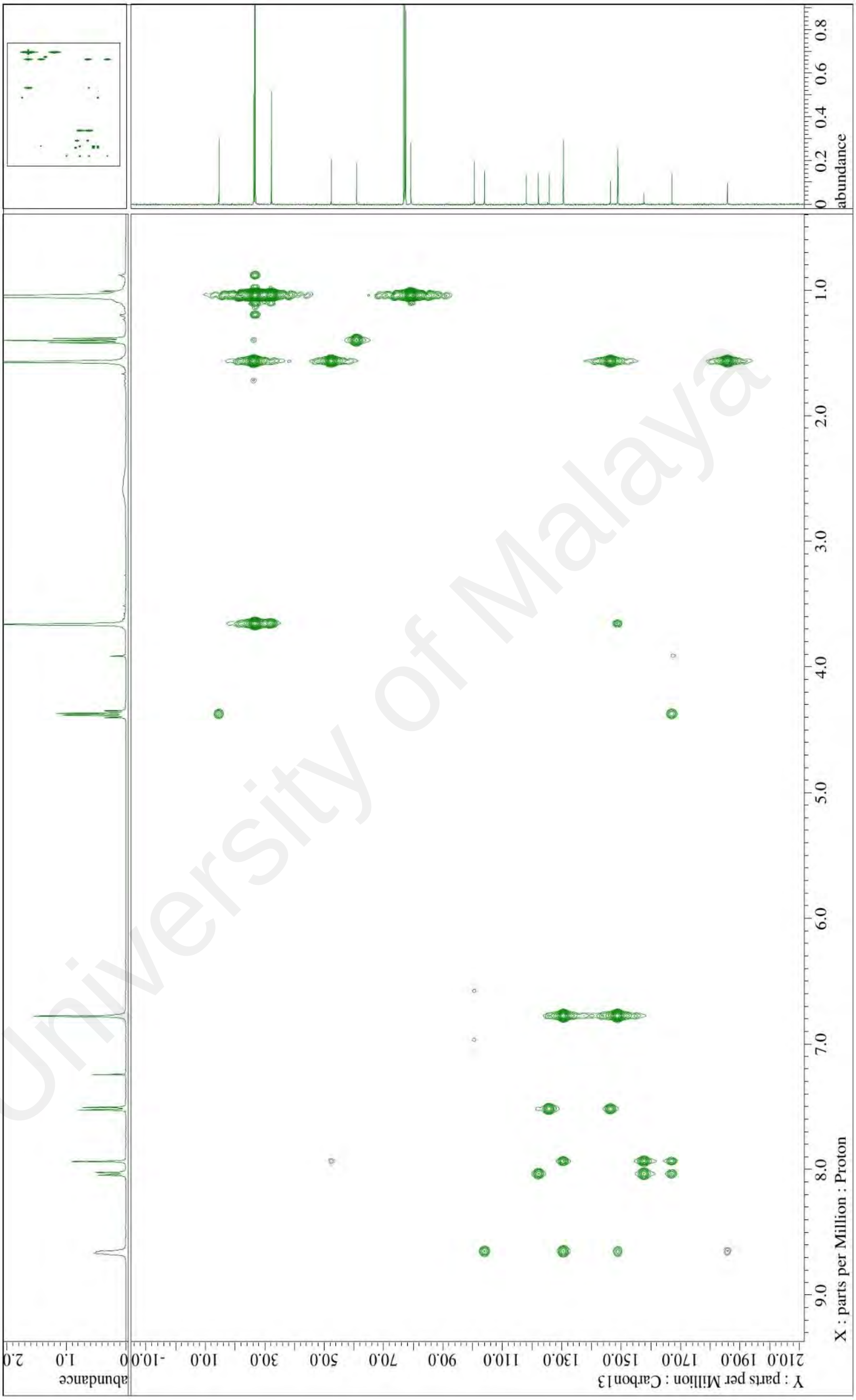

Figure 4.9: The HMBC spectrum of **7c**.

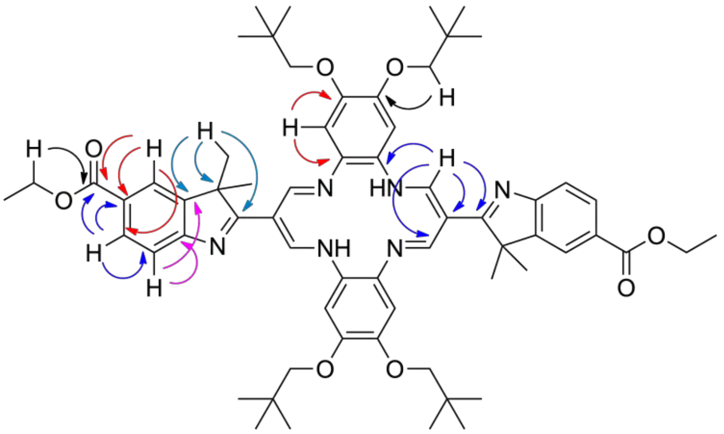

Figure 4.10: The arrows show the correlation between the carbons and protons as indicated in the HMBC spectrum of **7c.**

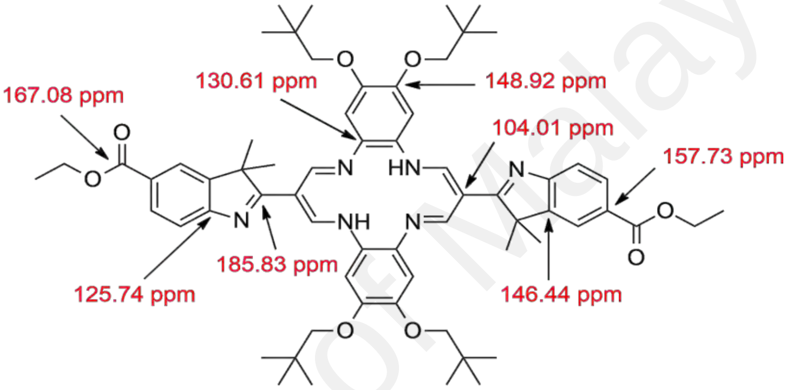

Figure 4.11: The chemical shifts for the quartenary carbons of **7c**.

The complexation of the ligand **7c** with Ni^{2+} slightly changed the ^1H NMR pattern of compound **8c**, where some signals are found shifted towards the upfield region (see **Appendix A.28** on page 109). Moreover, the disappearance of the inner NH signal in ^1H NMR spectrum indicates the chelation of metal ion through deprotonation of NH was successful by forming a diamagnetic square - planar complexes. Moreover, the ^1H NMR spectrum of compound **9c** was recorded in C_5D_5N solvent (see **Appendix A.30** on page 110). The structure was confirmed based on the disappearance of ethyl ester peaks in the ^1H NMR spectrum. However, further characterization using ^{13}C NMR spectrum could not be measured, owing to the low solubility of compound in solution which probably due to strong dimeric H-bonding interaction between COOH groups or strong intermolecular π-π stacking aggregation in the solution.

4.4 IR study

The IR spectrum of **7c** (see **Appendix B.10** on page 121) shows the presence of C=O stretching band of carbonyl ester at 1708 cm^{-1} with low intensity. The peak is found slightly shifted to a lower frequency of 1707 cm^{-1} after metalation reaction (see **Appendix B.13** on page 124). Moreover, the NH stretching band of ligand **7c**, which is previously appeared at 1317 cm^{-1} found disappeared after the chelation reaction with Ni^{2+}. The absorption band of C=C benzene ring of **8c** exhibits a sharp medium band at 1603 cm^{-1}, which is slightly shifted to right upon insertion of Ni^{2+} ion to ligand **7c**. The characteristic C-N stretching band is found in both compounds of ligand **7c** and complex **8c** at 1222 cm^{-1}. The weak frequencies exist in the range 2900 – 2960 cm^{-1} are due to the stretching mode of C-H alkanes for both structures.

The IR spectrum of macrocyclic **9c** (see **Appendix B.14** on page 125) shows a very broad peak with medium intensity at region between 4000 to 2000 cm^{-1} due to the presence of COOH group and their involvement in intermolecular H-bonding (Max & Chapados, 2004). The carboxyl C=O stretching H-dimer peak appears at a lower frequency 1689 cm^{-1} compared to the ester C=O. This is due to the increase the conjugation of double bond structure and weakened of C=O bond. The strong peak displays at 1183 cm^{-1} indicating the C-O stretching of COOH. The absorption bands observed at 2955, 2901 and 2868 cm^{-1} are assigned to the stretching modes of C-H alkanes. In conclusion, all IR assignation bands are in good agreement with the proposed structures of macrocyclic DBTAA ligands and their metal complexes. The presence of COOH bands in the spectrum indicates that the ester hydrolysis of macrocyclic **8c** dye was successful.

4.5 Elemental Analyses

The results of all CHN elemental analyses compounds are tabulated in **Table 4.3**. No significant difference was found between the experimental and theoretical values, indicating high purity of all the synthesized compounds and consistent with the proposed structures.

Table 4.3: The CHN results for all synthesized compounds.

Compound	Molecular Formulae	Percentage of Composition Element, (%) Found (Calculated)		
		C	H	N
1	$C_{12}H_{13}NO_2$	70.65 (70.92)	6.24 (6.45)	6.73 (6.89)
2	$C_{14}H_{17}NO_2$	72.30 (72.70)	7.43 (7.41)	6.43 (6.06)
3	$C_{16}H_{17}NO_4$	66.63 (66.89)	6.04 (5.96)	4.80 (4.88)
5b	$C_{18}H_{28}N_2O_6$	58.46 (58.68)	7.53 (7.66)	7.56 (7.60)
5c	$C_{16}H_{24}N_2O_6$	56.43 (56.46)	7.08 (7.11)	8.18 (8.23)
7a	$C_{44}H_{42}N_6O_4$	73.42 (73.52)	5.87 (5.89)	11.88 (11.69)
7b	$C_{68}H_{90}N_6O_8$	73.04 (72.96)	8.32 (8.10)	7.28 (7.51)
7c	$C_{64}H_{82}N_6O_8$	71.86 (72.29)	7.62 (7.77)	7.77 (7.90)
8a	$Ni\text{-}C_{44}H_{40}N_6O_4$	67.96 (68.14)	5.28 (5.20)	10.63 (10.84)
8b	$Ni\text{-}C_{68}H_{88}N_6O_8$	69.24 (69.44)	7.32 (7.54)	7.07 (7.15)
8c	$Ni\text{-}C_{68}H_{80}N_6O_8$	68.47 (68.83)	7.47 (7.20)	7.53 (7.50)
9c	$Ni\text{-}C_{60}H_{72}N_6O_8$	67.37 (67.73)	7.03 (6.82)	7.66 (7.90)

4.6 UV-Visible Absorption spectra of dyes.

The absorption spectra of the synthesized nickel complexes were recorded in dichloromethane (for **8a**, **8b** and **8c**) and in AcOH (for **8a**, **8b**, **8c** and **9c**), and their UV plots are shown in **Figure 4.12** and **Figure 4.13**, respectively.

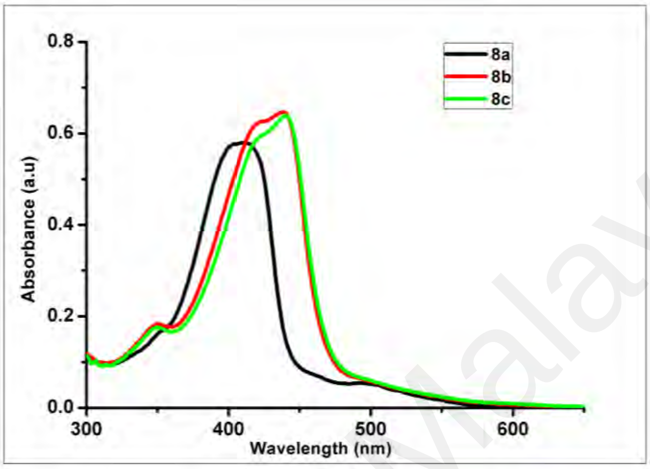

Figure 4.12: Absorption spectra of **8a-8c** in DCM solution.

All electronic parameters are tabulated in **Table 4.4**. The dyes have shown a broad and intense absorption band between 300 - 600 nm in dichloromethane. The weak spectral bands below 400 nm are due to the π-π* transitions in the ligands and charge transfer transition from the metal to the ligands (Sakata *et al.*, 1996). Usually, the broad spectral coverage of more than 400 nm can be attributed to the intramolecular charge-transfer (ICT) transition of the dyes. The strong absorption maxima are observed at 412, 439 and 440 nm for **8a-8c**, with molar absorption coefficients of ε =116000, 129000, 128000 M^{-1} cm^{-1}, respectively. In terms of sensitizer, it is clear that the all ester anchoring group dyes are capable to absorb light for photocurrent generation in DSSCs. The absorption maxima show a bathochromic shifts of ~ 28 nm upon insertion of the electron donor groups of hexoxyl and neopentoxyl. This is due to the extension of the π-conjugation in the structure, which leads to the decrease in energy gap between the HOMO and LUMO levels. The optical energy gaps of **8a-8c** estimated from the absorption onsets are 2.78, 2.62, and 2.62 eV, respectively.

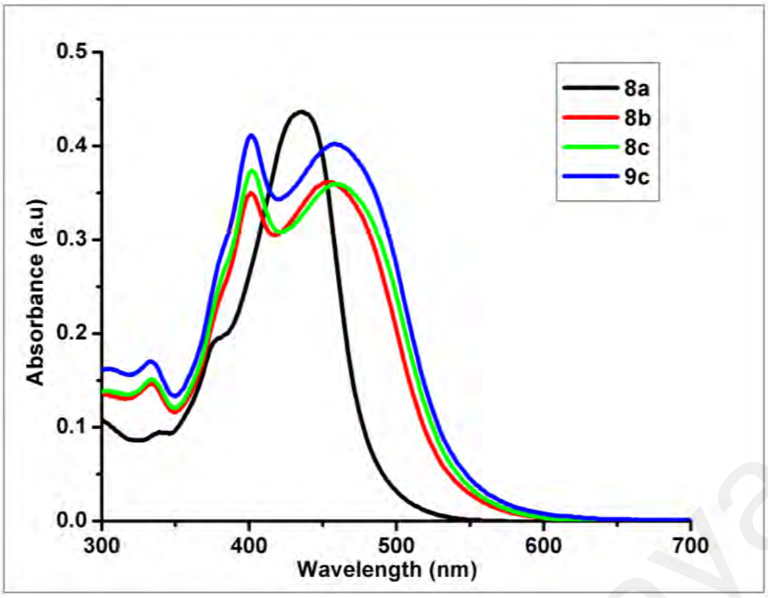

Figure 4.13: Absorption spectra of all dyes in AcOH solution.

Table 4.4: Absorption and electronic parameters of the dyes.

Dye	Solvent	Absorption λ_{max} (nm) / ε ($\times 10^5$ M^{-1} cm^{-1})	λ_{onset} (nm)	E_{gap} (*e*V)
8a	DCM	412 (1.16)	445.7	2.78
	AcOH	380 (0.39), 437 (0.87)	483.7	2.56
8b	DCM	350 (0.37), 439 (1.29)	473.6	2.62
	AcOH	334 (0.30), 401 (0.70),457 (0.70)	532.5	2.33
8c	DCM	350 (0.35), 440 (1.28)	473.5	2.62
	AcOH	334 (0.29), 401 (0.75),457 (0.75)	538.4	2.30
9c	AcOH	334 (0.34), 401 (0.82), 457 (0.82)	540.9	2.29

The λ_{onset} was approximated using a tangent from the first absorption band in the spectra with the correlation factor of $R^2 > 0.99$ and the expression for $\boldsymbol{E_{gap}} = \frac{\mathbf{1240}}{\boldsymbol{\lambda_{onset}}} \boldsymbol{e}\mathbf{V}$.

Figure 4.12 shows the UV-Vis absorption spectra measured in AcOH. Substituting dichloromethane for the more polar solvent of acetic acid resulted in positive salvatochromism for all dyes (Buncel & Rajagopal, 1990). The dye **8a** shows a broad spectrum between 350 - 550 nm, whereas the absorption spectra for the alkoxy-substituted dyes **8b**, **8c** and **9c** extend to 600 nm. The decrease in the intensity measured in AcOH is due to the intermolecular interactions between the solvent and dyes (Reichardt, 1994). The COOH-substituted dye **9c** exhibits a very similar absorption spectrum to those of **8b** and **8c** where the two main absorption bands are observed at 401 nm and 457 nm with the molar absorption coefficient in the range of ($0.70 – 0.82 \times 10^5$ M^{-1} cm^{-1}). The strong absorption bands below at $\lambda = 334$ nm can be attributed to π-π^* transitions within the macrocyclic dyes. Although all dyes have high absorption coefficient in both solvents, no fluorescence properties were observed in the solution. The optical gap of **9c** is determined in acetic acid solution due to insoluble in dichloromethane solvent and the value is 2.29 eV. Based on the data collected, all dyes should be suitable sensitizers for DSSCs applications.

4.7 Electrochemical Properties

Cyclic voltammetry experiment is conducted to determine the HOMO energy level of dyes in order to investigate the possibility of electron injection to the CB TiO_2. Cyclic voltammetry (CV) of dyes **8a** - **8c** were measured in dry DCM with $TBAPF_6$ (0.1M) as the supporting electrolyte, using a Pt wire as the counter electrode, an Ag/AgCl as the reference electrode, and measured at a scan rate of 25 mV s^{-1} at room temperature. The potential was calibrated using a ferrocenium / ferrocene, (Fc^+/Fc) couple where the $E_{Fc/Fc+}$ was observed at 0.37 eV. The HOMO and LUMO of energy levels were calculated from the following equations (Liu *et al.*, 2014).

$$E_{HOMO} = -[E_{oxi}^{onset} - E_{Fc/Fc+} + 4.8]\ e\text{V}$$

$$E_{LUMO} = (E_{HOMO} + E_{gap})\ e\text{V}$$

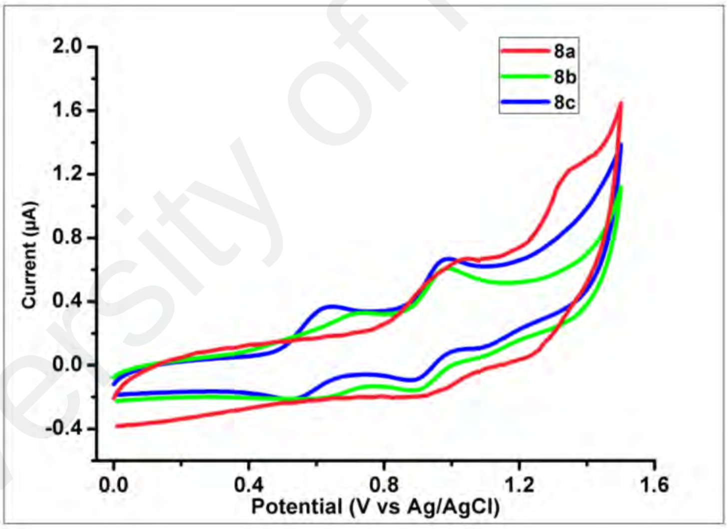

Figure 4.14: Cyclic voltammetry of **8a** - **8c** dyes solution using a glassy carbon as working electrode.

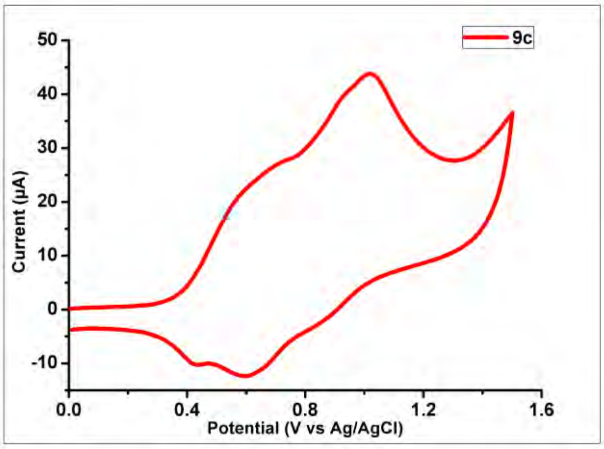

Figure 4.15: Cyclic voltammetry of **9c** using a dye sensitized photoanode as working electrode.

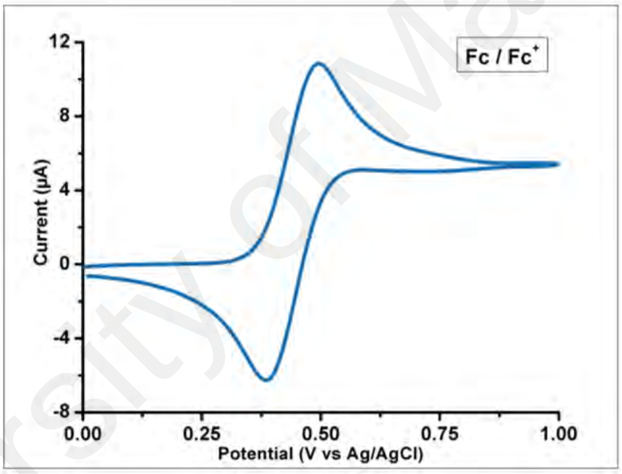

Figure 4.16: Cyclic voltammetry of 1.0 mM (Fc/Fc$^+$) containing 0.1 M TBAPF$_6$ in DCM solution.

Table 4.5: Electrochemical properties of dyes.

Dye	E_{oxi}^{onset} (eV)	E_{HOMO} (eV)	E_{LUMO} (eV)
8a	0.79	- 5.22	- 2.44
8b	0.41	- 4.84	- 2.22
8c	0.49	- 4.92	- 2.30
9c	0.38	- 4.81	- 2.52

All electrochemical data are listed in **Table 4.5**. All dyes exhibited two quasi - reversible oxidation and reduction wave in the voltammograms as shown in **Figure 4.14**. The HOMO energy levels estimated from the first onset of oxidation waves are -5.22, -4.84 and – 4.92 eV for **8a - 8c**, respectively which are more negative than the redox energy level of the electrolyte (-4.8 eV) (Nagarajan *et al.*, 2017). Therefore, it is thermodynamically favorable for the oxidized dyes to accept electrons from the redox electrolyte, I^-/I_3^- ions for the dye regeneration process. The HOMO energy levels of dyes **8b** and **8c** are at more positive potentials compared to that of **8a**, which is due to their electron rich structures. The E_{gap} values from the absorption spectra in dichloromethane were used to estimate the LUMO energy levels of the **8a** - **8c**, which are -2.44, -2.22 and -2.30 eV, respectively. This indicates that all dyes are capable to inject electrons from the excited state of the dyes to the conduction band of the TiO_2 (-4.0 eV).

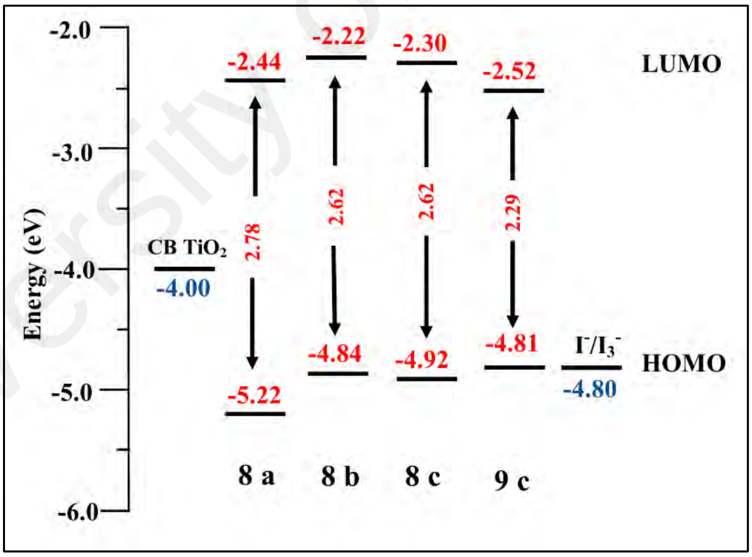

Figure 4.17: Schematic energy levels of the dyes corresponding to the DSSCs components.

The electrochemical properties of **9c** could not be performed in DCM solution due to the poor solubility of the compound, thus a dye – sensitized photoanode was used as the working electrode. As shown in **Figure 4.15**, the first onset oxidation potential for **9c** was observed at 0.38 eV which corresponds to a HOMO value of -4.81 eV. Theoretically, the small energy gap between the HOMO of the dye and the redox electrolyte I^-/I_3^-, could decrease the efficiency of DSSC due to an insufficient electron transfer for regeneration process of the oxidized dye, thus lower efficiency of DSSC is expected (Ning *et al.*, 2008). The LUMO energy level is -2.52 eV, and favours the electron injection to the conduction band of TiO_2. The calculated E_{gap} value from the absorption spectra in AcOH was used in the estimation. All parameters obtained from the absorption spectra and cyclic voltammetry measurements are illustrated in **Figure 4.17**. The CV of the dyes (**8a** - **8c**) was performed at a platinum electrode and in solution, in contrast to the sensitization of the dyes on the TiO_2 surface (**9c**) in the DSSC. Nevertheless, both the voltammetric measurements are relevant for the estimation of HOMO and LUMO energy levels.

4.8 DFT calculations

To elucidate the relationship between the geometrical structure and the electronic distribution of the dyes at different energy levels, DFT calculation were performed in the gas phase and the frontier molecular orbital profiles are shown in **Figure 4.18**. All calculations were fully optimized in the ground state with hybrid DFT at the B3LYP level of theory using Gaussian 09 program package (Becke, 1988). The 6-31G(d) basis set was performed for the C, H, N and O atoms (Cai-Rong *et al.*, 2009), while the LANL2DZ basis set (Yao *et al.*, 2008) which includes an effective core potential (ECP) was performed on the Ni atom. Frequency computation was also performed for all dyes to confirm that the optimized geometry corresponds to a stationary point. In terms of the optimized geometrical structure as depicted in **Figure 4.19**, dyes **8a – 8c** gave a saddle shaped (non-planar) geometrical structure with an estimated dihedral angle between the two indoleninyl side groups of 159.4^{o}, 146.7^{o} and 149.5^{o} for **8a** - **8c**, respectively. However, the conformations of optimized dyes obtained from the theoretical calculation are slightly different from the experimental solid state structure of Ni-DBTAA **(Figure 2.9)**, which is planar. The planar geometry of optimized dye **9c** containing COOH anchoring group is expected to have a good electron conjugation in the molecule.

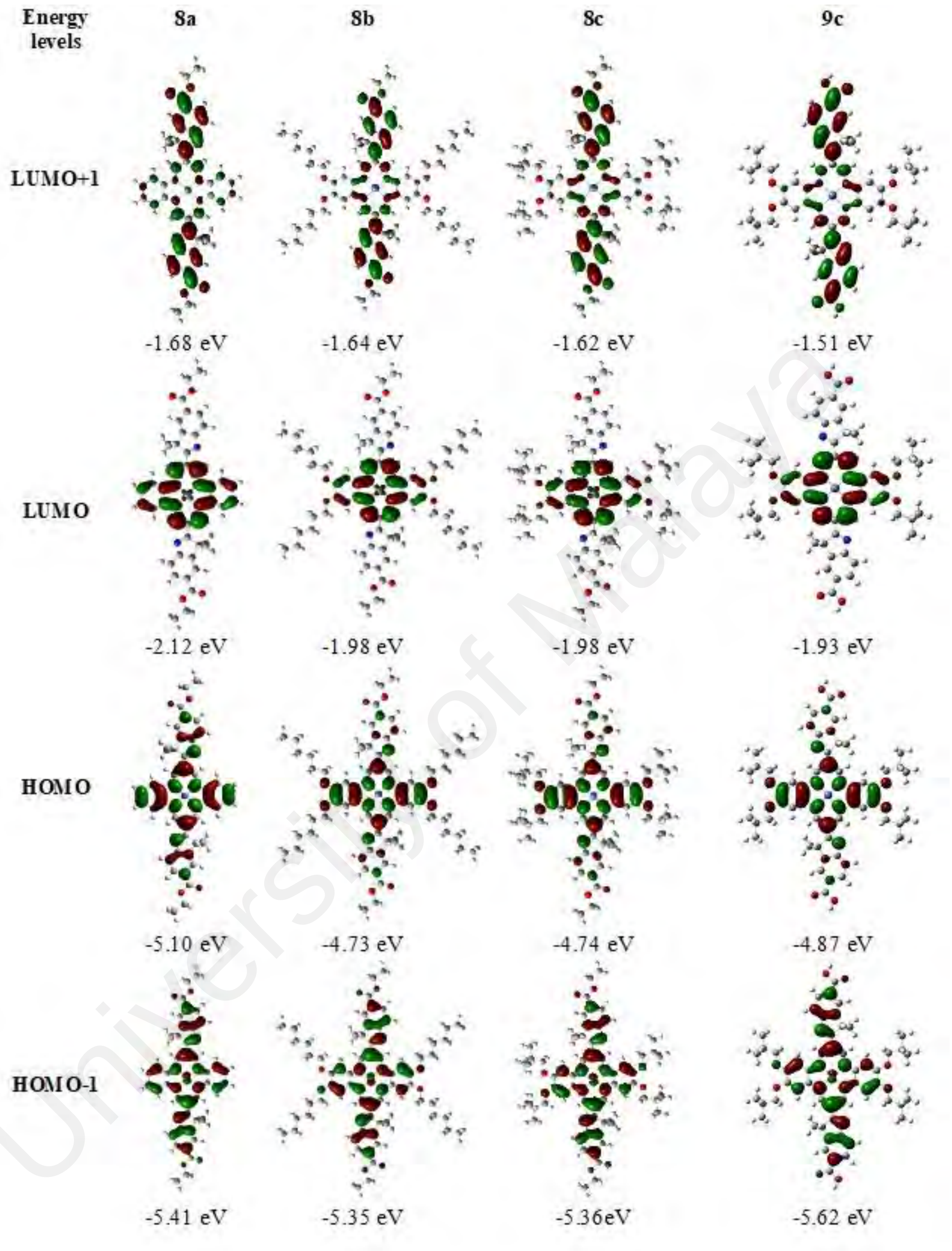

Figure 4.18: The frontier molecular orbitals of all dyes calculated by DFT at B3LYP/GenECP with 6-31G(d) basis set used for non-metals and LANL2DZ for Ni atom.

Dye	Top View	Side View
8a		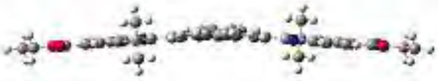
8b	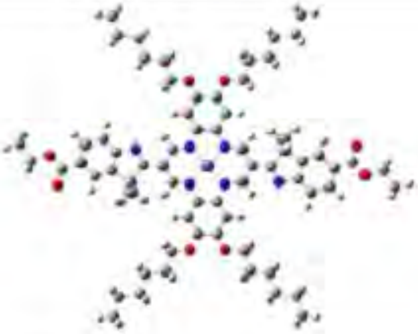	
8c	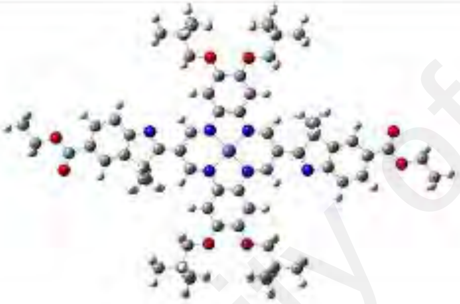	
9c	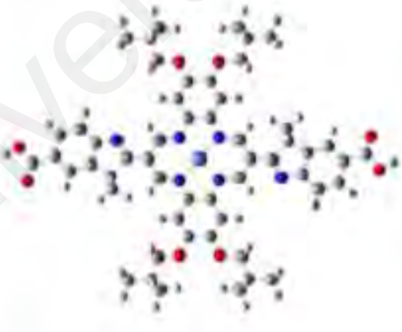	

Atom representation: Ni Nickel, O oxygen, N nitrogen, C carbon, H and hydrogen atoms respectively.

Figure 4.19: The geometry optimized structures of all dyes.

Table 4.6: Calculated HOMO and LUMO energy levels using DFT.

Dye	E_{HOMO} (eV)	E_{LUMO} (eV)	E_{gap} (eV)
8a	-5.10	-2.12	2.98
8b	-4.73	-1.98	2.75
8c	-4.74	-1.98	2.76
9c	-4.87	-1.93	2.94

The DFT results suggest that all dyes have similar electronic distribution in the HOMOs and LUMOs, where the electron densities are mainly delocalized throughout the DBTAA core as well as the indoleninyl units. Compared to **8a,** the alkoxy groups substitution in the dyes of **8b**, **8c**, and **9c** slightly changed the electronic distributions with a decrease in the HOMO and LUMO energy levels. The calculated HOMO - LUMO energy gaps for dyes **8a** - **8c** are between 2.75 – 2.98 *e*V, which is slightly higher than the experimental optical gap (E_{gap}) values obtained from the UV spectra of dichloromethane. At the LUMO+1, although the electron density of **8a** – **8c** are well distributed over the indoleninyl units, they are still incapable of reaching the anchoring group of the ethyl ester. On the other hands at the LUMO+1 of **9c**, the partial shift of electron density towards the COOH anchoring group is sufficient to promote the electrons to the conduction band of TiO_2 upon photoexcitation.

4.9 Photovoltaic Performances

The newly sensitized dyes was soaked in 0.2 mM solution and evaluated under stimulated AM 1.5G sunlight (100 mW cm^{-2}) using I^-/I_3^- as the redox electrolyte. The effective area was 0.196 cm^2. In these experiments, the two different compact layers of semiconductor TiO_2 with different particle sizes (P90 and P25) were deposited onto a FTO substrate in order to produce more solid state structural defects which allow the liquid electrolyte diffuse into the mesoporous TiO_2 (Mingsukang *et al.*, 2017). In fact, the combination of different compact layer is used to prevent or to reduce the amount of electron losses in between interlayer of the electrolyte and the FTO conducting glass. Therefore, it will give a better catalytic activity because of the less possibility for electrons recombination to occur in the cell.

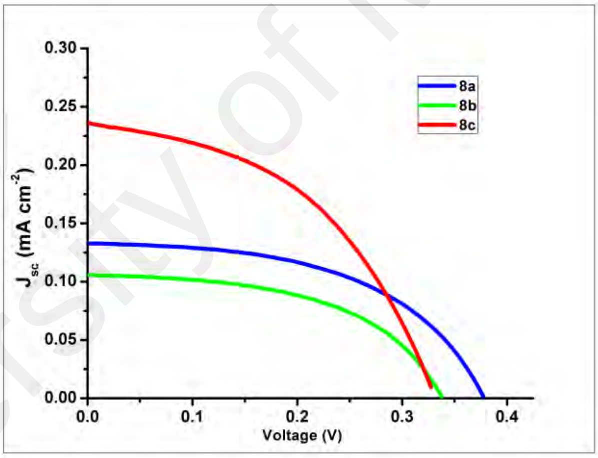

Figure 4.20: The *J-V* curves of **8a** - **8c**.

The photocurrent-voltage (*J-V*) relationships of the cell are shown in **Figure 4.20** and **Figure 4.21**. The detailed of their photovoltaic properties are summarized in **Table 4.7**. The lowest efficiency was demonstrated by dye **8b**, which gave the overall η = 0.019%, with J_{sc} = 0.10 mA cm^{-3}, V_{oc} = 0.33 V and FF = 0.562. Meanwhile, the **8a** gave better cell performance than **8b** with an increase in the J_{sc} and V_{oc}, corresponding to an efficiency of 0.026%. This result could be probably due to the lower amount of dye on the TiO_2 surface as the planar geometrical size of the dye increases.

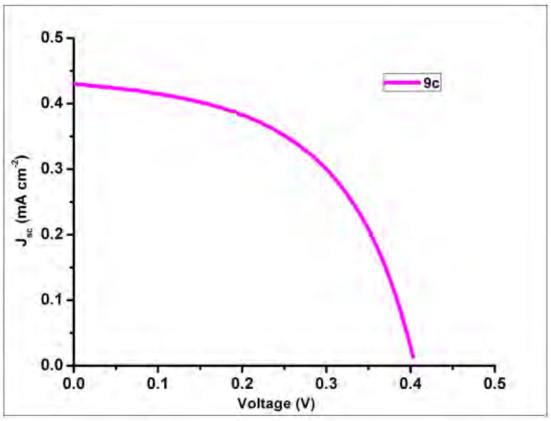

Figure 4.21: The *J-V* curve of **9c**.

Table 4.7: Photovoltaic parameters of all dyes.

Dye	J_{sc} (mA cm^{-2})	V_{oc} (V)	Fill factor (FF)	PCE, η (%)
8a	0.13	0.38	0.524	0.026
8b	0.10	0.33	0.562	0.019
8c	0.24	0.33	0.456	0.036
9c	0.43	0.41	0.528	0.093

The cell **8c** gave the best cell performance among the ester anchoring group. Compared to **8a** dye, the branched alkyl chains improved the J_{sc} value from 0.13 to 0.24 mA cm^{-2} but decreased the V_{oc} and *FF* parameters to 0.33V and 0.456, respectively. The highest value of *J*sc of **8c** dye compared to **8a** and **8b** was due to twist conformation of dye structure in the presence of branched alkyl chain group which help to reduce the face-to-face π-aggregation of the planar dye upon sensitization on the TiO_2 photoanode. When COOH was the anchoring group, the **9c** dye achieved an overall efficiency of 0.093% with J_{sc} = 0.43 mA cm^{-2}, V_{oc} = 0.41 V and *FF* = 0.528, which indicated that the dye had sufficient anchoring on the TiO_2 surface for electron transfer process, compared to the ester dyes.

Considering the types of anchoring groups used, the poor performance of dyes (**8a-8c**) is due to the weak binding attachment of ethyl ester on the TiO_2 surface compared to COOH anchoring group of dye **9c**. The coordination bond between the C=O and the TiO_2 surface makes the ester anchoring groups are ineffective in transferring the electron from the dye molecules to the CB of TiO_2. Unlike dye **9c**, the COOH is deprotonated upon adsorbed onto the TiO_2 semiconductor, hence more efficient for electron injection compared to the ester anchoring group.

Furthermore, the presence of dual anchoring group of ester or COOH on the both sides of indoleninyl part, we expected all dyes were attached on the TiO_2 surface in planar orientation mode rather than parallel mode, resulted in low dye loading amount on the TiO_2 surface. The poor performance of all dyes were also supported by preliminary DFT computational evaluation where all dyes required high photoexcitation energy to excite the electron from the HOMO to the LUMO energy level, consequently reducing the amount of electrons population at CB of TiO_2.

Finally, the branched alkyl chain substitution on **9c** was insufficient to improve the solubility of dye in the solution, thus it led to the formation of π-π stacking aggregation between the dyes on the TiO_2 surface which affected the rate of charge transfer during the photoexcitation and regeneration processes. The role of branched alkyl chain helped to prevent the recombination of electron between the iodide and the oxidized dye, it explained the higher η exhibited by **8c** and **9c** compared to **8a** and **8b** dyes.

4.10 Comparison of IPCE, EIS, and electron lifetime between 8c & 9c.

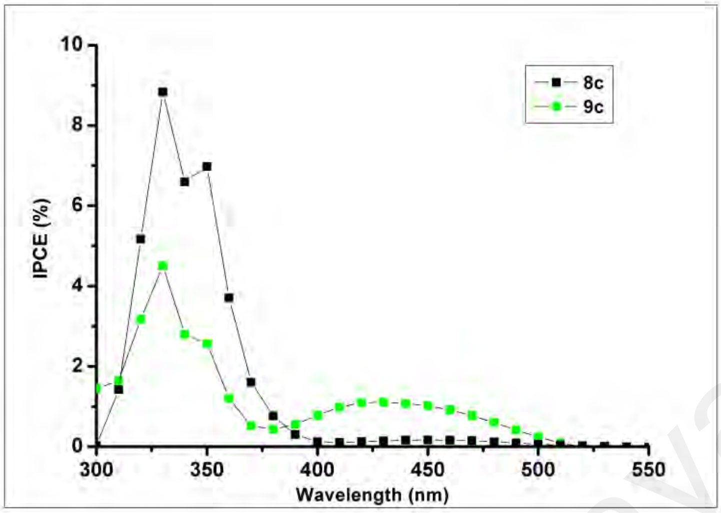

Figure 4.22: The IPCE spectrum of **8c** and **9c**.

To investigate the different of J_{sc} values between the **8c** and **9c** dyes, the incident photon-to-current conversion efficiencies (IPCEs) curves were plotted as shown in **Figure 4.22**. Both dyes display extremely weak photocurrent responses under simulated light. The maximum IPCE intensity occurs at the same wavelength at 330 nm, with intensities of 8.84 % and 4.50 % for the **8c** and **9c** dyes, respectively. The **9c** dye shows a slightly broad and higher intensity of IPCE spectrum in between 375-525 nm, which is consistent to the higher J_{sc} value than **8c** dye. This indicates that the **9c** dye is more efficient in converting photons into electrical energy than **8c** dye upon received the sunlight energy. The higher J_{sc} value of **9c** dye observed in the *J-V* curve could be due to the higher dye absorbing amount attached on the TiO_2 compared to **8c** dye, which increased the amount of electron injection to CB TiO_2. The J_{sc} values obtained in the photovoltaic performances between ethyl ester and COOH types anchoring groups can be further explained by electron lifetime analysis.

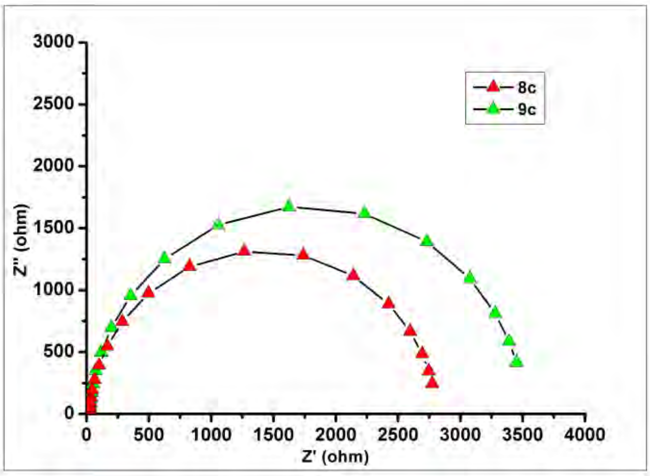

Figure 4.23: The EIS Nyquist plots of device **8c** and **9c**.

The Electrochemical Impedance Spectroscopy (EIS) analysis was performed at open circuit voltage of 0.3 *V* in order to analyse the interfacial properties between photoanodes **8c**, **9c** and electrolyte of the devices as shown in **Figure 4.23**. The R_s and R_1 are represents the series resistance, and interfacial resistance between the counter electrode (Pt) and the electrolyte, respectively. The R_1 values for both devices are extremely small and could not be seen in the spectrum. However, the larger semicircles in the Nyquist plot is represented by R_2, attributed to the charge transfer resistance across the TiO_2/dye/electrolyte interfaces which is mainly related to the dye performance. The larger R_2 indicates a larger charge transfer resistance, smaller dark current (charge recombination) and higher V_{oc}. The estimated R_2 values of the **8c** and **9c** dyes are 2786 Ω and 3490 Ω, respectively. This indicates that the dye **9c** has a greater interfacial resistance between photoanodes and electrolyte than dye **8c**, and the results are consistent with the V_{oc} recorded in *J*-*V* curve.

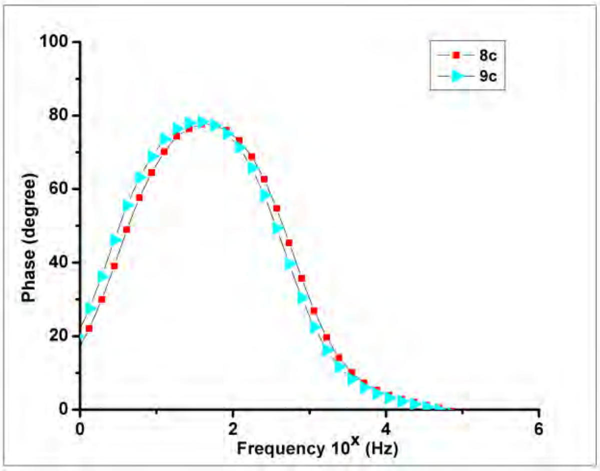

Figure 4.24: The Bode phase plots of **8c** and **9c**.

Table 4.8: Parameters obtained from the Nyquist plots derived from curve fitting.

Dye	R_S (Ω)	R_1 (Ω)	R_2 (Ω)	Electron lifetime (ms)
8c	18	3	2786	44
9c	22	3	3490	62

The maximum frequency of the semicircle in the Nyquist plot in **Figure 4.23** can be further investigated by the electron lifetime and Bode phase plot is shown in **Figure 4.24**. The value is calculated from the plot by $\tau_e = (2\pi f)^{-1}$, where f is the mid - frequency peak which corresponds to the charge transfer process of the injected electrons in the cell. The dye **9c** (62 ms) showed longer electron lifetime compared to dye **8c** (44 ms), indicated that the recombination resistance of fabricated dye **9c** is higher than dye **8c**. The result explained that the electron lifetime of **9c** can survive for a longer time than dye **8c** during electron transport for the external work done in the cell. The calculated values are agree well with the J_{sc} and PCE parameters obtained from the J-V curve measurement. All the EIS data are tabulated in **Table 4.8**.

CHAPTER 5: CONCLUSION

In summary, a new class of sensitizers based on the macrocyclic DBTAA structure with the ethyl ester or COOH anchoring groups were prepared and evaluated for their DSSCs application. The UV-Vis results revealed that all dyes have relatively high absorption coefficients (ε), which is necessary for sensitizers in DSSCs. Although the electrochemical results show that upon excitation, all dyes are able to inject electrons to the conduction band of TiO_2, the small energy gap between HOMO of the dyes and I^-/I_3^- electrolyte significant could affect the DSSCs performance because of insufficient electron transfer for dye regeneration. The poor solubility of the dyes in the solution and their aggregation on the TiO_2 photoanode is perhaps a preliminary reason for low efficiency obtained. The DFT calculation suggests a lack of electron density on the anchoring group which could be a contributing factor to the poor DSSCs performance due to insufficient electron flow from the donor to the acceptor moiety. The carboxylic acid dye **9c** dye gave a better photocatalytic activity than the ethyl ester dyes **8a - 8c**, resulting in the highest efficiency of 0.093% was achieved**.** The neopentoxyl and hexoxyl substitution improved the J_{sc} and *FF* values, respectively. The differences in the terms of the J_{sc} and V_{oc} values between dyes **8c** and **9c** can be correlated to the IPCE, EIS and electron lifetime results.

For future works, further structural modification of dye are required *via* replacement of the anchoring group or extending the π-conjugation system on the DBTAA moiety in order to alter the HOMO energy level and increase the rate of electron injection to the conduction band of TiO_2. The use of different types of electrolyte might help with fine tuning of the energy levels to maximize the electron transfer for regeneration process of oxidized dye.

REFERENCES

Ambre, R. B., Mane, S. B., Chang, G.-F., & Hung, C.-H. (2015). Effects of number and position of *meta* and *para* carboxyphenyl groups of zinc porphyrins in dye-sensitized solar cells: Structure–performance relationship. *ACS Applied Materials & Interfaces, 7*(3), 1879-1891.

Azuma, N., Tani, H., Ozawa, T., Niida, H., Tajima, K., & Sakata, K. (1995). A crystal modification of dibenzo[b,i][1,4,8,11]tetraaza[14]annulene: X-ray molecular structure and proton tautomerism of the highly [π]-conjugated form. *Journal of the Chemical Society, Perkin Transactions 2, 0*(2), 343-348.

Bai, Y., Cao, Y., Zhang, J., Wang, M., Li, R., Wang, P., . . . Grätzel, M. (2008). High-performance dye-sensitized solar cells based on solvent-free electrolytes produced from eutectic melts. *Nature Materials, 7*(8), 626-630.

Baradarani, M. M., Afghan, A., Zebarjadi, F., Hasanzadeh, K., & Joule, J. A. (2006). The synthesis of 3,3-dimethyl-2-(1-aryl-1h-pyrazol-4-yl)-3H-indoles. *Journal of Heterocyclic Chemistry, 43*(6), 1591-1595.

Becke, A. D. (1988). Density-functional exchange-energy approximation with correct asymptotic behavior. *Physical Review A, 38*(6), 3098-3100.

Bella, F., Sacco, A., Pugliese, D., Laurenti, M., & Bianco, S. (2014). Additives and salts for dye-sensitized solar cells electrolytes: what is the best choice? *Journal of Power Sources, 264*(Supplement C), 333-343.

Bonadies, J. A., Maroney, M. J., & Pecoraro, V. L. (1989). Structurally diverse manganese(III) Schiff base complexes: solution speciation via paramagnetic proton NMR spectroscopy and electrochemistry. *Inorganic Chemistry, 28*(11), 2044-2051.

Buncel, E., & Rajagopal, S. (1990). Solvatochromism and solvent polarity scales. *Accounts of Chemical Research, 23*(7), 226-231.

Cai-Rong, Z., Zi-Jiang, L., Yu-Hong, C., Hong-Shan, C., You-Zhi, W., & Li-Hua, Y. (2009). DFT and TDDFT study on organic dye sensitizers D5, DST and DSS for solar cells. *Journal of Molecular Structure: THEOCHEM, 899*(1), 86-93.

Campbell, W. M., Burrell, A. K., Officer, D. L., & Jolley, K. W. (2004). Porphyrins as light harvesters in the dye-sensitised TiO_2 solar cell. *Coordination Chemistry Reviews, 248*(13), 1363-1379.

Cannadine, J. C., Errington, W., Moore, P., Wallbridge, M. G. H., Nield, E., & Fenn, D. (1995). Group 13 tetraazamacrocyclic complexes. The synthesis and characterisation of the monomethyl- and dimethyl-aluminium(III) and gallium(III) complexes of the two tetraazamacrocyclic ligands omtaa$_2$− (H$_2$omtaa=2,3,6,8,11,12,15,17-octamethyl-5,14-dihydro-5,9,14,18-tetraaza-dibenzo[a,h]-cyclotetradecene), and tmtaa$_2$− (H$_2$tmtaa = 6,8,15,17-tetramethyl-5,14-dihydro-5,9,14,18-tetraaza-dibenzo[a,h]cyclotetradecene), and the crystal structure of [MeGa(omtaa)]. *Journal of Organometallic Chemistry, 486*(1), 237-242.

Chapin, D. M., Fuller, C. S., & Pearson, G. L. (1954). A new silicon p-n junction photocell for converting solar radiation into electrical power. *Journal of Applied Physics, 25*(5), 676-677.

Chave, P., & Honeybourne, C. L. (1969). A template synthesis of metal complexes of macrocyclic ligands. *Journal of the Chemical Society D: Chemical Communications, 0*(6), 279-279.

Chen, J., Ko, S., Liu, L., Sheng, Y., Han, H., & Li, X. (2015). The effect of different alkyl chains on the photovoltaic performance of D-π-A porphyrin-sensitized solar cells. *New Journal of Chemistry, 39*(5), 3736-3746.

Chen, R., Yang, X., Tian, H., Wang, X., Hagfeldt, A., & Sun, L. (2007). Effect of tetrahydroquinoline dyes structure on the performance of organic dye-sensitized solar cells. *Chemistry of Materials, 19*(16), 4007-4015.

Choi, H., Nahm, C., Kim, J., Moon, J., Nam, S., Jung, D.-R., & Park, B. (2012). The effect of TiCl$_4$-treated TiO$_2$ compact layer on the performance of dye-sensitized solar cell. *Current Applied Physics, 12*(3), 737-741.

Chulkin, P., Vybornyi, O., Lapkowski, M., Skabara, P. J., & Data, P. (2018). Impedance spectroscopy of OLEDs as a tool for estimating mobility and the concentration of charge carriers in transport layers. *Journal of Materials Chemistry C, 6*(5), 1008-1014

Cotton, F. A., & Czuchajowska, J. (1990). Recent developments in the chemistry of mono- and dinuclear complexes of the macrocyclic dianion, 5,7,12,14-tetramethyldibenzo[b,i][1,4,8,11] tetraazac. *Polyhedron, 9*(21), 2553-2566.

Cutler, A. R., Alleyne, C. S., & Dolphin, D. (1985). Facile template synthesis of nickel(II) complexes of dibenzotetraaza[14]annulenes. *Inorganic Chemistry, 24*(14), 2276-2281.

Dresselhaus, M. S., & Thomas, I. L. (2001). Alternative energy technologies. *Nature, 414*(6861), 332-337.

Dudek, Ł., Grolik, J., Kaźmierska, A., Szneler, E., Eilmes, A., Stadnicka, K., & Eilmes, J. (2011). F− and OH− induced monodeprotonation of a lacunar cationic dibenzotetraaza[14]annulene: experimental evidence of tautomerism in a monoanionic macrocycle. *Tetrahedron Letters, 52*(28), 3597-3601.

Fang, X., Ma, T., Guan, G., Akiyama, M., Kida, T., & Abe, E. (2004). Effect of the thickness of the Pt film coated on a counter electrode on the performance of a dye-sensitized solar cell. *Journal of Electroanalytical Chemistry, 570*(2), 257-263.

Faraj, F. L., Khaledi, H., Morimoto, Y., Itoh, S., Olmstead, M. M., & Ali, H. M. (2014). A tetradentate *β*-diiminato ligand containing phenolate substituents: Flexivalent coordination to Mn^{III}, Co^{III}, Ni^{II}, and Cu^{II}. *European Journal of Inorganic Chemistry, 2014*(33), 5752-5759.

Feng, H., Qiu, N., Wang, X., Wang, Y., Kan, B., Wan, X., . . . Chen, Y. (2017). An A-D-A type small-molecule electron acceptor with end-extended conjugation for high performance organic solar cells. *Chemistry of Materials, 29*(18), 7908-7917.

Feng, Q., Zhou, G., & Wang, Z.-S. (2013). Varied alkyl chain functionalized organic dyes for efficient dye-sensitized solar cells: Influence of alkyl substituent type on photovoltaic properties. *Journal of Power Sources, 239*(Supplement C), 16-23.

Funaki, T., Otsuka, H., Onozawa-Komatsuzaki, N., Kasuga, K., Sayama, K., & Sugihara, H. (2014). Systematic evaluation of HOMO energy levels for efficient dye regeneration in dye-sensitized solar cells. *Journal of Materials Chemistry A, 2*(38), 15945-15951.

Gang, X., Liqiong, W., Xiaofei, H., Bin, W., & Tingli, M. (2013). Effect of enhanced pyrolysis platinized processes on the performance of counter electrodes. *Rare Metal Materials and Engineering, 42*(6), 1130-1133.

Gorlov, M., & Kloo, L. (2008). Ionic liquid electrolytes for dye-sensitized solar cells. *Dalton Transactions, 0*(20), 2655-2666.

Grätzel, M. (2003). Dye-sensitized solar cells. *Journal of Photochemistry and Photobiology C: Photochemistry Reviews, 4*(2), 145-153.

Grätzel, M. (2009). Recent advances in sensitized mesoscopic solar cells. *Accounts of Chemical Research, 42*(11), 1788-1798.

Green, M. A. (2009). The path to 25% silicon solar cell efficiency: History of silicon cell evolution. *Progress in Photovoltaics: Research and Applications, 17*(3), 183-189.

Grolik, J., Dudek, Ł., Eilmes, J., Eilmes, A., Górecki, M., Frelek, J., . . . Donnio, B. (2012). New chiral discotics with helical organization of the mesophase-liquid crystalline derivatives of dibenzotetraaza[14]annulene. *Tetrahedron, 68*(20), 3875-3884.

Guarnieri, M. (2015). More light on information [Historical]. *IEEE Industrial Electronics Magazine, 9*(4), 58-61.

Hagfeldt, A., Boschloo, G., Sun, L., Kloo, L., & Pettersson, H. (2010). Dye-sensitized solar cells. *Chemical Reviews, 110*(11), 6595-6663.

Harima, Y., Fujita, T., Kano, Y., Imae, I., Komaguchi, K., Ooyama, Y., & Ohshita, J. (2013). Lewis-acid sites of TiO_2 surface for adsorption of organic dye having pyridyl group as anchoring unit. *The Journal of Physical Chemistry C, 117*(32), 16364-16370.

Hart, A. S., Kc, C. B., Gobeze, H. B., Sequeira, L. R., & D'Souza, F. (2013). Porphyrin-sensitized solar sells: Effect of carboxyl anchor group orientation on the cell performance. *ACS Applied Materials & Interfaces, 5*(11), 5314-5323.

Honeybourne, C. L. (1974). Evidence for paramagnetic exaltation in a 4n-π -electron, (4n-2) - atom, conjugated molecules. *Tetrahedron Letters, 15*(35), 3075 - 3078.

Huang, H.-H., Chao, C.-G., Lee, S.-L., Wu, H.-J., Chen, C.-h., & Luh, T.-Y. (2012). Double stranded polymeric ladderphanes with 16-π-electron antiaromatic metallocycle linkers. *Organic & Biomolecular Chemistry, 10*(30), 5948-5953.

Huang, Z.-S., Zang, X.-F., Hua, T., Wang, L., Meier, H., & Cao, D. (2015). 2,3-Dipentyldithieno[3,2-f:2′,3′-h]quinoxaline-Based organic dyes for efficient dye-sensitized solar cells: Effect of π-bridges and electron donors on solar cell performance. *ACS Applied Materials & Interfaces, 7*(36), 20418-20429.

Jacobson, M. Z. (2009). Review of solutions to global warming, air pollution, and energy security. *Energy & Environmental Science, 2*(2), 148-173.

Jasim, K. E. (2011). Dye sensitized solar cells - Working principles, challenges, and opportunities. *Solar Cells - Dye Sensitized Devices* (pp. 171-203). Department of Physics, University of Bahrain, Kingdom of Bahrin: IntechOpen.

Jungsuttiwong, S., Sirithip, K., Prachumrak, N., Tarsang, R., Sudyoadsuk, T., Namuangruk, S., . . . Keawin, T. (2017). Significant enhancement in the performance of porphyrin for dye-sensitized solar cells: aggregation control using chenodeoxycholic acid. *New Journal of Chemistry, 41*(15), 7081-7091.

Jungsuttiwong, S., Yakhanthip, T., Surakhot, Y., Khunchalee, J., Sudyoadsuk, T., Promarak, V., . . . Namuangruk, S. (2012). The effect of conjugated spacer on novel carbazole derivatives for dye-sensitized solar cells: Density functional theory/time-dependent density functional theory study. *Journal of Computational Chemistry, 33*(17), 1517-1523.

Kay, A., & Graetzel, M. (1993). Artificial photosynthesis. 1. Photosensitization of titania solar cells with chlorophyll derivatives and related natural porphyrins. *The Journal of Physical Chemistry, 97*(23), 6272-6277.

Kee, J. W., Ng, Y. Y., Kulkarni, S. A., Muduli, S. K., Xu, K., Ganguly, R., . . . Soo, H. S. (2016). Development of bis(arylimino)acenaphthene (BIAN) copper complexes as visible light harvesters for potential photovoltaic applications. *Inorganic Chemistry Frontiers, 3*(5), 651-662.

Keita, B., Lu, Y. W., & Nadjo, L. (1994). Chemically-modified electrodes based on new metal-dibenzotetraaza [14] annulenes. *Journal of Electroanalytical Chemistry, 367*(1), 285-291.

Keita, F., Kenjiro, K., Naoki, K., Hiroyuki, K., & Hiroshi, O. (2010). Black-dye-adsorbed TiO_2 (110) electrodes studied by Frequency-Modulation Atomic Force microscopy. *Japanese Journal of Applied Physics, 49*(8S3), 08LB06.

Khaledi, H., Ali, H. M., & Olmstead, M. M. (2011). Versatile coordination modes of 2-(Diformylmethylene)-3,3-dimethylindole towards late-transition-metal ions: C–H bond activation and formation of cyclic acyl–palladium(II) complexes. *European Journal of Inorganic Chemistry, 2011*(15), 2394-2404.

Khaledi, H., Olmstead, M. M., Mohd Ali, H., & Thomas, N. F. (2013). Indolenine meso-substituted dibenzotetraaza[14]annulene and its coordination chemistry toward the transition metal ions Mn^{III}, Fe^{III}, Co^{II}, Ni^{II}, Cu^{II}, and Pd^{II}. *Inorganic Chemistry, 52*(4), 1926-1941.

Khanamiryan, A. K., Bhardwaj, N., & Leznoff, C. C. (2000). Towards N-alkylated phthalocyanines using 2,3,9,10,16,17,23,24-octaneopentoxyphthalocyanine. *Journal of Porphyrins and Phthalocyanines, 4*(5), 484-490.

Kitamura, T., Ikeda, M., Shigaki, K., Inoue, T., Anderson, N. A., Ai, X., . . . Yanagida, S. (2004). Phenyl-conjugated oligoene sensitizers for TiO_2 solar cells. *Chemistry of Materials, 16*(9), 1806-1812.

Klfout, H., Stewart, A., Elkhalifa, M., & He, H. (2017). BODIPYs for dye-sensitized solar cells. *ACS Applied Materials & Interfaces, 9*(46), 39873-39889.

Krishna, N. V., Krishna, J. V. S., Singh, S. P., Giribabu, L., Han, L., Bedja, I., . . . Islam, A. (2017). Donor-π–acceptor based stable porphyrin sensitizers for dye-sensitized solar cells: Effect of π-conjugated spacers. *The Journal of Physical Chemistry C, 121*(12), 6464-6477.

Kusama, H., & Arakawa, H. (2004). Influence of alkylaminopyridine additives in electrolytes on dye-sensitized solar cell performance. *Solar Energy Materials and Solar Cells, 81*(1), 87-99.

Ladomenou, K., Kitsopoulos, T. N., Sharma, G. D., & Coutsolelos, A. G. (2014). The importance of various anchoring groups attached on porphyrins as potential dyes for DSSC applications. *RSC Advances, 4*(41), 21379-21404.

Le Bahers, T., Pauporté, T., Lainé, P. P., Labat, F., Adamo, C., & Ciofini, I. (2013). Modeling dye-sensitized solar cells: From theory to experiment. *The Journal of Physical Chemistry Letters, 4*(6), 1044-1050.

Li, R., Liu, J., Cai, N., Zhang, M., & Wang, P. (2010). Synchronously reduced surface states, charge recombination, and light absorption length for high-performance organic dye-sensitized solar cells. *The Journal of Physical Chemistry B, 114*(13), 4461-4464.

Liao, J., Zhao, H., Xu, Y., Zhou, W., Peng, F., Wang, Y., & Fang, Y. (2017). Novel BODIPY dyes with electron donor variety for dye-sensitized solar cells. *RSC Advances, 7*(54), 33975-33985.

Listorti, A., O'Regan, B., & Durrant, J. R. (2011). Electron transfer dynamics in dye-sensitized solar cells. *Chemistry of Materials, 23*(15), 3381-3399.

Liu, H., Bo, R., Liu, H., Li, N., Xu, Q., Li, H., . . . Wang, L. (2014). Study of the influences of molecular planarity and aluminum evaporation rate on the performances of electrical memory devices. *Journal of Materials Chemistry C, 2*(28), 5709-5716.

Liu, J., Li, R., Si, X., Zhou, D., Shi, Y., Wang, Y., . . . Wang, P. (2010). Oligothiophene dye-sensitized solar cells. *Energy & Environmental Science, 3*(12), 1924-1928.

Liu, Y., Xiang, N., Feng, X., Shen, P., Zhou, W., Weng, C., . . . Tan, S. (2009). Thiophene-linked porphyrin derivatives for dye-sensitized solar cells. *Chemical Communications, 0*(18), 2499-2501.

Magnano, G., Marinotto, D., Cipolla, M. P., Trifiletti, V., Listorti, A., Mussini, P. R., . . . Pizzotti, M. (2016). Influence of alkoxy chain envelopes on the interfacial photoinduced processes in tetraarylporphyrin-sensitized solar cells. *Physical Chemistry Chemical Physics, 18*(14), 9577-9585.

Mai, C.-L., Moehl, T., Hsieh, C.-H., Décoppet, J.-D., Zakeeruddin, S. M., Grätzel, M., & Yeh, C.-Y. (2015). Porphyrin sensitizers bearing a pyridine-type anchoring group for dye-sensitized solar cells. *ACS Applied Materials & Interfaces, 7*(27), 14975-14982.

Masuko, K., Shigematsu, M., Hashiguchi, T., Fujishima, D., Kai, M., Yoshimura, N., . . . Okamoto, S. (2014). Achievement of more than 25% conversion efficiency with crystalline silicon heterojunction solar cell. *IEEE Journal of Photovoltaics, 4*(6), 1433-1435.

Mathew, S., Yella, A., Gao, P., Humphry-Baker, R., Curchod, B. F. E., Ashari-Astani, N., . . . Grätzel, M. (2014). Dye-sensitized solar cells with 13% efficiency achieved through the molecular engineering of porphyrin sensitizers. *Nature Chemistry, 6*(3), 242-247.

Max, J.-J., & Chapados, C. (2004). Infrared spectroscopy of aqueous carboxylic acids: Comparison between different acids and their salts. *The Journal of Physical Chemistry A, 108*(16), 3324-3337.

Mingsukang, M. A., Buraidah, M. H., Careem, M. A., Albinsson, I., Mellander, B. E., & Arof, A. K. (2017). Investigation of counter electrode materials for gel polymer electrolyte based quantum dot sensitized solar cells. *Electrochimica Acta, 241*, 487-496.

Mountford, P. (1998). Dibenzotetraaza[14]annulenes: versatile ligands for transition and main group metal chemistry. *Chemical Society Reviews, 27*(2), 105-116.

Mulyana, Y., Lindoy, L. F., Kepert, C. J., McMurtrie, J., Parkin, A., Turner, P., . . . Wilson, J. G. (2011). New metal organic frameworks incorporating the ditopic macrocyclic ligand dipyridyldibenzotetraaza[14]annulene. *Journal of Inclusion Phenomena and Macrocyclic Chemistry, 71*(3), 455-462.

Nagarajan, B., Kushwaha, S., Elumalai, R., Mandal, S., Ramanujam, K., & Raghavachari, D. (2017). Novel ethynyl-pyrene substituted phenothiazine based metal free organic dyes in DSSC with 12% conversion efficiency. *Journal of Materials Chemistry A, 5*(21), 10289-10300.

Nagarjuna, G., Kokil, A., Kumar, J., & Venkataraman, D. (2012). A straightforward route to electron transporting conjugated polymers. *Journal of Materials Chemistry, 22*(31), 16091-16094.

Ning, Z., Fu, Y., & Tian, H. (2010). Improvement of dye-sensitized solar cells: what we know and what we need to know. *Energy & Environmental Science, 3*(9), 1170-1181.

Ning, Z., Zhang, Q., Wu, W., Pei, H., Liu, B., & Tian, H. (2008). Starburst triarylamine based dyes for efficient dye-sensitized solar cells. *The Journal of Organic Chemistry, 73*(10), 3791-3797.

O'Regan, B., & Grätzel, M. (1991). A low-cost, high-efficiency solar cell based on dye-sensitized colloidal TiO_2 films. *Nature, 353*(6346), 737-740.

Omata, K., Kuwahara, S., Katayama, K., Qing, S., Toyoda, T., Lee, K.-M., & Wu, C.-G. (2015). The cause for the low efficiency of dye sensitized solar cells with a combination of ruthenium dyes and cobalt redox. *Physical Chemistry Chemical Physics, 17*(15), 10170-10175.

Ozawa, H., Shimizu, R., & Arakawa, H. (2012). Significant improvement in the conversion efficiency of black-dye-based dye-sensitized solar cells by cosensitization with organic dye. *RSC Advances, 2*(8), 3198-3200.

Pareek, Y., Lakshmi, V., & Ravikanth, M. (2014). Axially bonded pentads constructed on the Sn(IV) porphyrin scaffold. *Dalton Transactions, 43*(18), 6870-6879.

Perrin, L., & Hudhomme, P. (2011). Synthesis, electrochemical and optical absorption properties of new perylene-3,4:9,10-bis(dicarboximide) and perylene-3,4:9,10-bis(benzimidazole) derivatives. *European Journal of Organic Chemistry, 2011*(28), 5427-5440.

Prachumrak, N., Sudyoadsuk, T., Thangthong, A., Nalaoh, P., Jungsuttiwong, S., Daengngern, R., . . . Promarak, V. (2017). Improvement of D-π-A organic dye-based dye-sensitized solar cell performance by simple triphenylamine donor substitutions on the π-linker of the dye. *Materials Chemistry Frontiers, 1*(6), 1059-1072.

Qi, B., & Wang, J. (2012). Open-circuit voltage in organic solar cells. *Journal of Materials Chemistry, 22*(46), 24315-24325.

Ragoussi, M.-E., & Torres, T. (2015). New generation solar cells: concepts, trends and perspectives. *Chemical Communications, 51*(19), 3957-3972.

Rashidi, A., Afghan, A., Baradarani, M. M., & Joule, J. A. (2009). The synthesis of 4-(3,3-dimethyl-3H-pyrrolo[2,3-f]quinolin-2-yl)pyrazoles and 4-(3,3-dimethyl-3H-pyrrolo[3,2-h]quinolin-2-yl)pyrazoles. *Journal of Heterocyclic Chemistry, 46*(3), 428-431.

Reddy, P. M., Rohini, R., Krishna, E. R., Hu, A., & Ravinder, V. (2012). Synthesis, spectral and antibacterial studies of copper(II) tetraaza macrocyclic complexes. *International Journal of Molecular Sciences, 13*(4), 4982-4992.

Reichardt, C. (1994). Solvatochromic dyes as solvent polarity indicators. *Chemical Reviews, 94*(8), 2319-2358.

Reichardt, C., & Scheibelein, W. (1978). Syntheses with aliphatic dialdehydes, XXVII [1] A non-template synthesis for the preparation of metal-free 1,4,8,11-Tetraaza[14]annulene derivatives. *Zeitschrift fuer Naturforschung, Teil B: Anorganische Chemie, Organische Chemie, 33 b*(9), 1012-1015.

Sakata, K., & Itoh, M. (1992). Synthesis and characterization of 7,16-dinicotinoyl- and 7,16-diisonicotinoyltetraaza[14]annulene and their nickel(II) and copper(II) complexes. *Journal of Heterocyclic Chemistry, 29*(4), 921-926.

Sakata, K., Shimoda, M., & Hashimoto, M. (1996). Preparation and characterization of tetraaza[14]annulene and its nickel(II) and copper(II) complexes with crown ether functionalities. *Journal of Heterocyclic Chemistry, 33*(6), 1593-1598.

Sarker, S., Ahammad, A. J. S., Seo, H. W., & Kim, D. M. (2014). Electrochemical impedance spectra of dye-sensitized solar Cells: Fundamentals and spreadsheet calculation. *International Journal of Photoenergy, 2014*, 1-17.

Schiermeier, Q., Tollefson, J., Scully, T., Witze, A., & Morton, O. (2008). Energy alternatives: Electricity without carbon. *Nature, 454*(7206), 816-823.

Sepehrifard, A., Chen, S., Stublla, A., Potvin, P. G., & Morin, S. (2013). Effects of ligand LUMO levels, anchoring groups and spacers in Ru(II)-based terpyridine and dipyrazinylpyridine complexes on adsorption and photoconversion efficiency in DSSCs. *Electrochimica Acta, 87*(Supplement C), 236-244.

Sepehrifard, A., Stublla, A., Haftchenary, S., Chen, S., Potvin, P. G., & Morin, S. (2008). Effects of carboxyl and ester anchoring groups on solar conversion efficiencies of TiO_2 dye-sensitized solar cells. *Journal of New Materials for Electrochemical Systems, 11*(4), 281-285.

Shang, H., Luo, Y., Guo, X., Huang, X., Zhan, X., Jiang, K., & Meng, Q. (2010). The effect of anchoring group number on the performance of dye-sensitized solar cells. *Dyes and Pigments, 87*(3), 249-256.

Sister, E., Gottfried, V., Kapon, M., Kaftory, M., Dori, Z., & Gray, H. B. (1988). Structural characterization of the product of oxidation of a macrocyclic cobalt(II) complex in pyridine solution. *Inorganic Chemistry, 27*(4), 600-604.

Song, H., Liu, Q., & Xie, Y. (2018). Porphyrin-sensitized solar cells: systematic molecular optimization, coadsorption and cosensitization. *Chemical Communications, 54*(15), 1811-1824.

Stojkovic, M. R., Marjanovic, M., Pawlica, D., Dudek, L., Eilmes, J., Kralj, M., & Piantanida, I. (2010). Cationic side-chains control DNA/RNA binding properties and antiproliferative activity of dicationic dibenzotetraaza[14]annulene derivatives. *New Journal of Chemistry, 34*(3), 500-507.

Sustmann, R., Korth, H.-G., Kobus, D., Baute, J., Seiffert, K.-H., Verheggen, E., . . . de Groot, H. (2007). FeIII complexes of 1,4,8,11-Tetraaza[14]annulenes as catalase mimics. *Inorganic Chemistry, 46*(26), 11416-11430.

Taib, M. A. A., Tan, W. K., Okuno, T., Kawamura, G., Jaafar, M., Razak, K. A., . . . Lockman, Z. (2016). Formation of TiO_2 nanotube arrays by anodic oxidation in LiOH added ethylene glycol electrolyte and the effect of thermal annealing on the photoelectrochemical properties. *AIP Conference Proceedings, 1733*(1), 020025.

Teng, C., Yang, X., Yang, C., Li, S., Cheng, M., Hagfeldt, A., & Sun, L. (2010). Molecular design of anthracene-bridged metal-free organic dyes for efficient dye-sensitized solar cells. *The Journal of Physical Chemistry C, 114*(19), 9101-9110.

Thalluri, G. K. V. V., Décultot, M., Henrist, C., Dewalque, J., Colson, P., Habraken, S., . . . Cloots, R. (2013). Morphological and opto-electrical properties of a solution deposited platinum counter electrode for low cost dye sensitized solar cells. *Physical Chemistry Chemical Physics, 15*(45), 19799-19806.

Theerthagiri, J., Senthil, A. R., Madhavan, J., & Maiyalagan, T. (2015). Recent progress in non-platinum counter electrode materials for dye-sensitized solar cells. *ChemElectroChem, 2*(7), 928-945.

Theerthagiri, J., Senthil, R. A., Buraidah, M. H., Madhavan, J., Arof, A. K., & Ashokkumar, M. (2016). One-step electrochemical deposition of Ni1-xMoxS ternary sulfides as an efficient counter electrode for dye-sensitized solar cells. *Journal of Materials Chemistry A, 4*(41), 16119-16127.

Thomas, S., Deepak, T. G., Anjusree, G. S., Arun, T. A., Nair, S. V., & Nair, A. S. (2014). A review on counter electrode materials in dye-sensitized solar cells. *Journal of Materials Chemistry A, 2*(13), 4474-4490.

Tomasulo, M., Kaanumal, S. L., Sortino, S., & Raymo, F. M. (2007). Synthesis and properties of benzophenone−spiropyran and naphthalene−spiropyran conjugates. *The Journal of Organic Chemistry, 72*(2), 595-605.

Urbani, M., Grätzel, M., Nazeeruddin, M. K., & Torres, T. (2014). Meso-substituted porphyrins for dye-sensitized solar cells. *Chemical Reviews, 114*(24), 12330-12396.

Vinayak, M. V., Lakshmykanth, T. M., Yoosuf, M., Soman, S., & Gopidas, K. R. (2016). Effect of recombination and binding properties on the performance of dye sensitized solar cells based on propeller shaped triphenylamine dyes with multiple binding groups. *Solar Energy, 124*(Supplement C), 227-241.

Wan, Z., Jia, C., Duan, Y., Zhou, L., Lin, Y., & Shi, Y. (2012). Phenothiazine-triphenylamine based organic dyes containing various conjugated linkers for efficient dye-sensitized solar cells. *Journal of Materials Chemistry, 22*(48), 25140-25147.

Wang, P., Zakeeruddin, S. M., Comte, P., Charvet, R., Humphry-Baker, R., & Grätzel, M. (2003). Enhance the performance of dye-sensitized solar cells by co-grafting amphiphilic sensitizer and hexadecylmalonic acid on TiO_2 nanocrystals. *The Journal of Physical Chemistry B, 107*(51), 14336-14341.

Wang, Z.-S., Cui, Y., Dan-oh, Y., Kasada, C., Shinpo, A., & Hara, K. (2007). Thiophene-functionalized coumarin dye for efficient dye-sensitized solar cells: Electron lifetime improved by coadsorption of deoxycholic acid. *The Journal of Physical Chemistry C, 111*(19), 7224-7230.

Whyte, A. M., Shuku, Y., Nichol, G. S., Matsushita, M. M., Awaga, K., & Robertson, N. (2012). Planar Ni(II), Cu(II) and Co(II) tetraaza[14]annulenes: structural, electronic and magnetic properties and application to field effect transistors. *Journal of Materials Chemistry, 22*(34), 17967-17975.

Williams, D. B. G., & Lawton, M. (2010). Drying of organic solvents: Quantitative evaluation of the efficiency of several desiccants. *The Journal of Organic Chemistry, 75*(24), 8351-8354.

Wu, J., Lan, Z., Lin, J., Huang, M., Huang, Y., Fan, L., & Luo, G. (2015). Electrolytes in dye-sensitized solar cells. *Chemical Reviews, 115*(5), 2136-2173.

Wu, J., Lan, Z., Lin, J., Huang, M., Huang, Y., Fan, L., . . . Wei, Y. (2017). Counter electrodes in dye-sensitized solar cells. *Chemical Society Reviews, 46*(19), 5975-6023.

Wu, M., Lin, X., Wang, Y., Wang, L., Guo, W., Qi, D., . . . Ma, T. (2012). Economical Pt-Free catalysts for counter electrodes of dye-sensitized solar cells. *Journal of the American Chemical Society, 134*(7), 3419-3428.

Xue, X., Zhang, W., Zhang, N., Ju, C., Peng, X., Yang, Y., . . . Zhang, B. (2014). Effect of the length of the alkyl chains in porphyrin meso-substituents on the performance of dye-sensitized solar cells. *RSC Advances, 4*(17), 8894-8900.

Yao, B.-Q., Sun, J.-S., Tian, Z.-F., Ren, X.-M., Gu, D.-W., Shen, L.-J., & Xie, J. (2008). Ion-pair charge transfer complexes with intense near IR absorption: Syntheses, crystal structures, electronic spectra and DFT calculations. *Polyhedron, 27*(13), 2833-2844.

Yu, L., Shi, W., Lin, L., Liu, Y., Li, R., Peng, T., & Li, X. (2014). Effects of benzo-annelation of asymmetric phthalocyanine on the photovoltaic performance of dye-sensitized solar cells. *Dalton Transactions, 43*(22), 8421-8430.

Yu, Q.-Y., Liao, J.-Y., Zhou, S.-M., Shen, Y., Liu, J.-M., Kuang, D.-B., & Su, C.-Y. (2011). Effect of hydrocarbon chain length of disubstituted triphenyl-amine-based organic dyes on dye-sensitized solar cells. *The Journal of Physical Chemistry C, 115*(44), 22002-22008.

Yum, J.-H., Baranoff, E., Kessler, F., Moehl, T., Ahmad, S., Bessho, T., . . . Grätzel, M. (2012). A cobalt complex redox shuttle for dye-sensitized solar cells with high open-circuit potentials. *Nature Communications, 3*(631), 1-8.

Zervaki, G. E., Angaridis, P. A., Koukaras, E. N., Sharma, G. D., & Coutsolelos, A. G. (2014). Dye-sensitized solar cells based on triazine-linked porphyrin dyads containing one or two carboxylic acid anchoring groups. *Inorganic Chemistry Frontiers, 1*(3), 256-270.

Zhang, L., & Cole, J. M. (2015). Anchoring groups for dye-sensitized solar cells. *ACS Applied Materials & Interfaces, 7*(6), 3427-3455.

Zhang, T., Qian, X., Zhang, P.-F., Zhu, Y.-Z., & Zheng, J.-Y. (2015). A meso-meso directly linked porphyrin dimer-based double D-π-A sensitizer for efficient dye-sensitized solar cells. *Chemical Communications, 51*(18), 3782-3785.

Zhang, X.-H., Cui, Y., Katoh, R., Koumura, N., & Hara, K. (2010). Organic dyes containing thieno[3,2-b]indole donor for efficient dye-sensitized solar cells. *The Journal of Physical Chemistry C, 114*(42), 18283-18290.

Zhu, K., Neale, N. R., Halverson, A. F., Kim, J. Y., & Frank, A. J. (2010). Effects of annealing temperature on the charge-collection and light-harvesting properties of TiO_2 nanotube-based dye-sensitized solar cells. *The Journal of Physical Chemistry C, 114*(32), 13433-13441.

Zwolinski, K. M., & Eilmes, J. (2016). New developments in porphyrin-like macrocyclic chemistry: a novel family of dibenzotetraaza[14]annulene-based cofacial dimers. *Chemical Communications, 52*(21), 4084-4087.

Zwolinski, K. M., Sieron, L., & Eilmes, J. (2018). One-flask synthesis of dibenzotetraaza[14]annulene cyclic congeners bearing buta-1,3-diyne bridges. *Organic Chemistry Frontiers, 5*(2), 171-178.

LIST OF PAPERS PRESENTED

1. Indolenine - dibenzotetraaza[14]annulene for dye - sensitized solar cells: Synthesis, characterizations and geometries optimized structures. Chemistry Poster Presentation Showcase Symposium, 3rd March 2016, University of Malaya, Kuala Lumpur, Malaysia.

2. "Tetraaza[14]annulene – based dye sensitized solar cell dyes: Design, synthesis and DFT computational studies". International Conference in Organic Synthesis 2016, 21st – 24th August 2016, Majestic Hotel, Kuching, Sarawak, Malaysia.

APPENDIX A: NMR SPECTRA

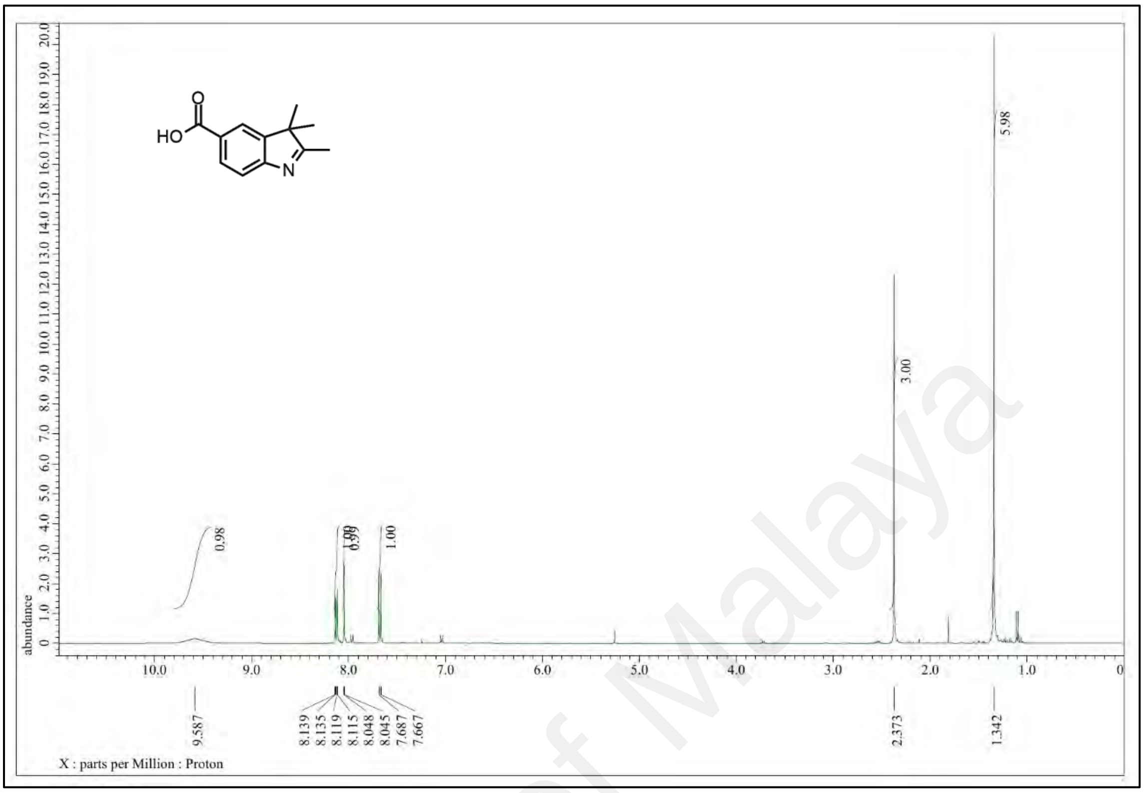

Appendix A.1: ^{1}H NMR (400 MHz, CDCl$_3$) spectrum of **1**.

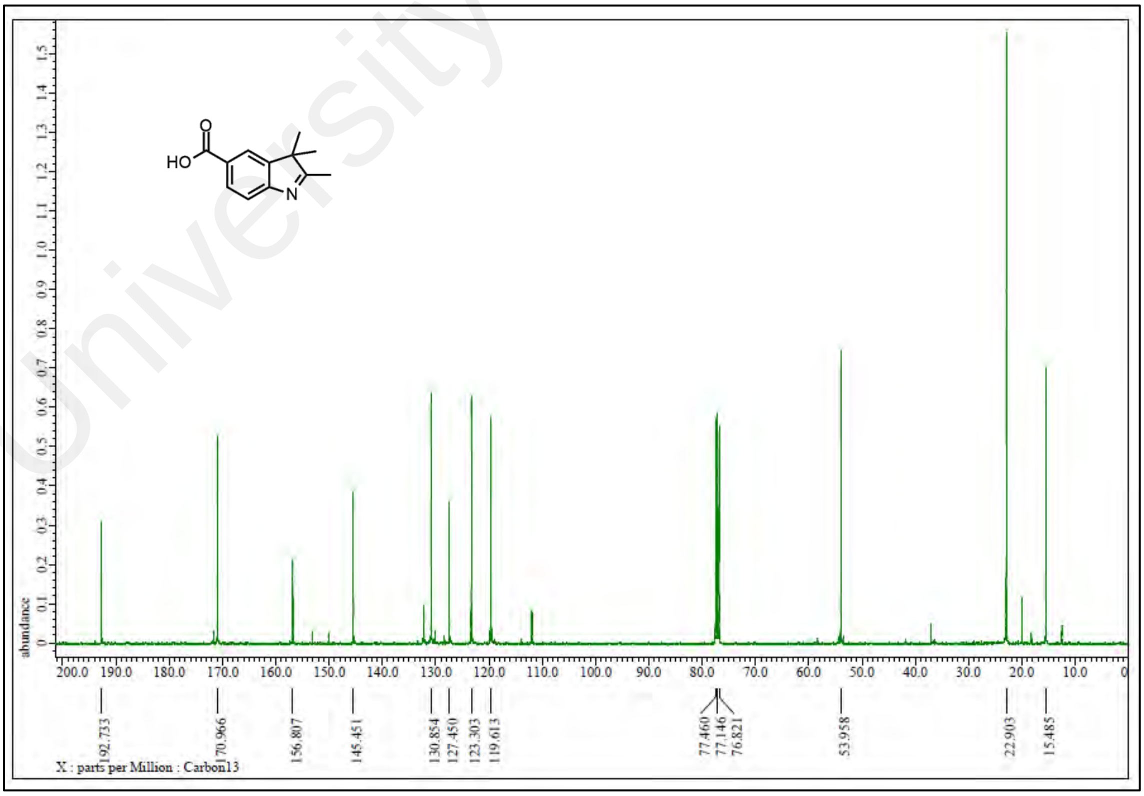

Appendix A.2: ^{13}C NMR (100 MHz, CDCl$_3$) spectrum of **1**.

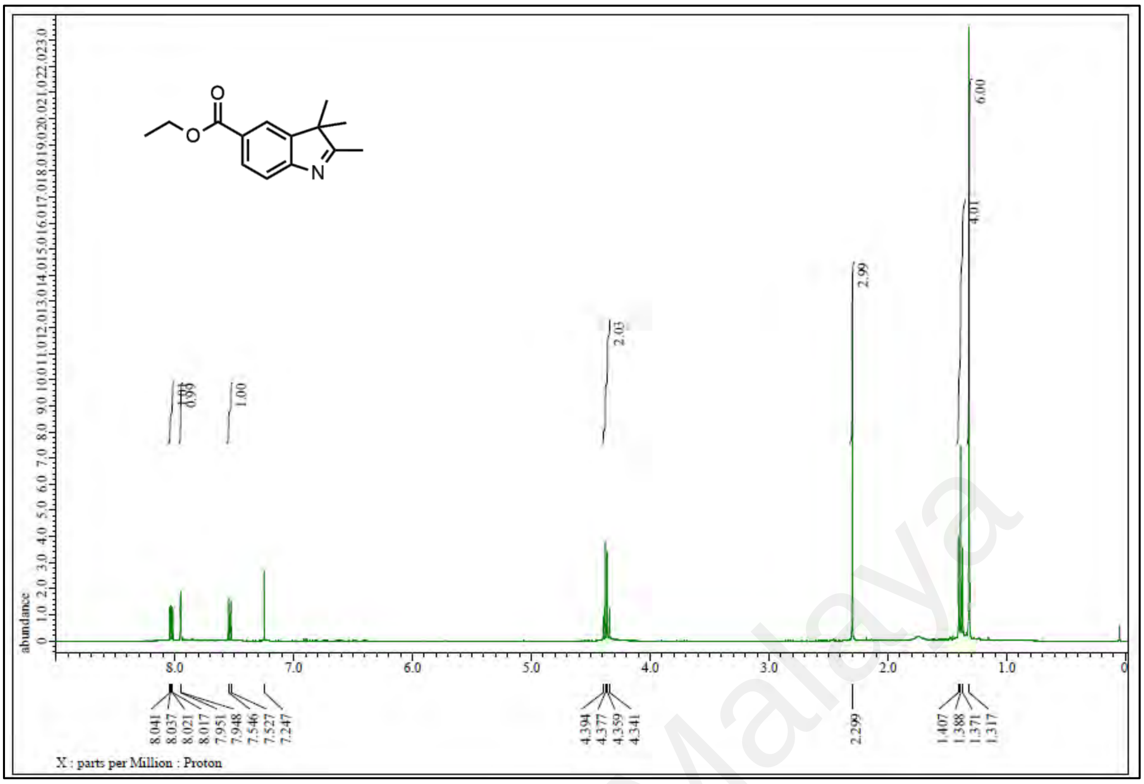

Appendix A.3: ^{1}H NMR (400 MHz, $CDCl_3$) spectrum of **2**.

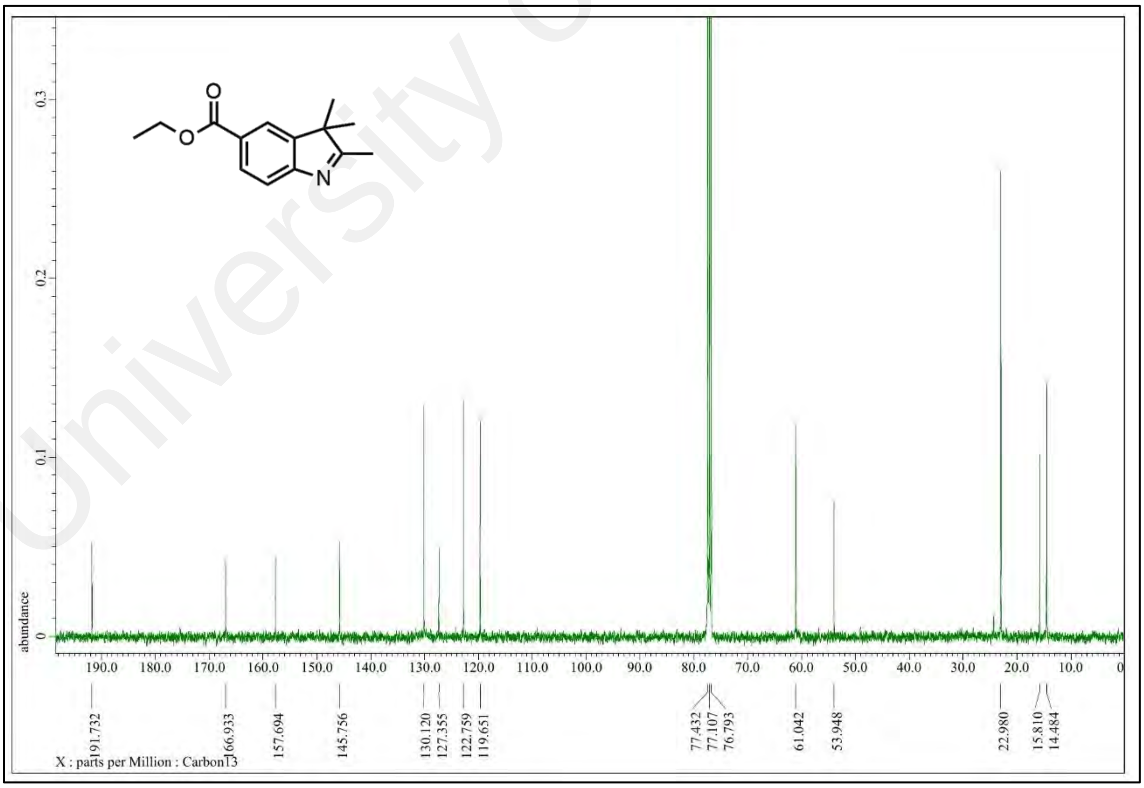

Appendix A.4: ^{13}C NMR (100 MHz, $CDCl_3$) spectrum of **2**.

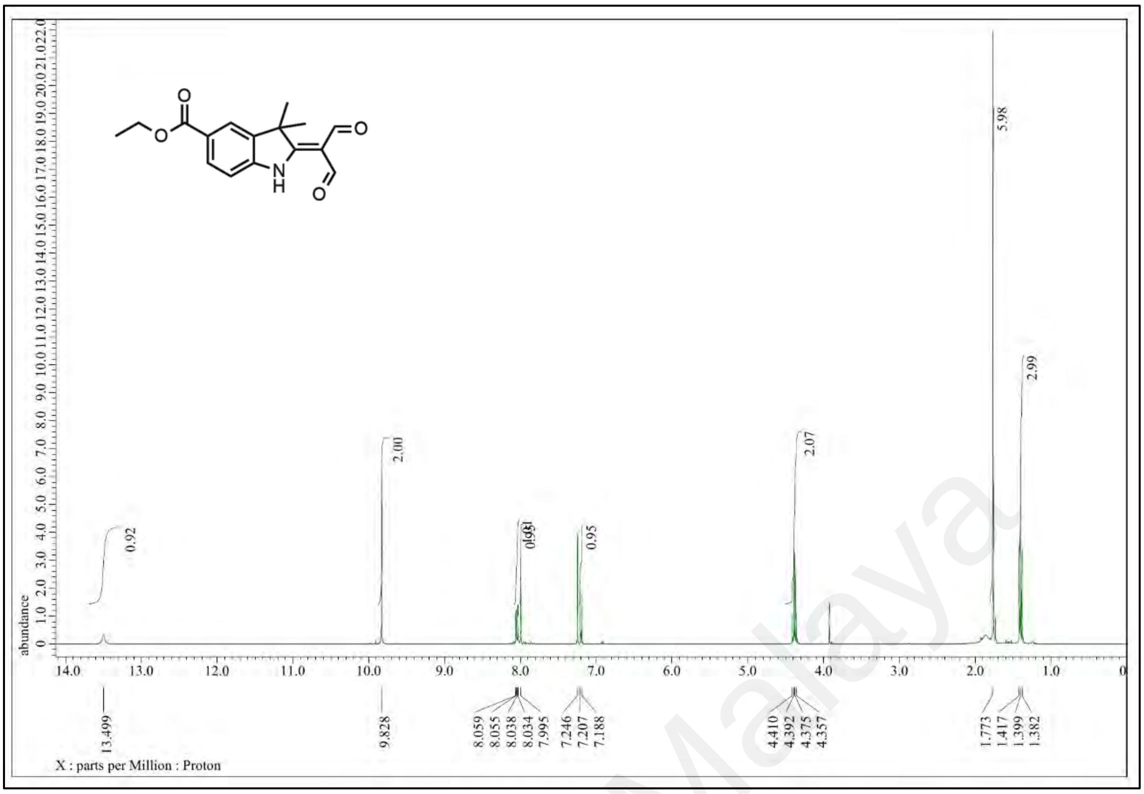

Appendix A.5: ^{1}H NMR (400 MHz, $CDCl_3$) spectrum of **3**.

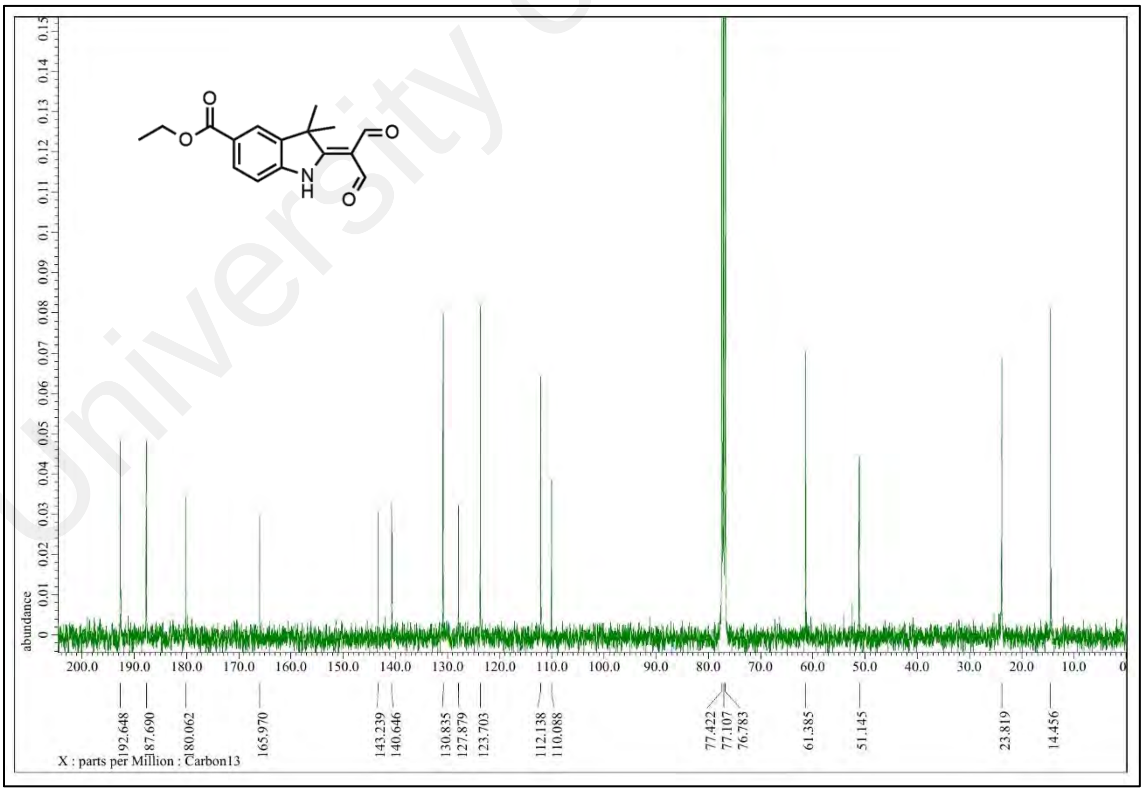

Appendix A.6: ^{13}C NMR (100 MHz, $CDCl_3$) spectrum of **3**.

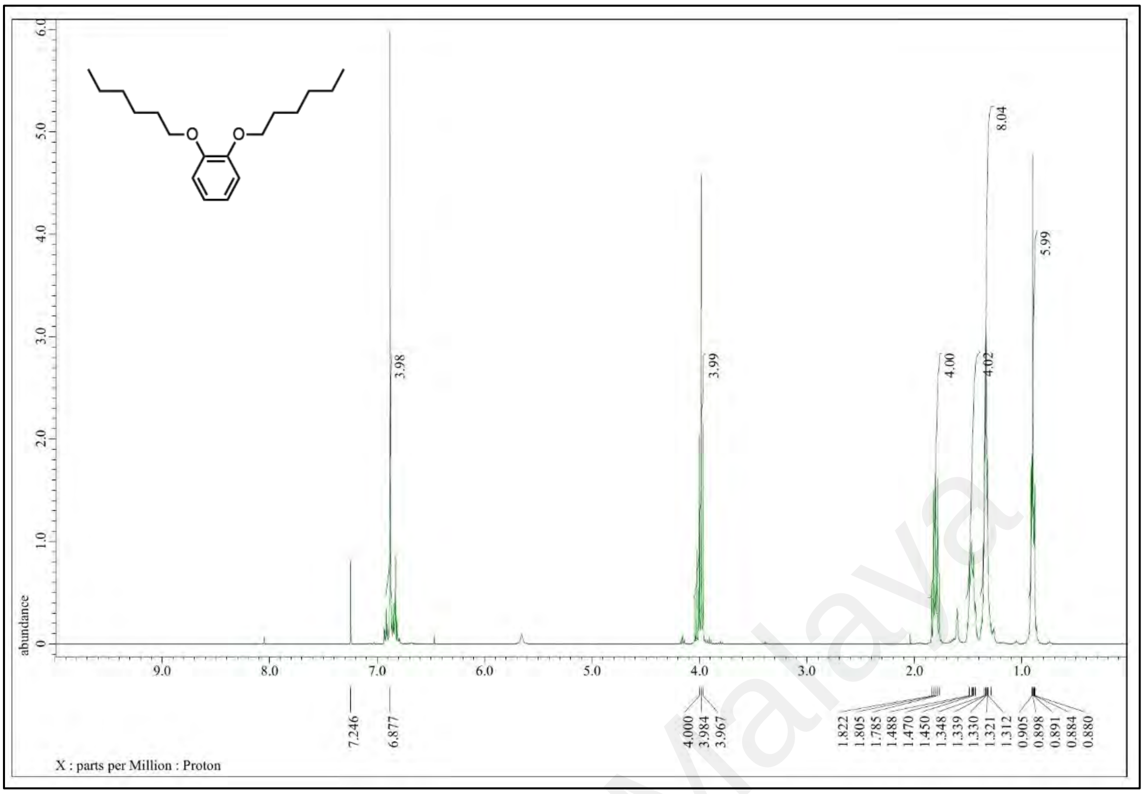

Appendix A.7: ^{1}H NMR (400 MHz, $CDCl_3$) spectrum of **4b**.

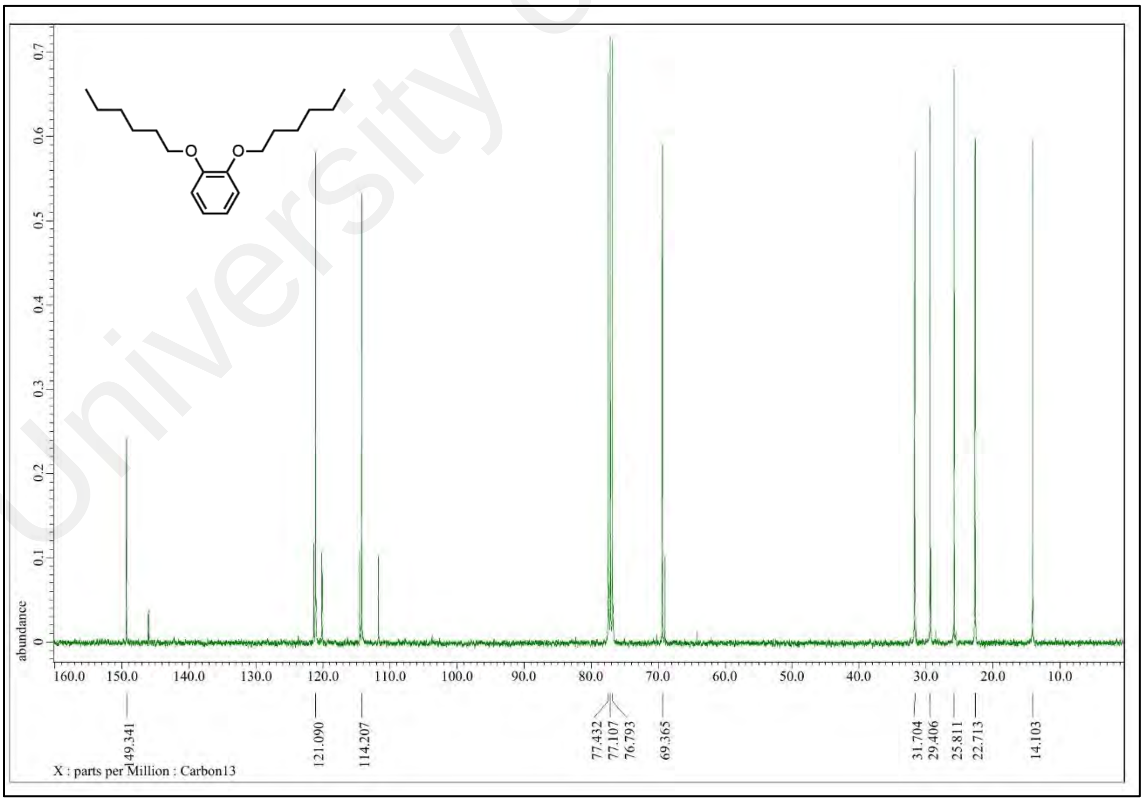

Appendix A.8: ^{13}C NMR (100 MHz, $CDCl_3$) spectrum of **4b**.

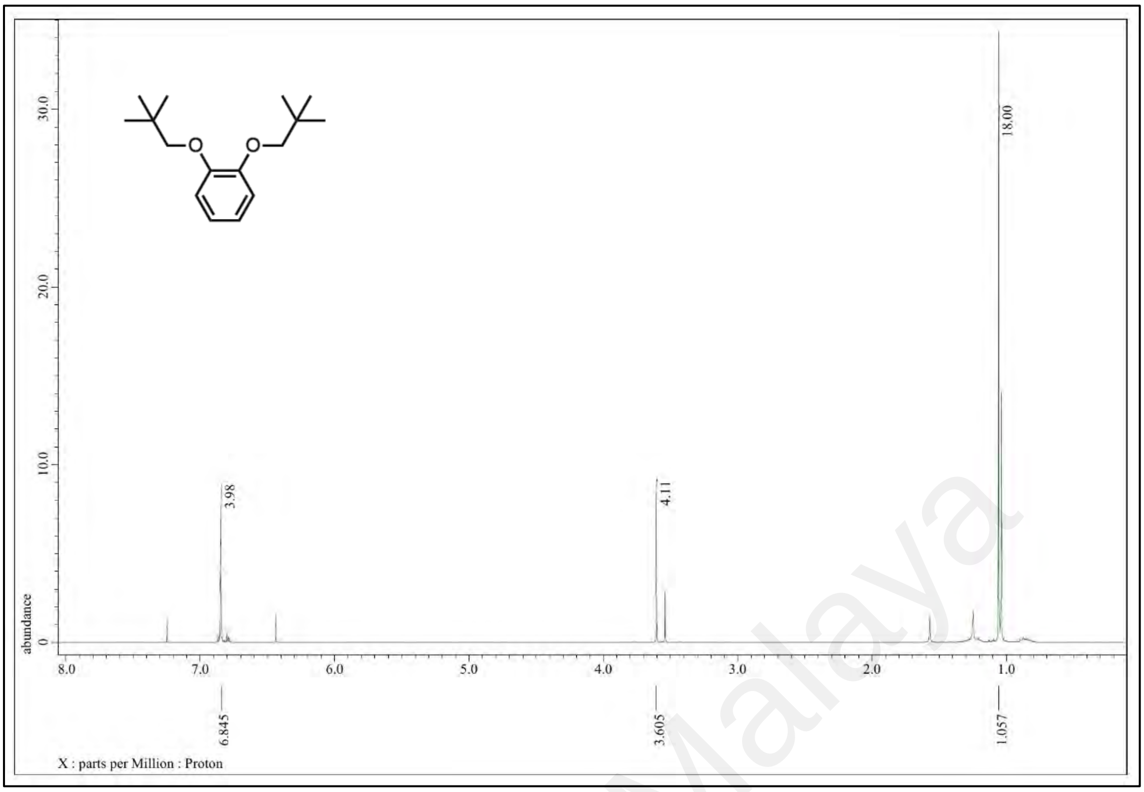

Appendix A.9: ^{1}H NMR (400 MHz, CDCl$_3$) spectrum of **4c**.

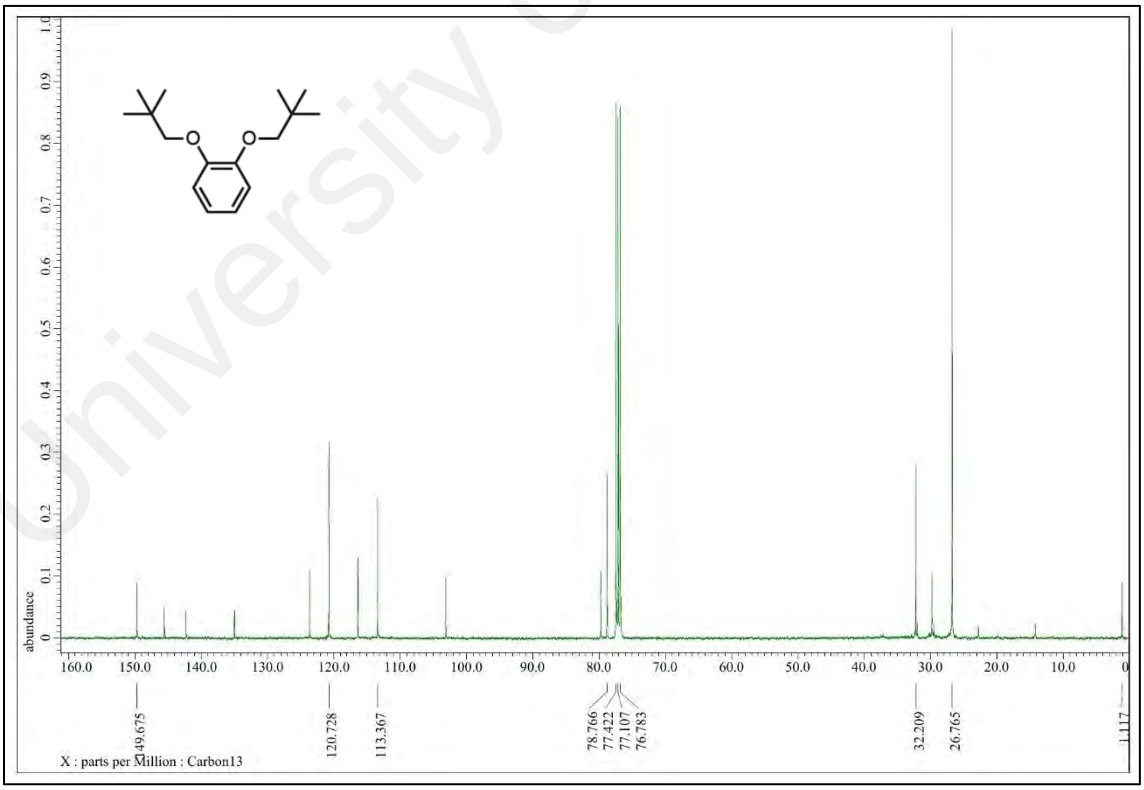

Appendix A.10: ^{13}C NMR (100 MHz, CDCl$_3$) spectrum of **4c**.

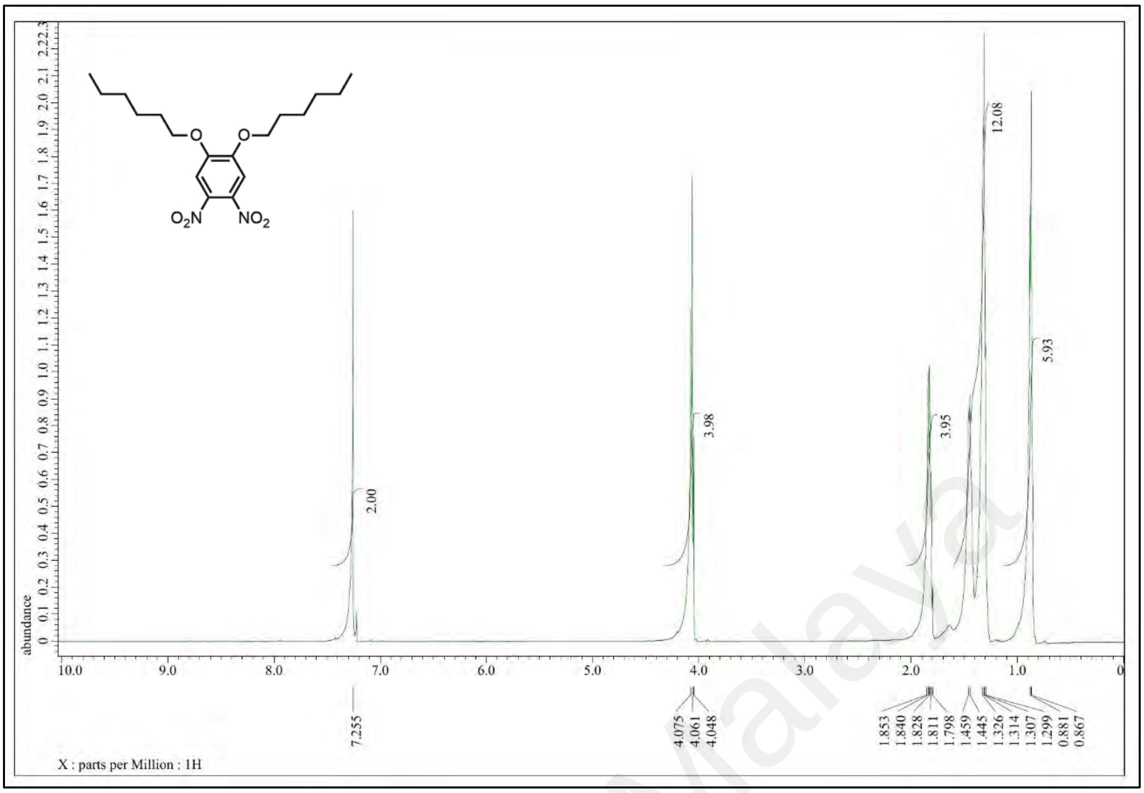

Appendix A.11: ^{1}H NMR (500 MHz, $CDCl_3$) spectrum of **5b**.

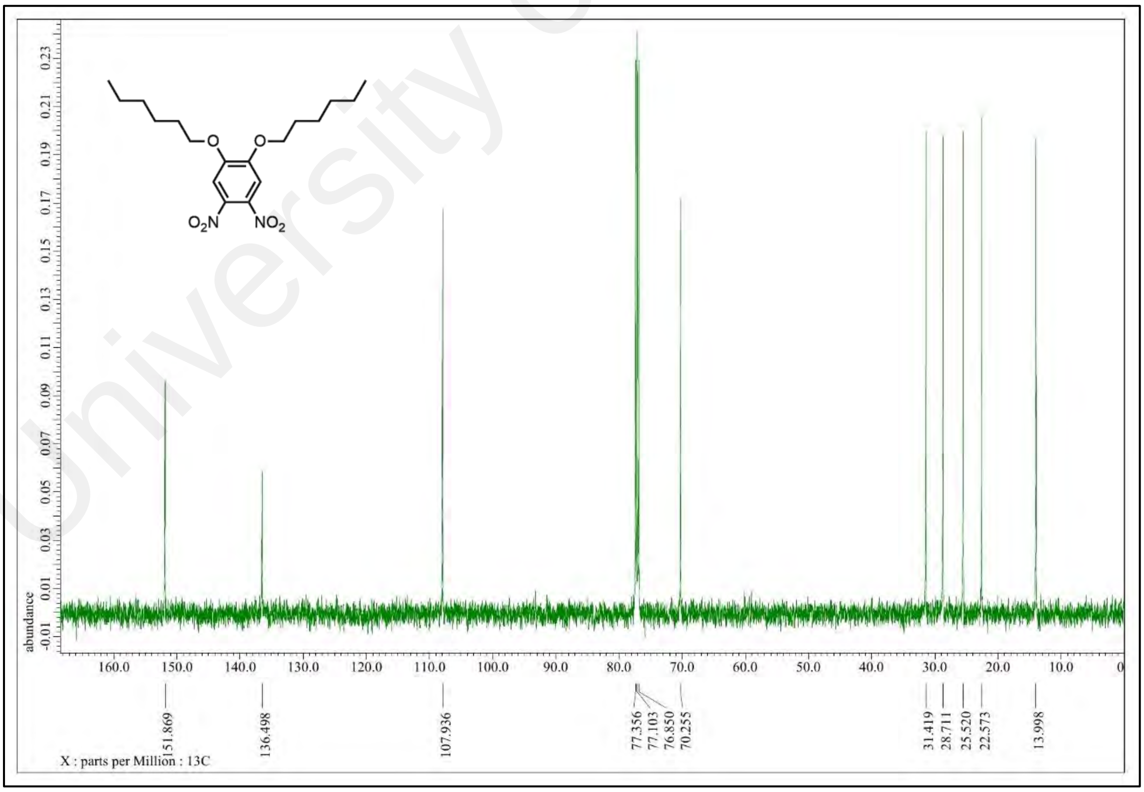

Appendix A.12: ^{13}C NMR (125 MHz, $CDCl_3$) spectrum of **5b**.

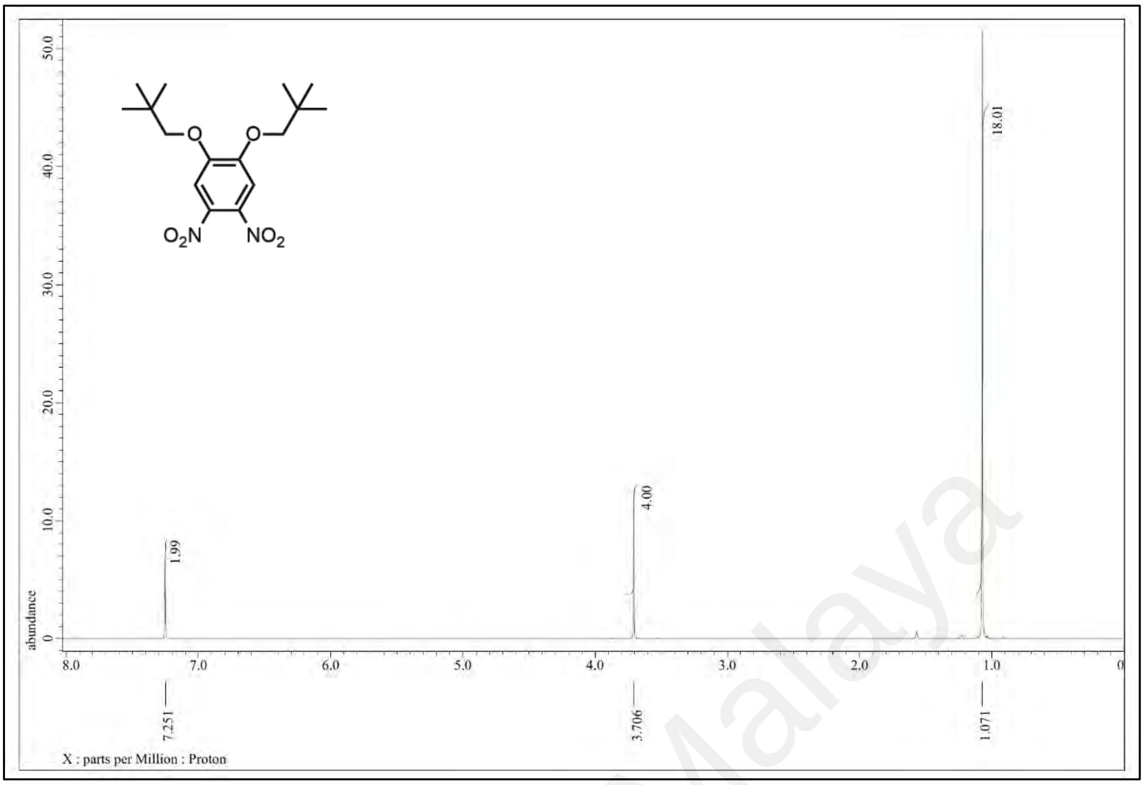

Appendix A.13: ^{1}H NMR (400 MHz, $CDCl_3$) spectrum of **5c**.

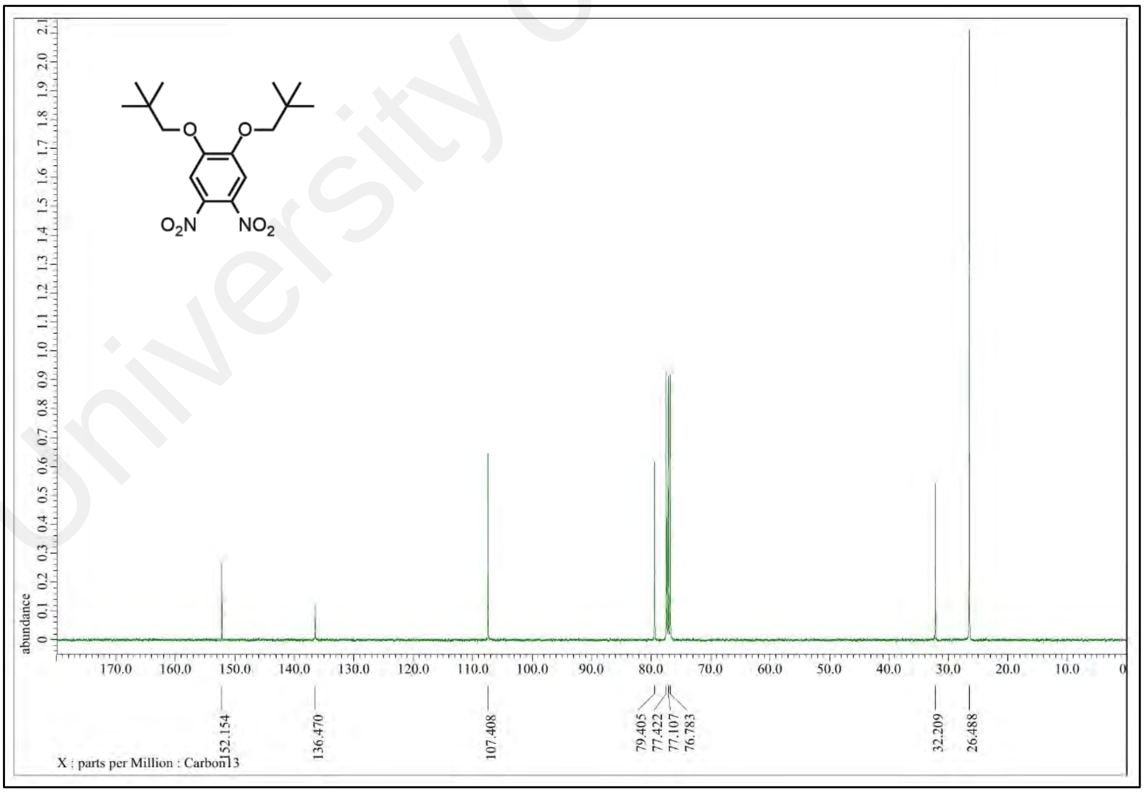

Appendix A.14: ^{13}C NMR (100 MHz, $CDCl_3$) spectrum of **5c**.

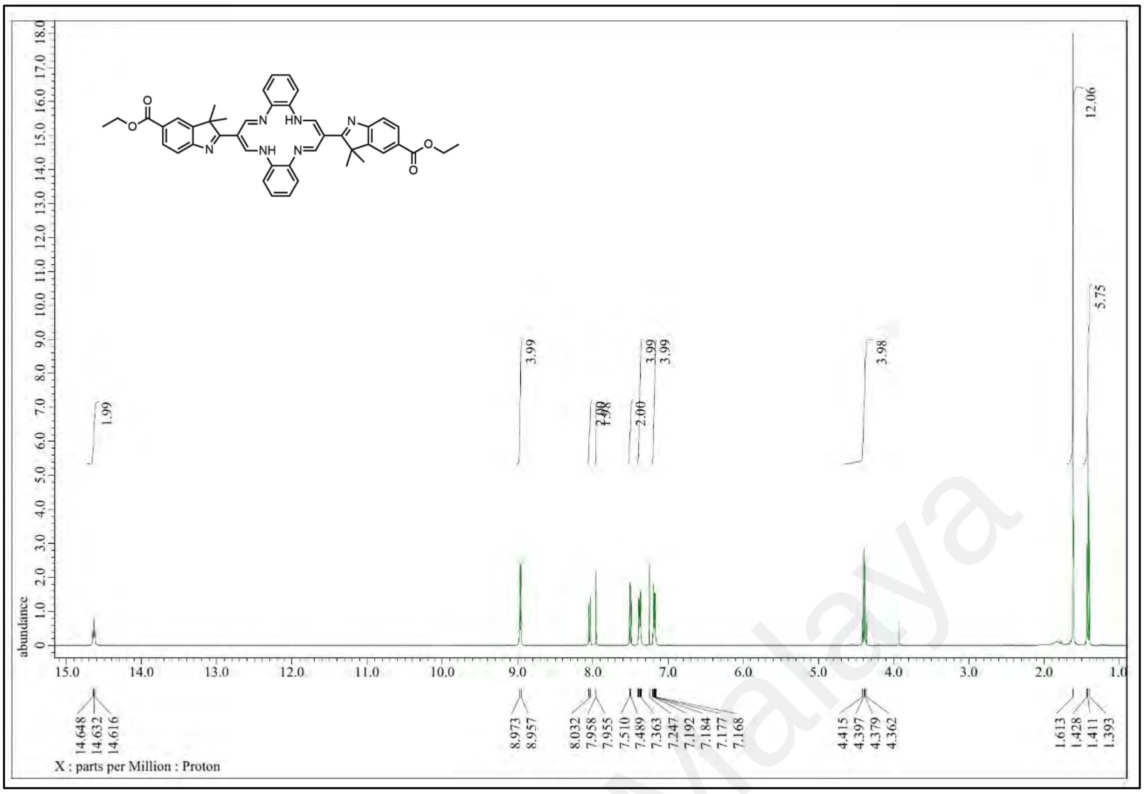

Appendix A.15: ^{1}H NMR (400 MHz, CDCl$_3$) spectrum of **7a**.

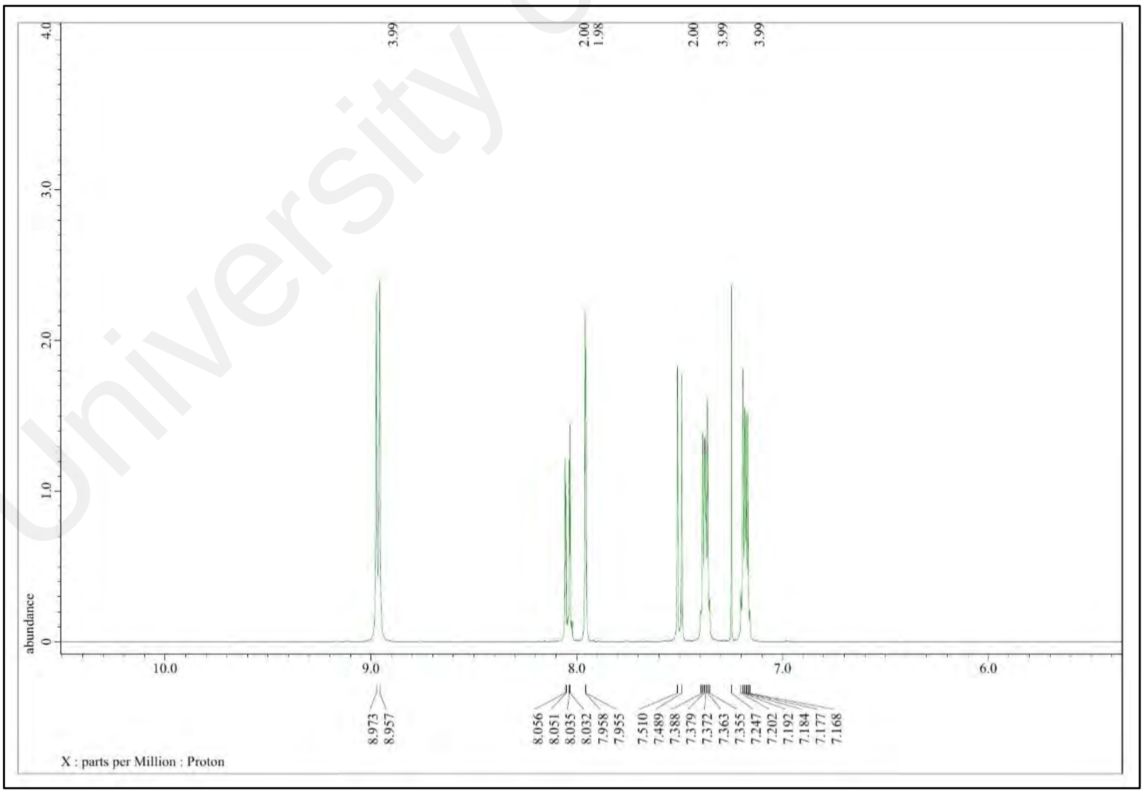

Appendix A.16: Aromatic expansion spectrum of **7a**.

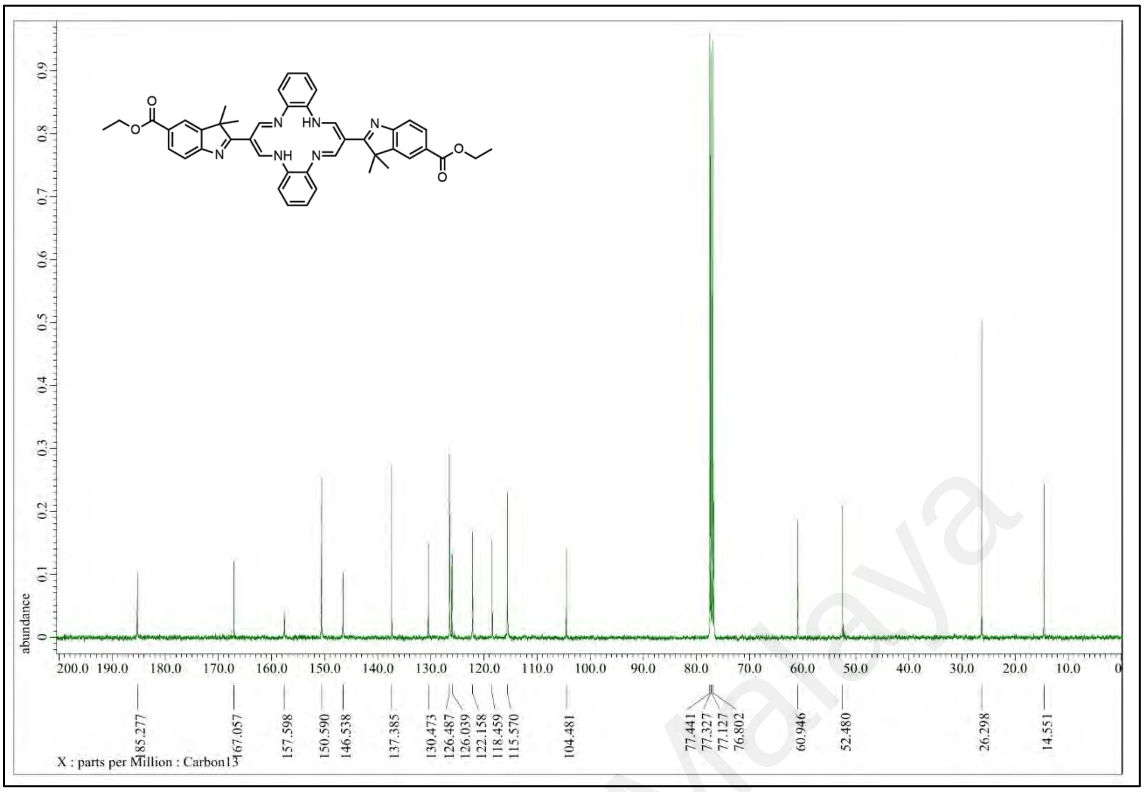

Appendix A.17: ^{13}C NMR (100 MHz, $CDCl_3$) spectrum of **7a**.

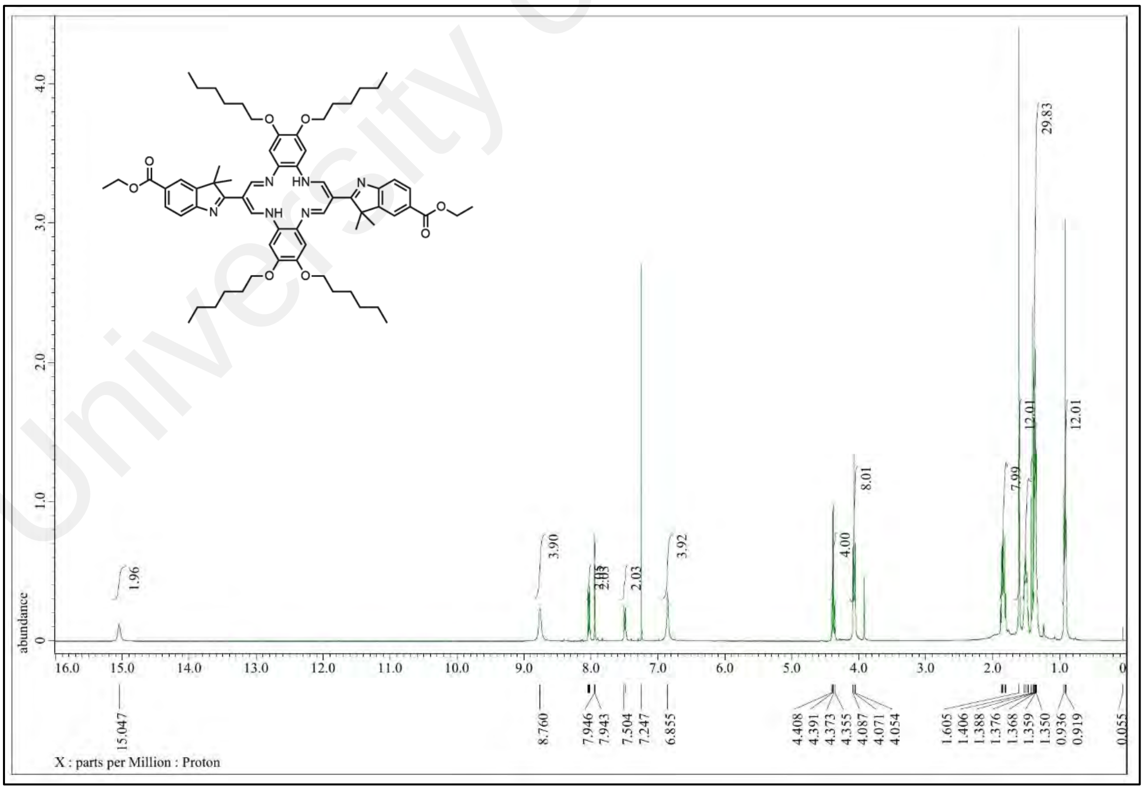

Appendix A.18: ^{1}H NMR (400 MHz, $CDCl_3$) spectrum of **7b**.

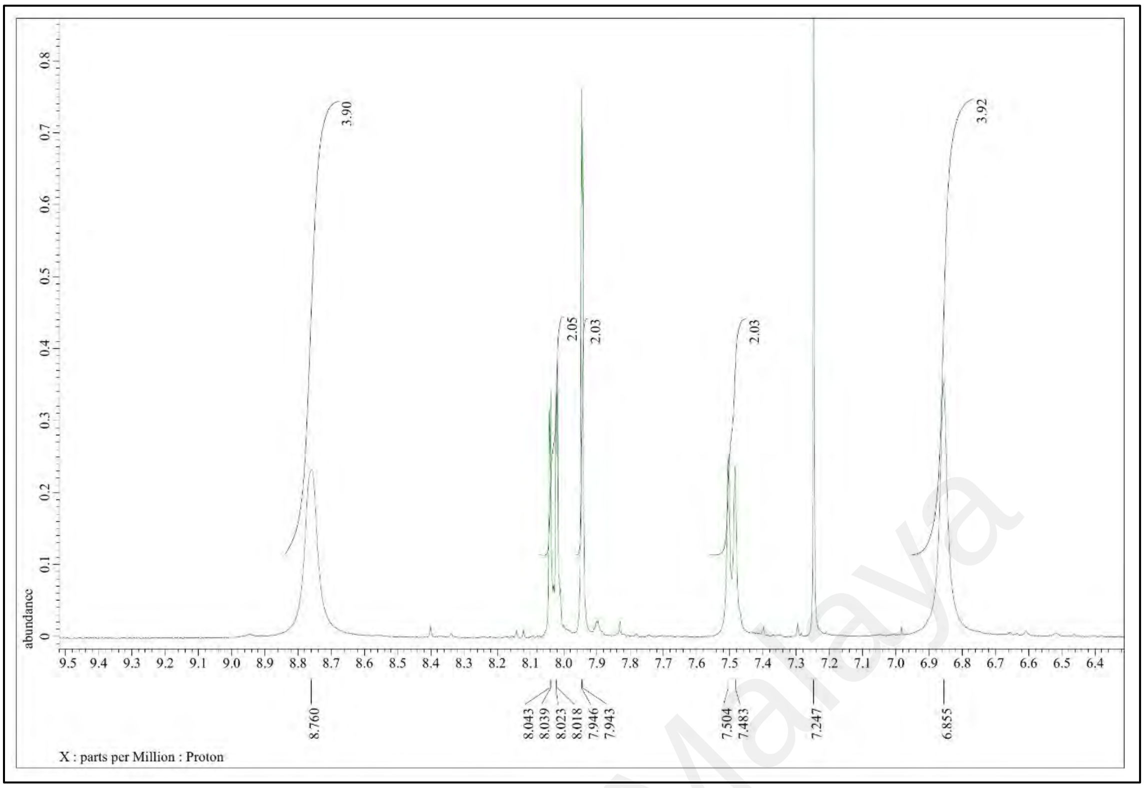

Appendix A.19: Aromatic expansion spectrum of **7b**.

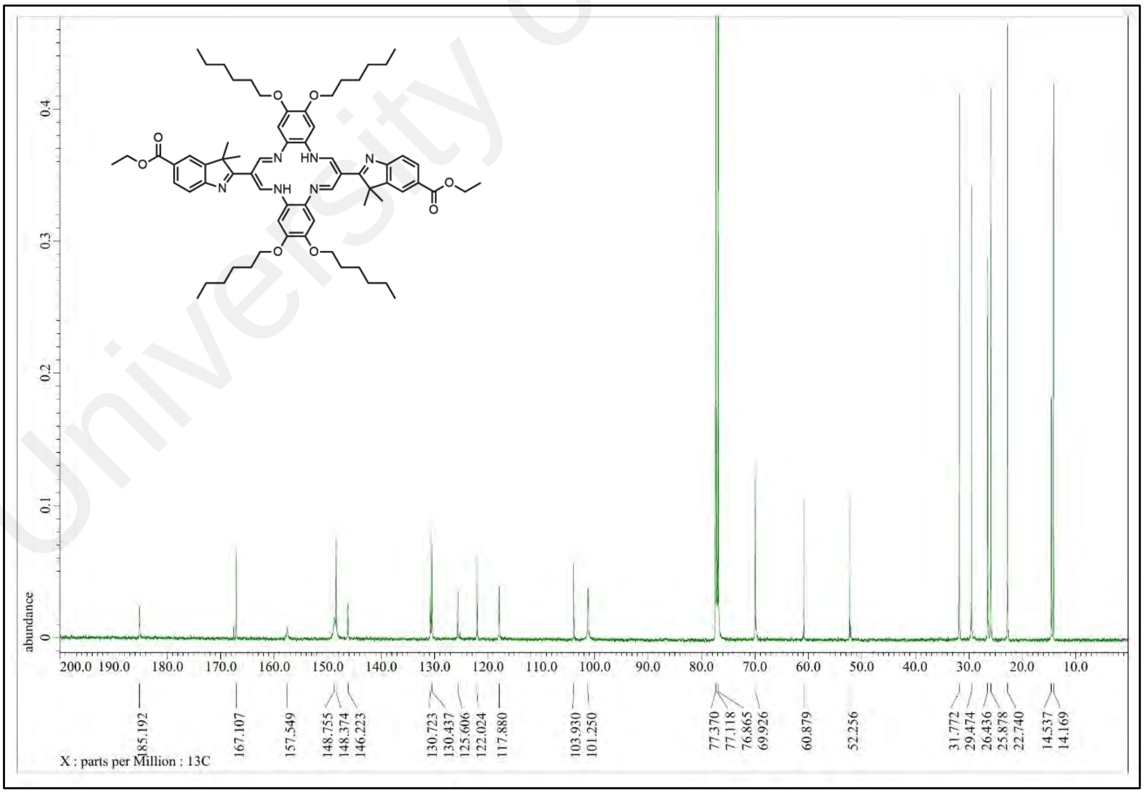

Appendix A.20: ^{13}C NMR (125 MHz, CDCl$_3$) spectrum of **7b**.

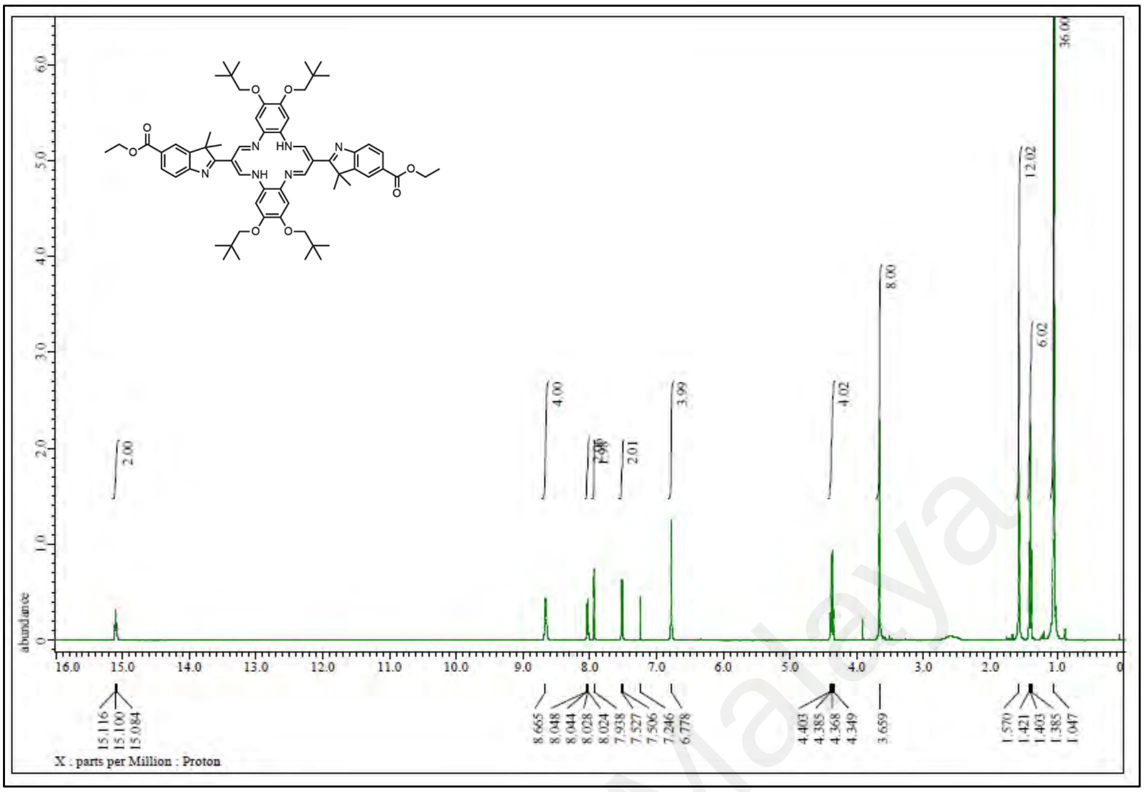

Appendix A.21: ^{1}H NMR (400 MHz, $CDCl_3$) spectrum of **7c**.

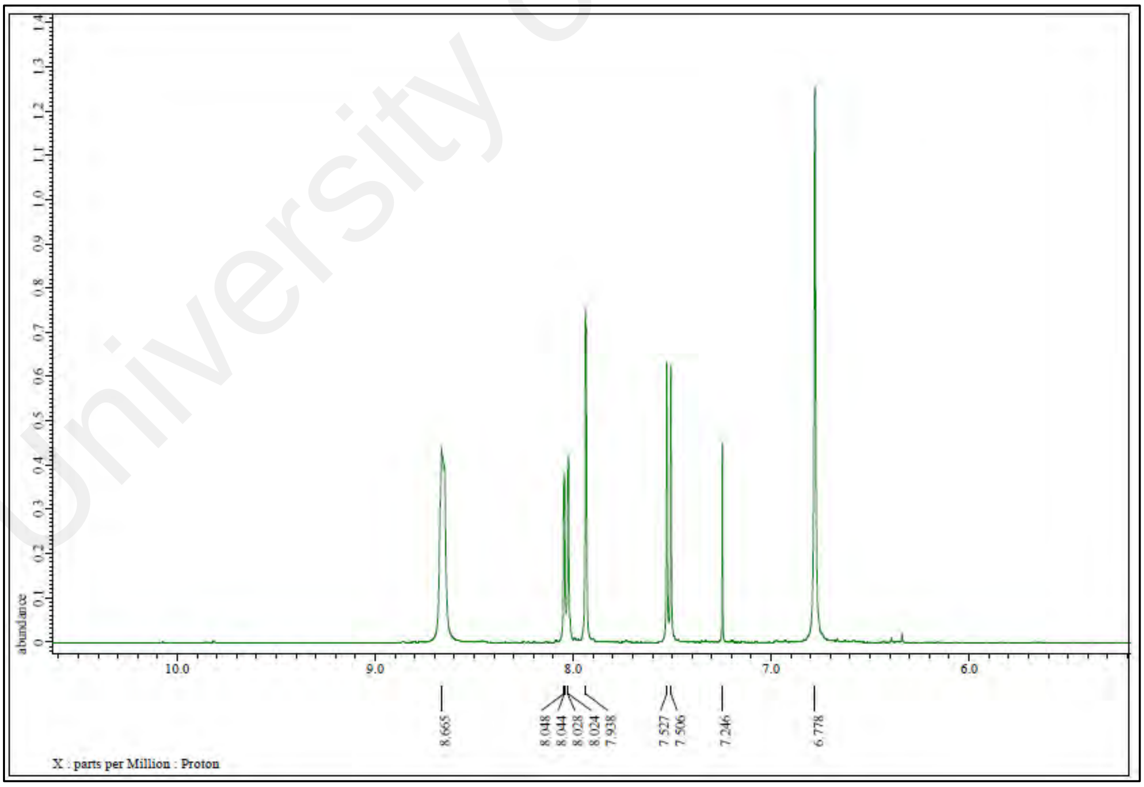

Appendix A.22: Aromatic expansion spectrum of **7c**.

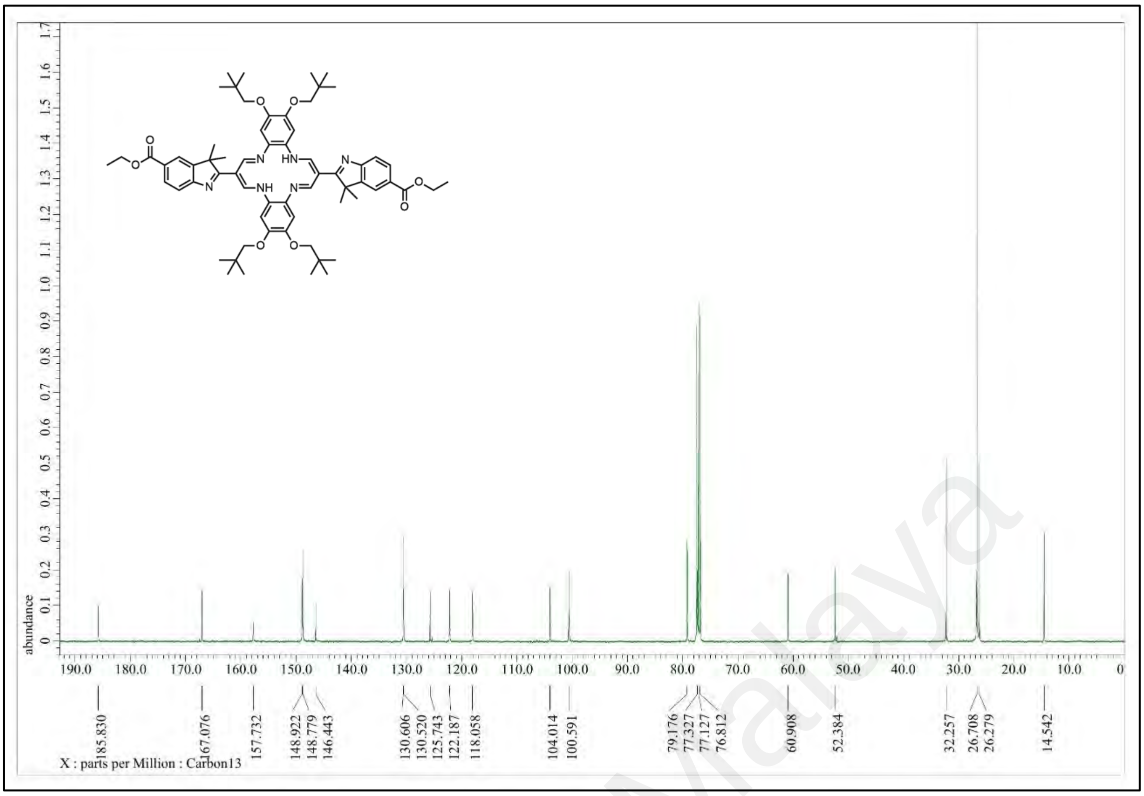

Appendix A.23: ^{13}C NMR (100 MHz, CDCl$_3$) spectrum of **7c**.

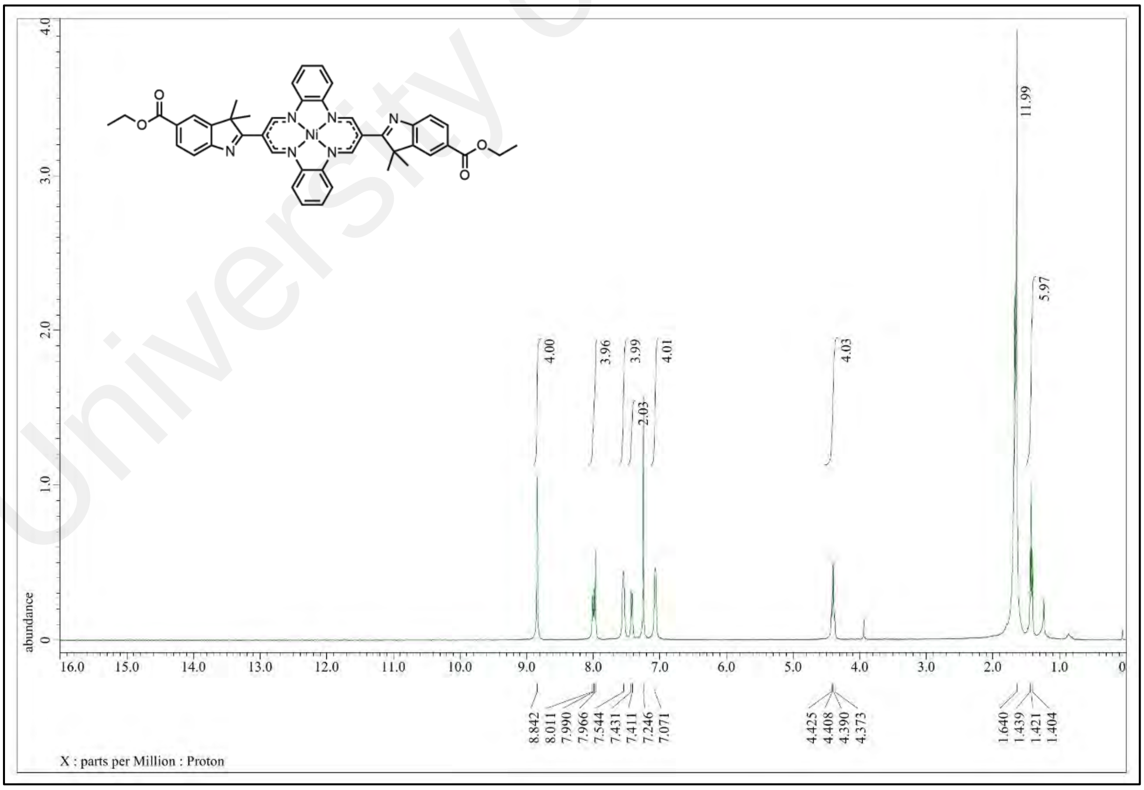

Appendix A.24: ^{1}H NMR (400 MHz, CDCl$_3$) spectrum of **8a**.

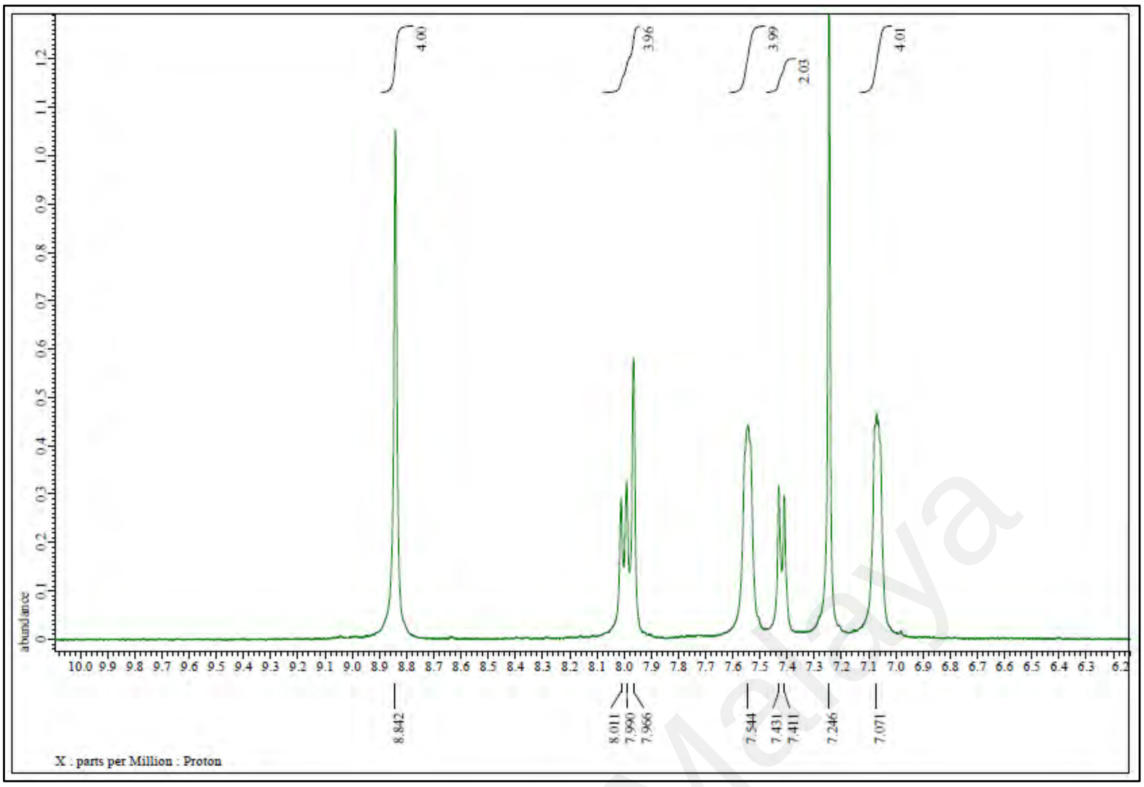

Appendix A.25: Aromatic expansion spectrum of **8a**.

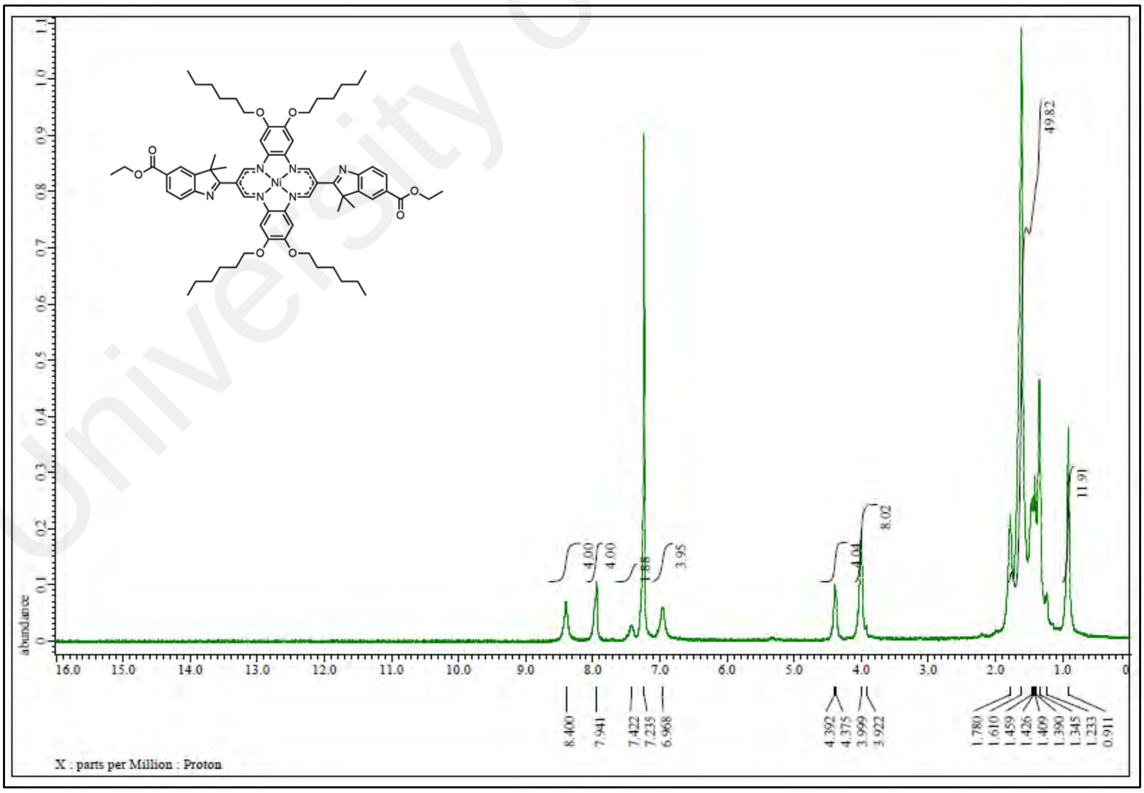

Appendix A.26: ^{1}H NMR (400 MHz, $CDCl_3$) spectrum of **8b**.

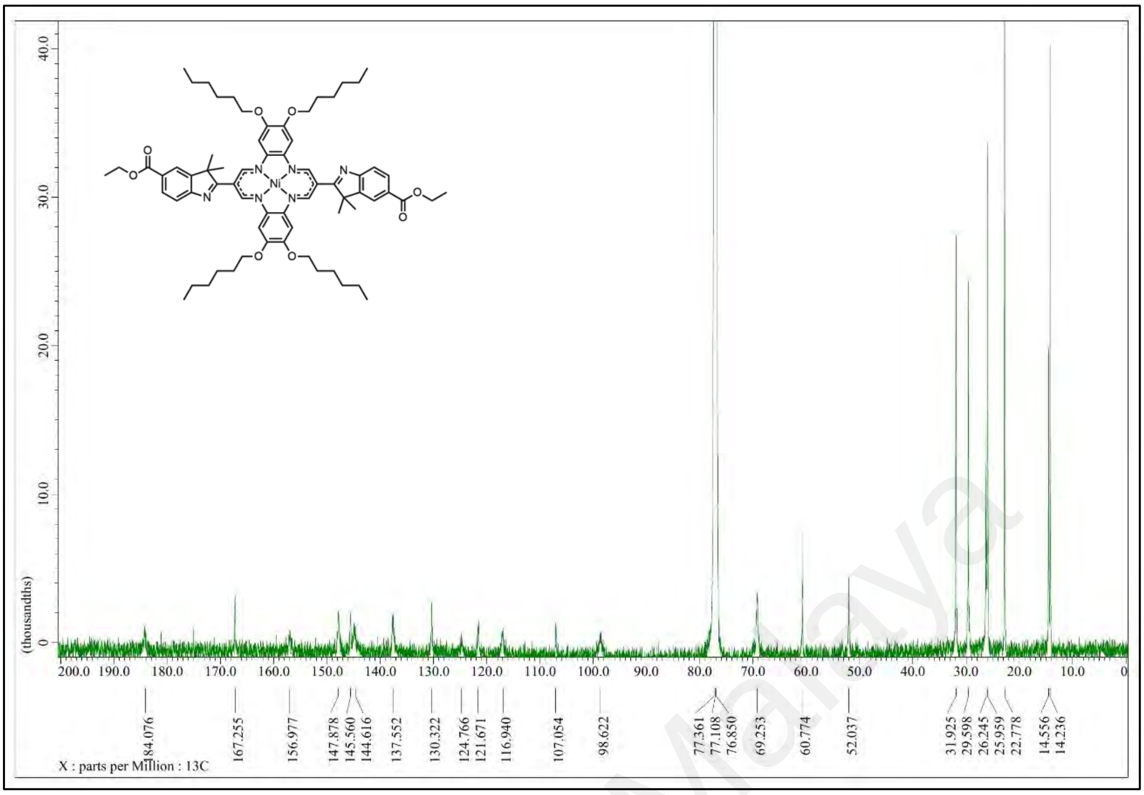

Appendix A.27: ^{13}C NMR (125 MHz, $CDCl_3$) spectrum of **8b**.

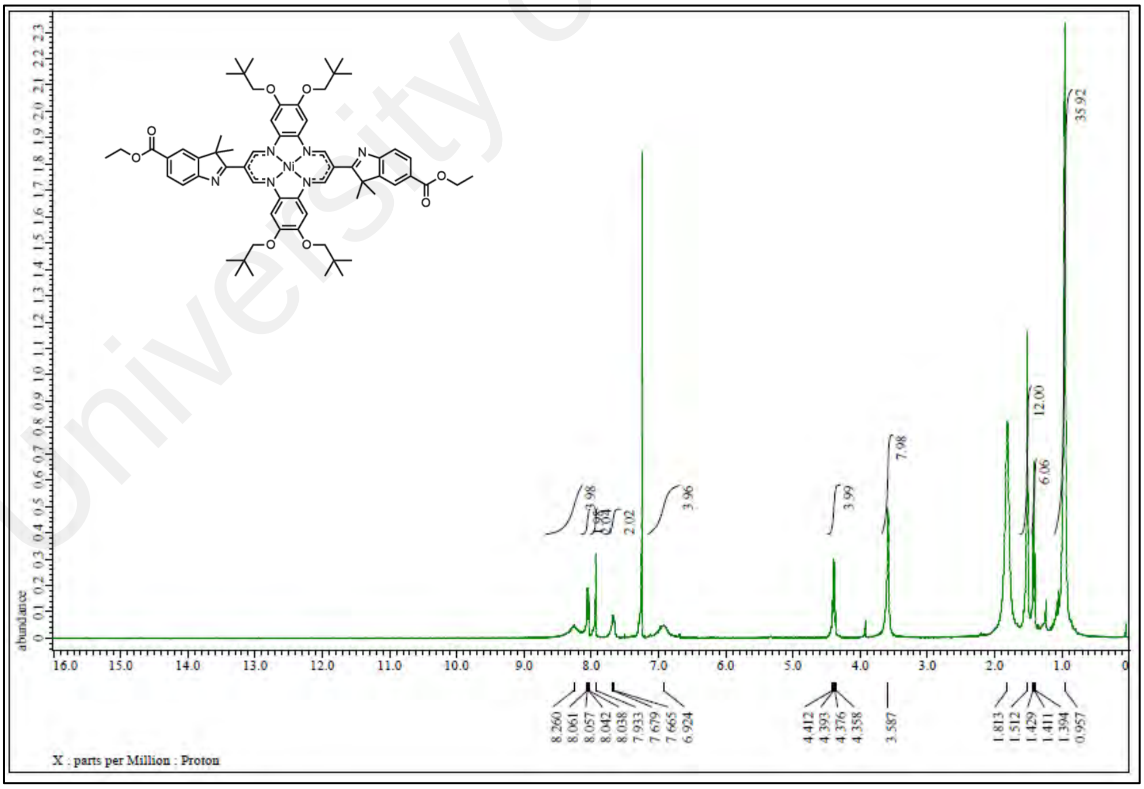

Appendix A.28: ^{1}H NMR (400 MHz, $CDCl_3$) spectrum of **8c**.

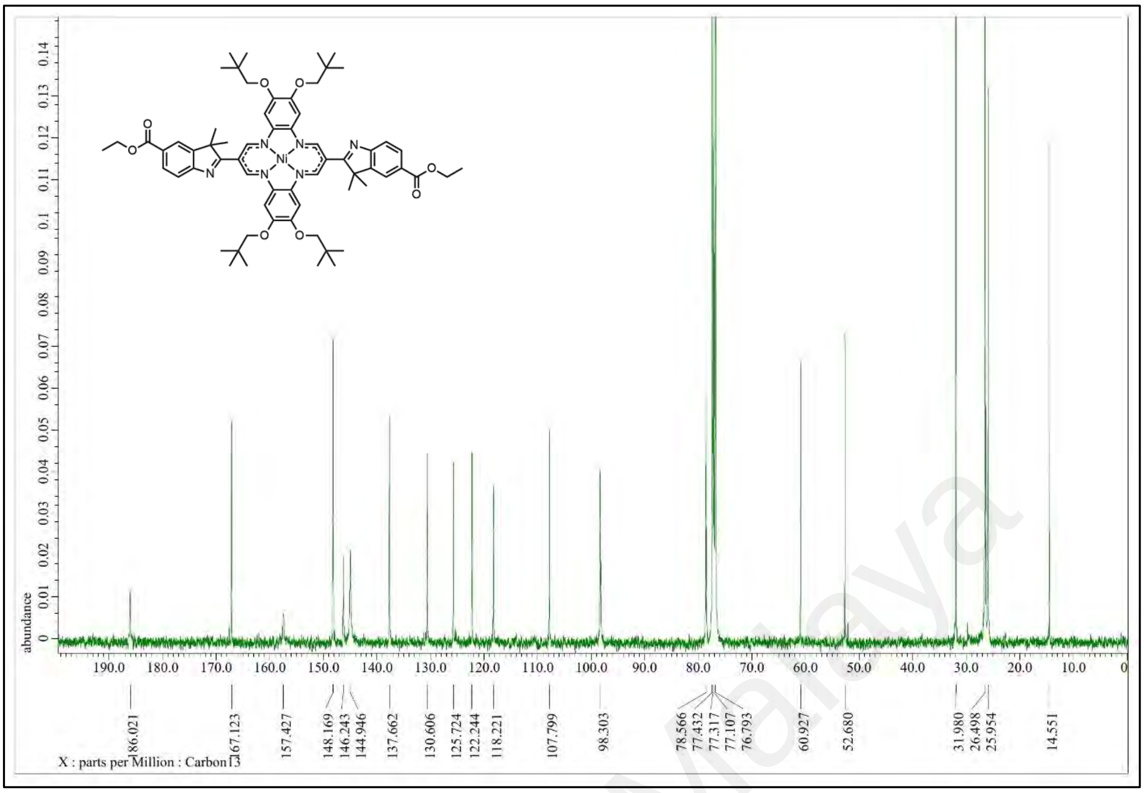

Appendix A.29: ^{13}C NMR (100 MHz, $CDCl_3$) spectrum of **8c**.

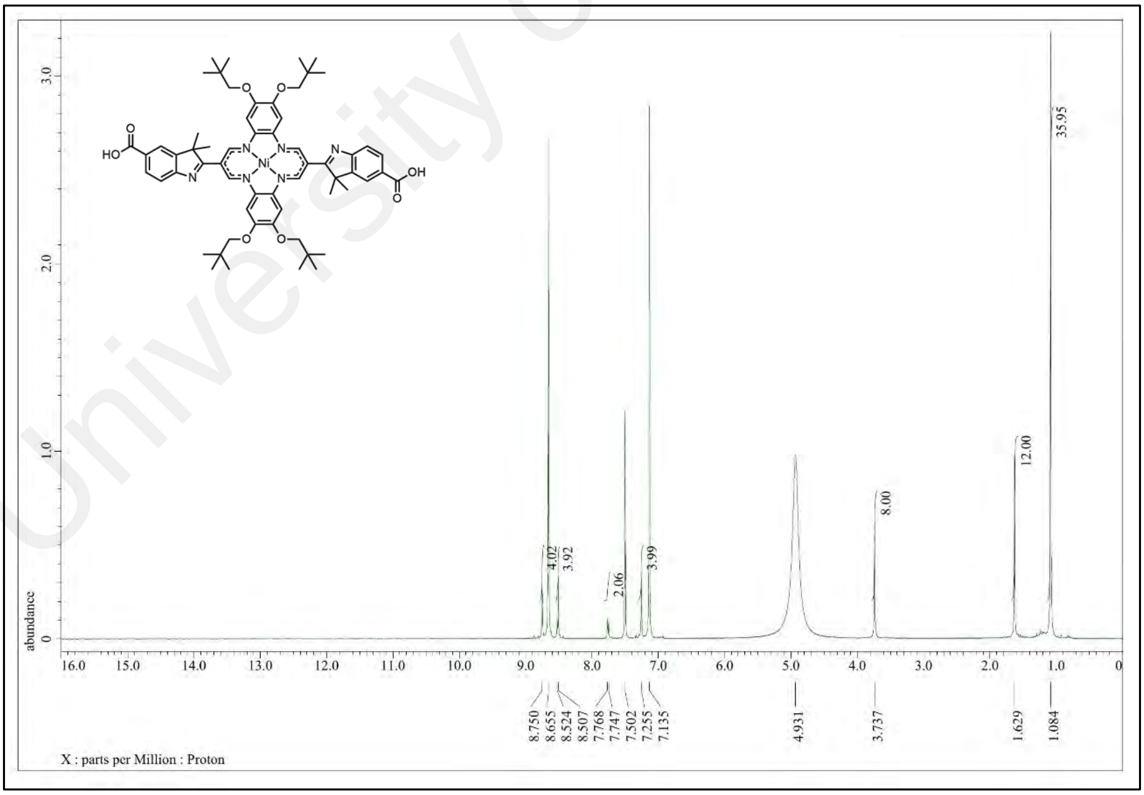

Appendix A.30: ^{1}H NMR (400 MHz, C_5D_5N) spectrum of **9c**.

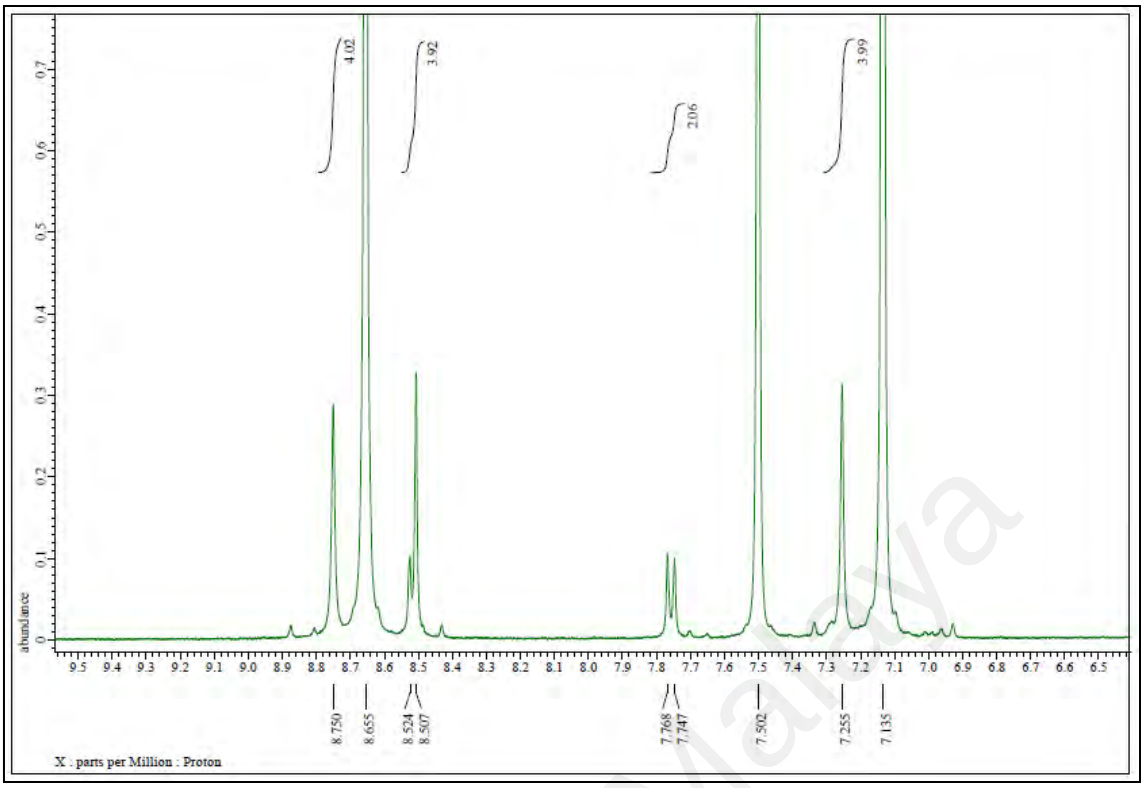

Appendix A.31: Aromatic expansion spectrum of **9c**.

APPENDIX B: IR SPECTRA

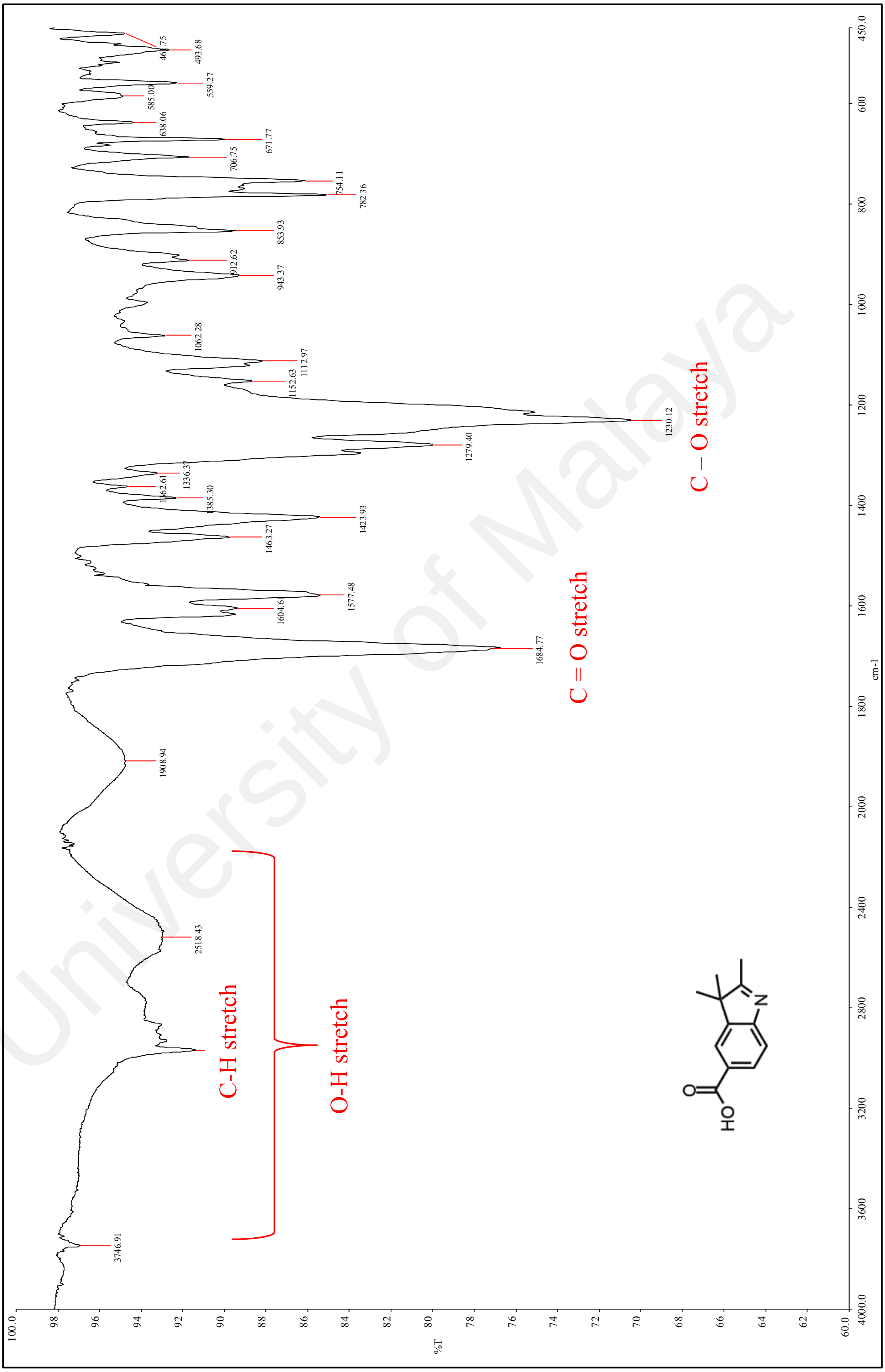

Appendix B.1: FT-IR (ATR) spectrum of **1**.

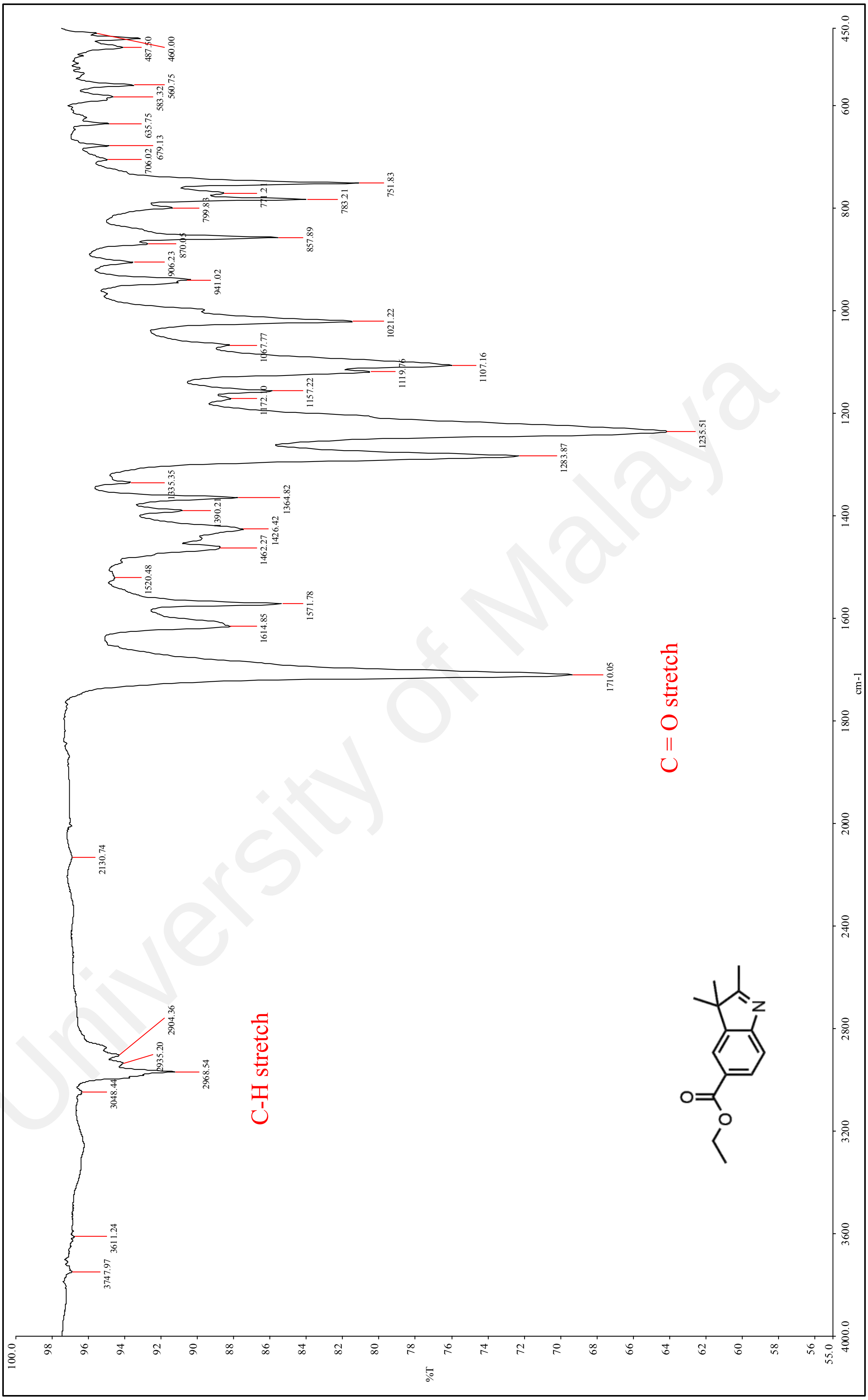

Appendix B.2: FT-IR (ATR) spectrum of **2**.

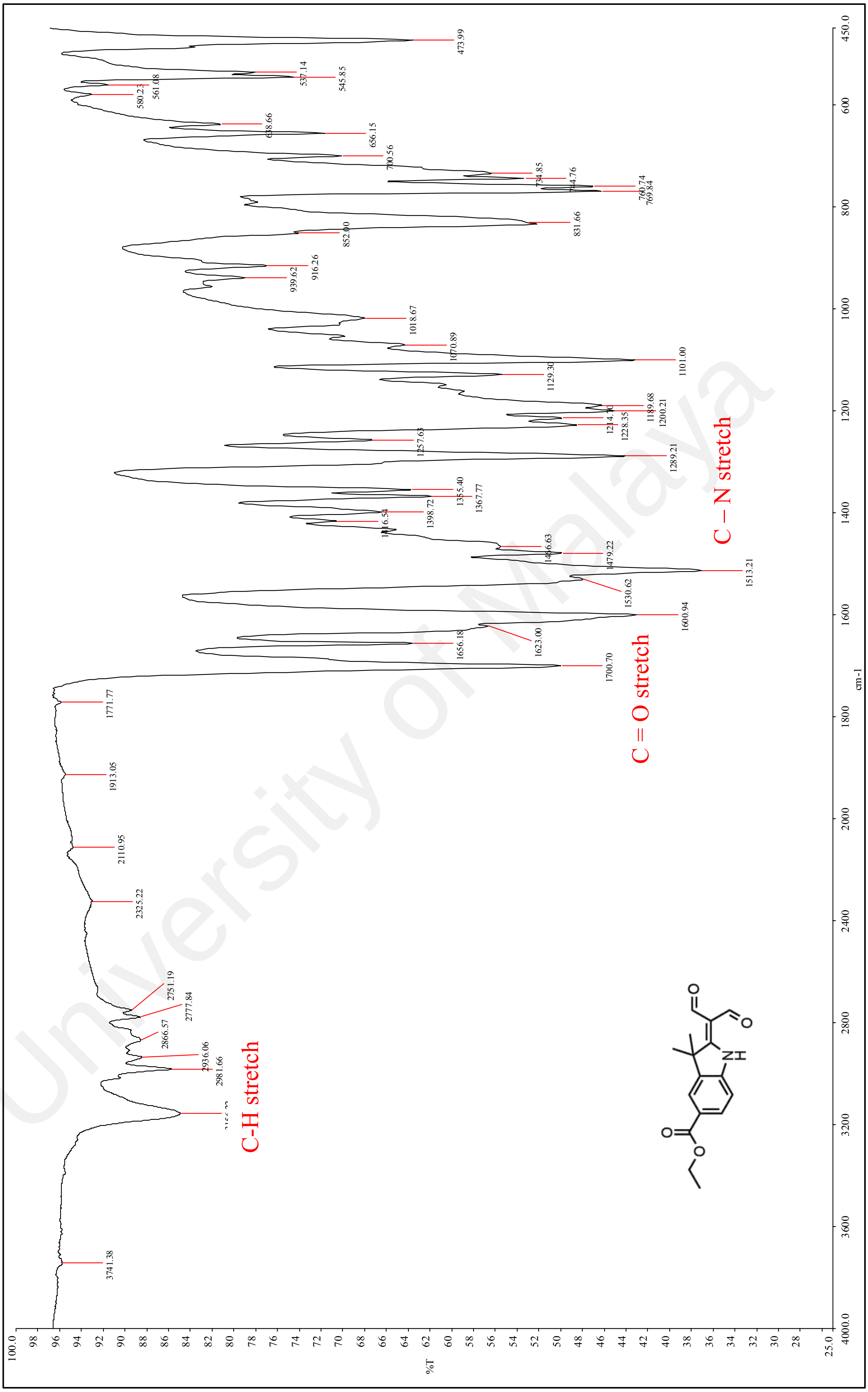

Appendix B.3: FT-IR (ATR) spectrum of **3**.

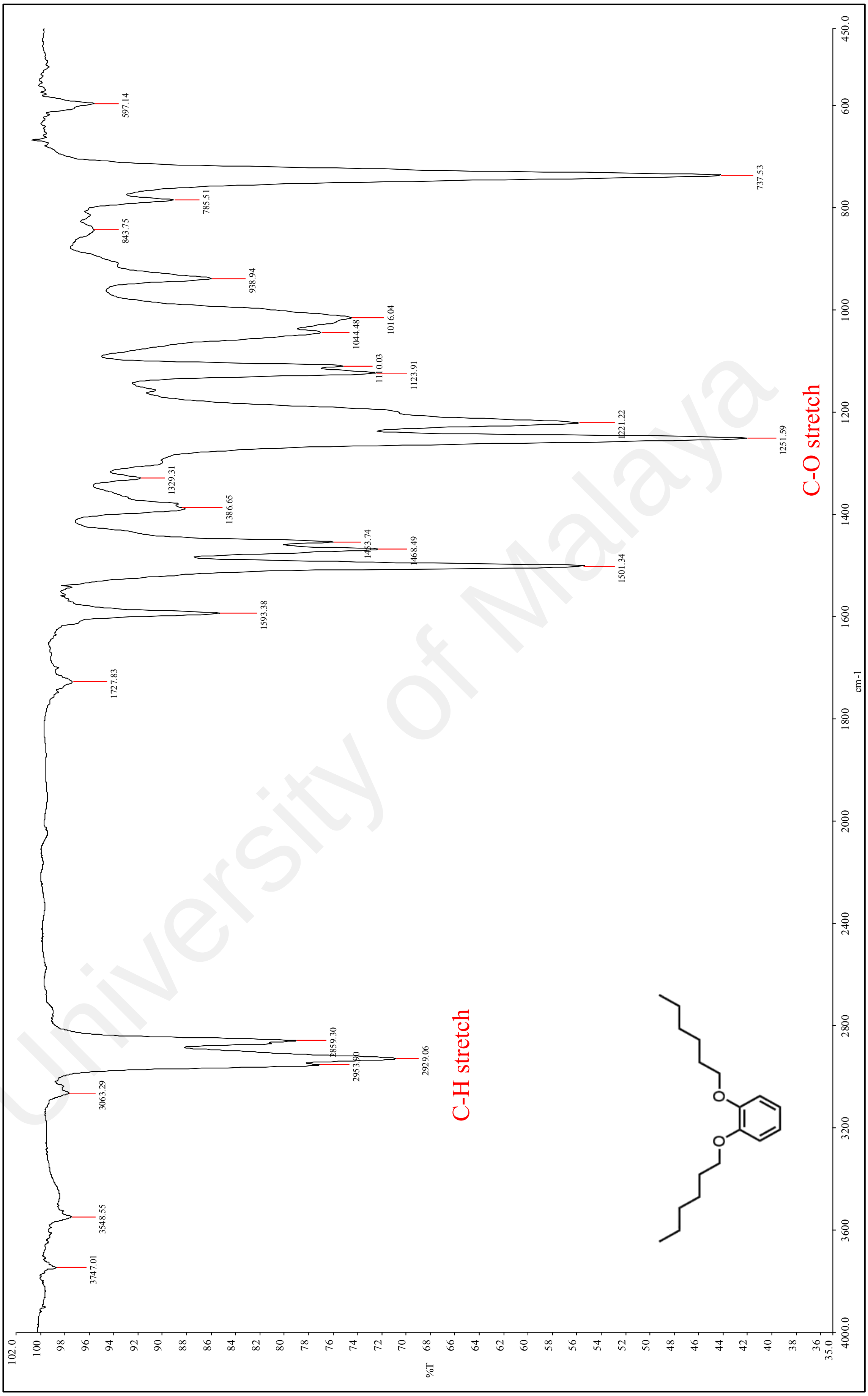

Appendix B.4: FT-IR (ATR) spectrum of **4b.**

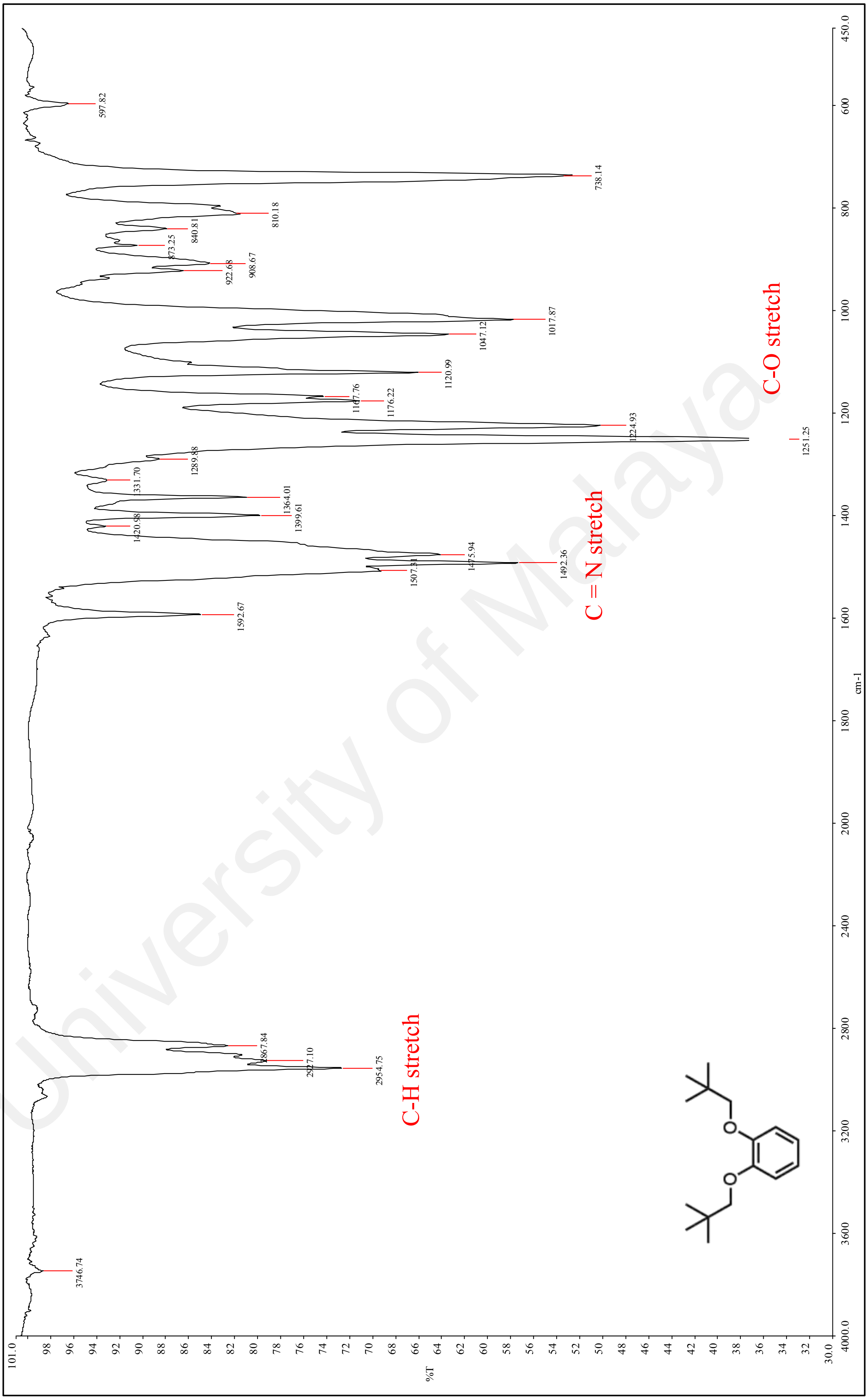

Appendix B.5: FT-IR (ATR) spectrum of **4c.**

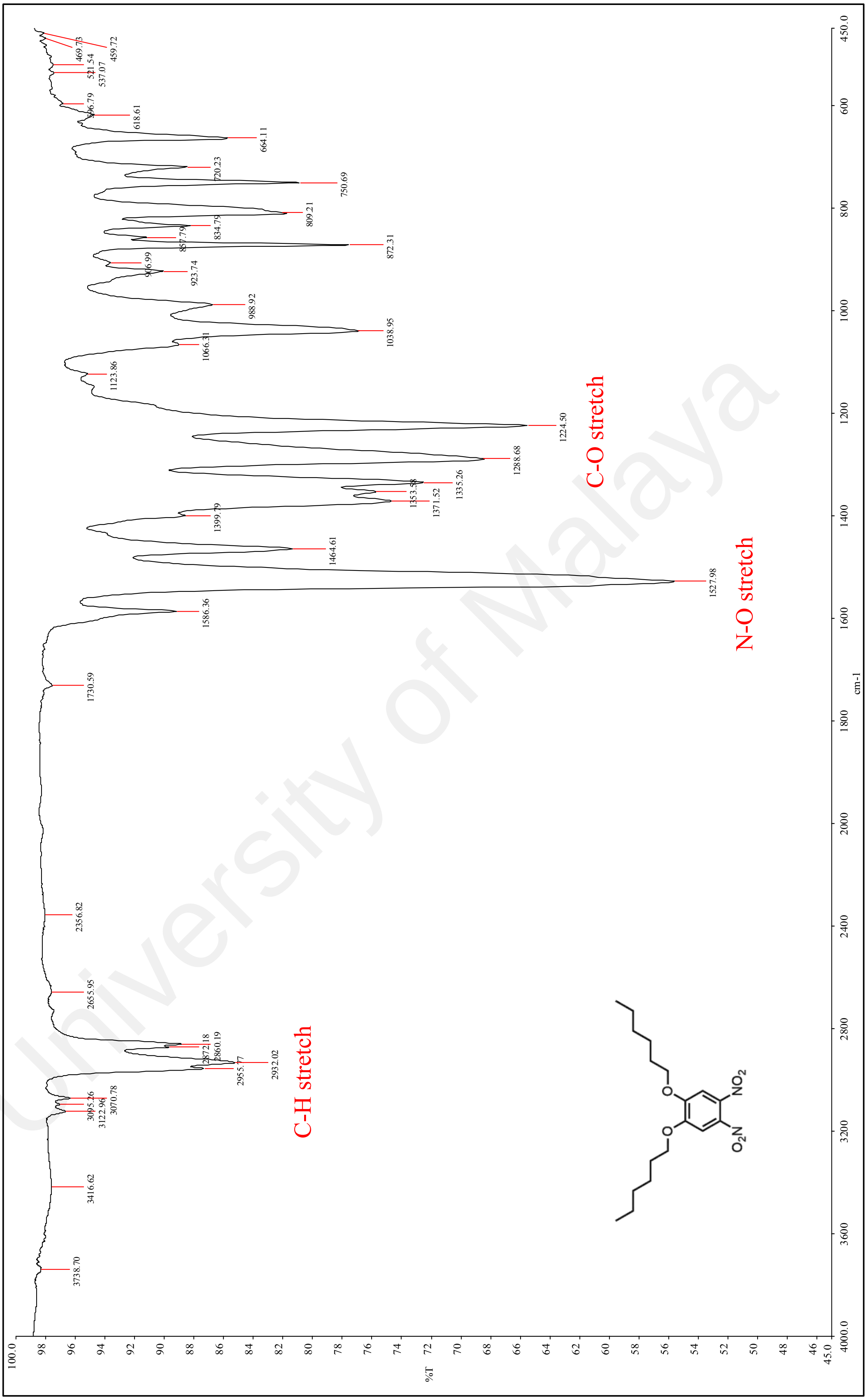

Appendix B.6: FT-IR (ATR) spectrum of **5b**.

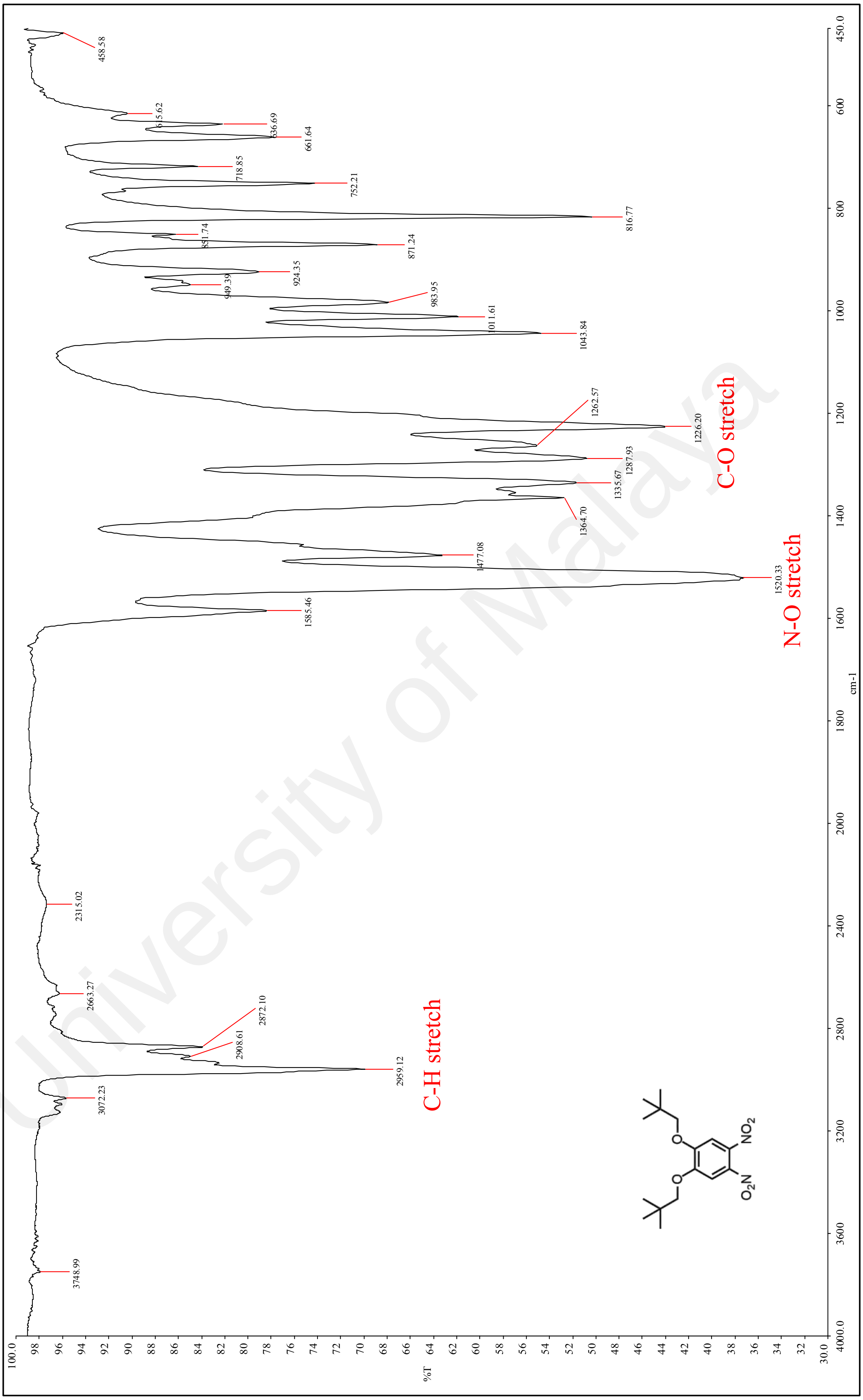

Appendix B.7: FT-IR (ATR) spectrum of **5c**.

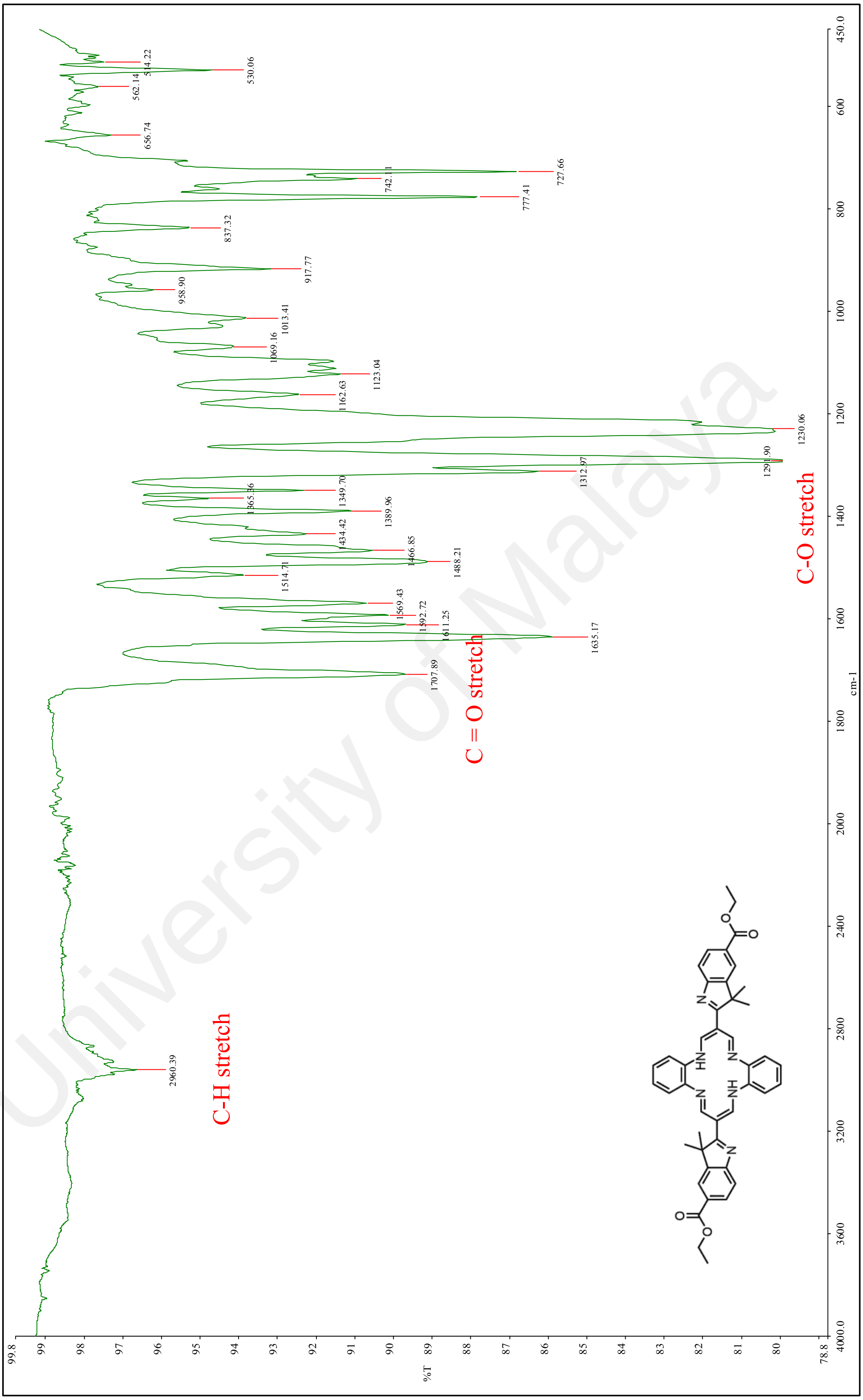

Appendix B.8: FT-IR (ATR) spectrum of **7a**.

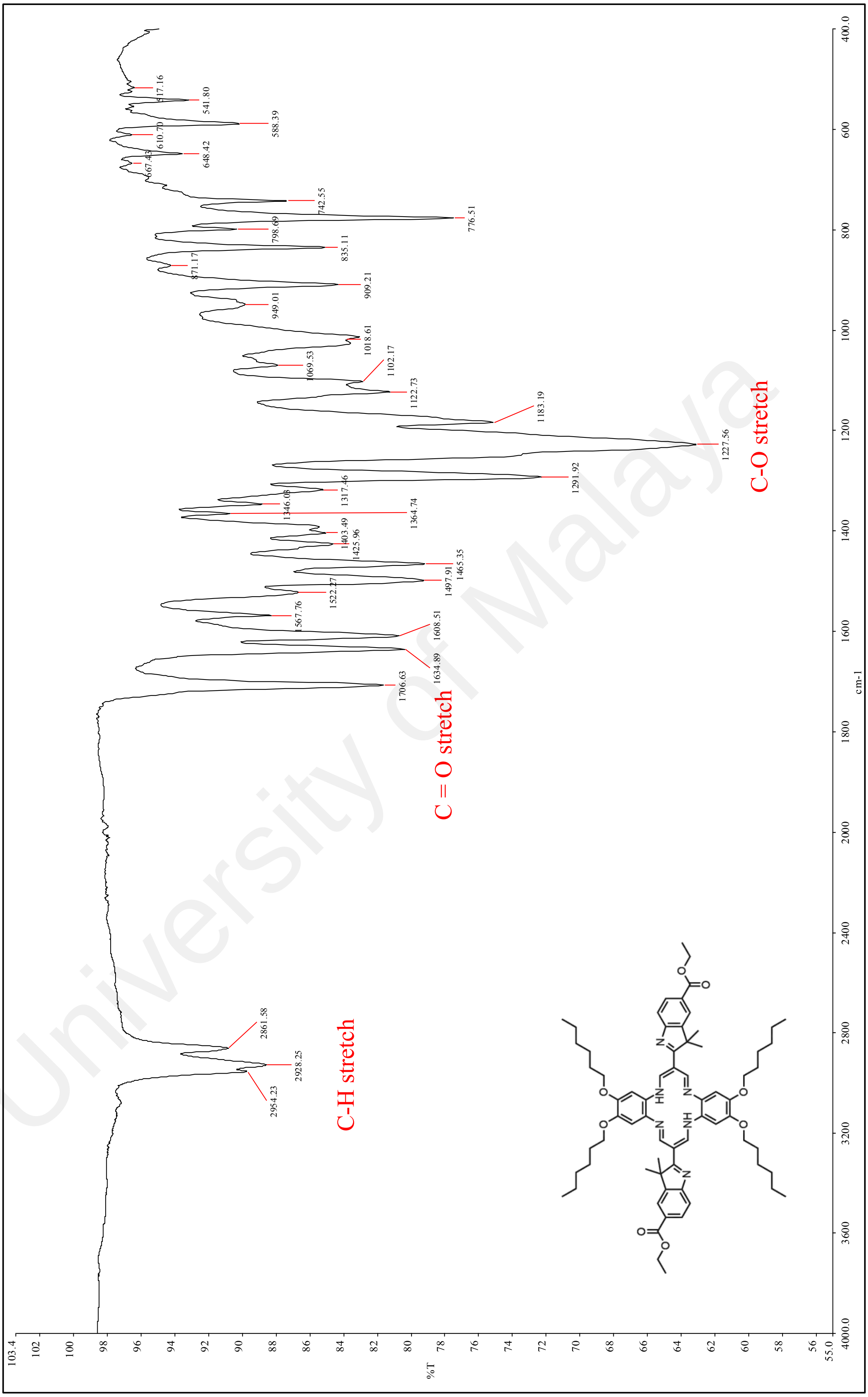

Appendix B.9: FT-IR (ATR) spectrum of **7b**.

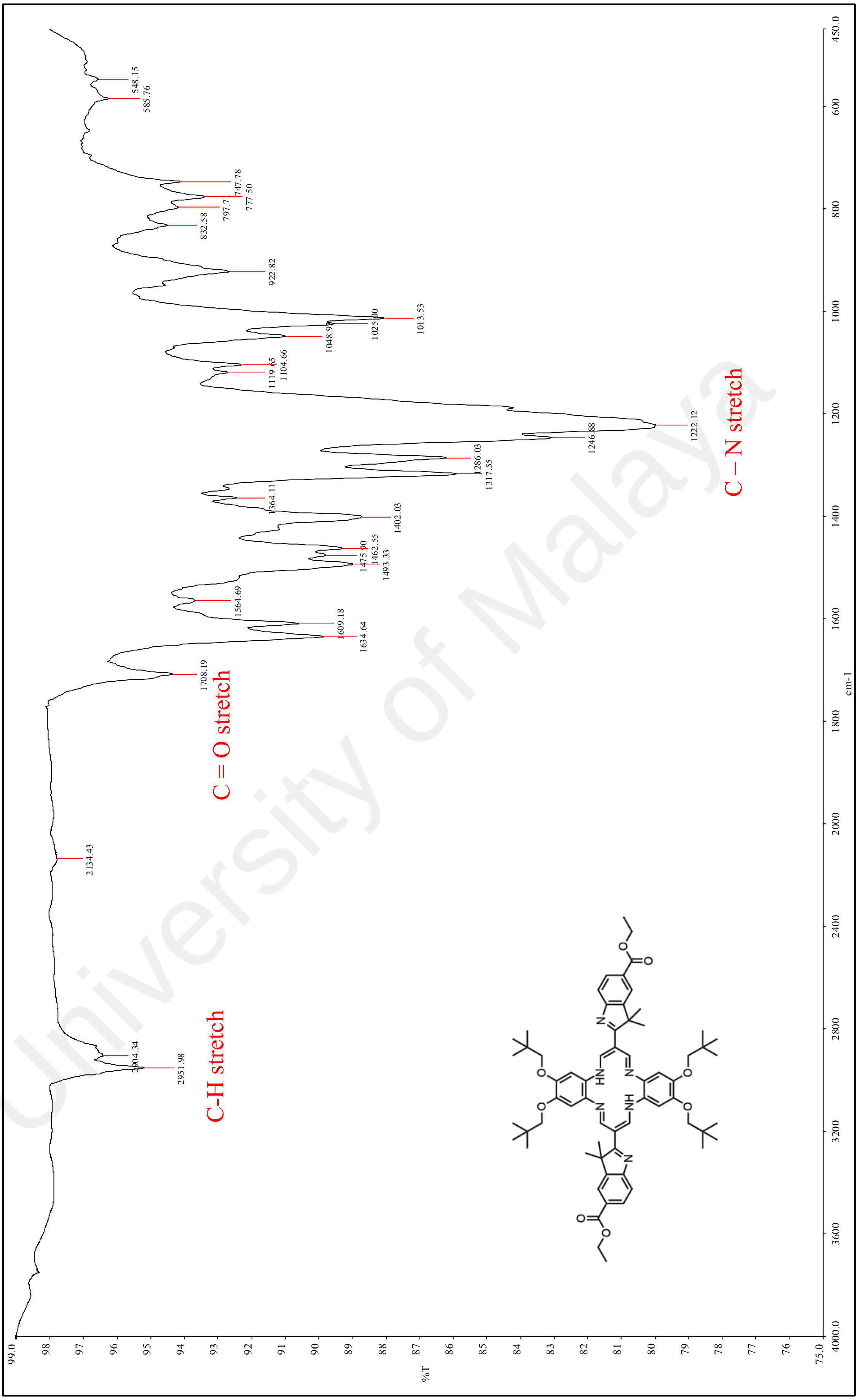

Appendix B.10: FT-IR (ATR) spectrum of **7c**.

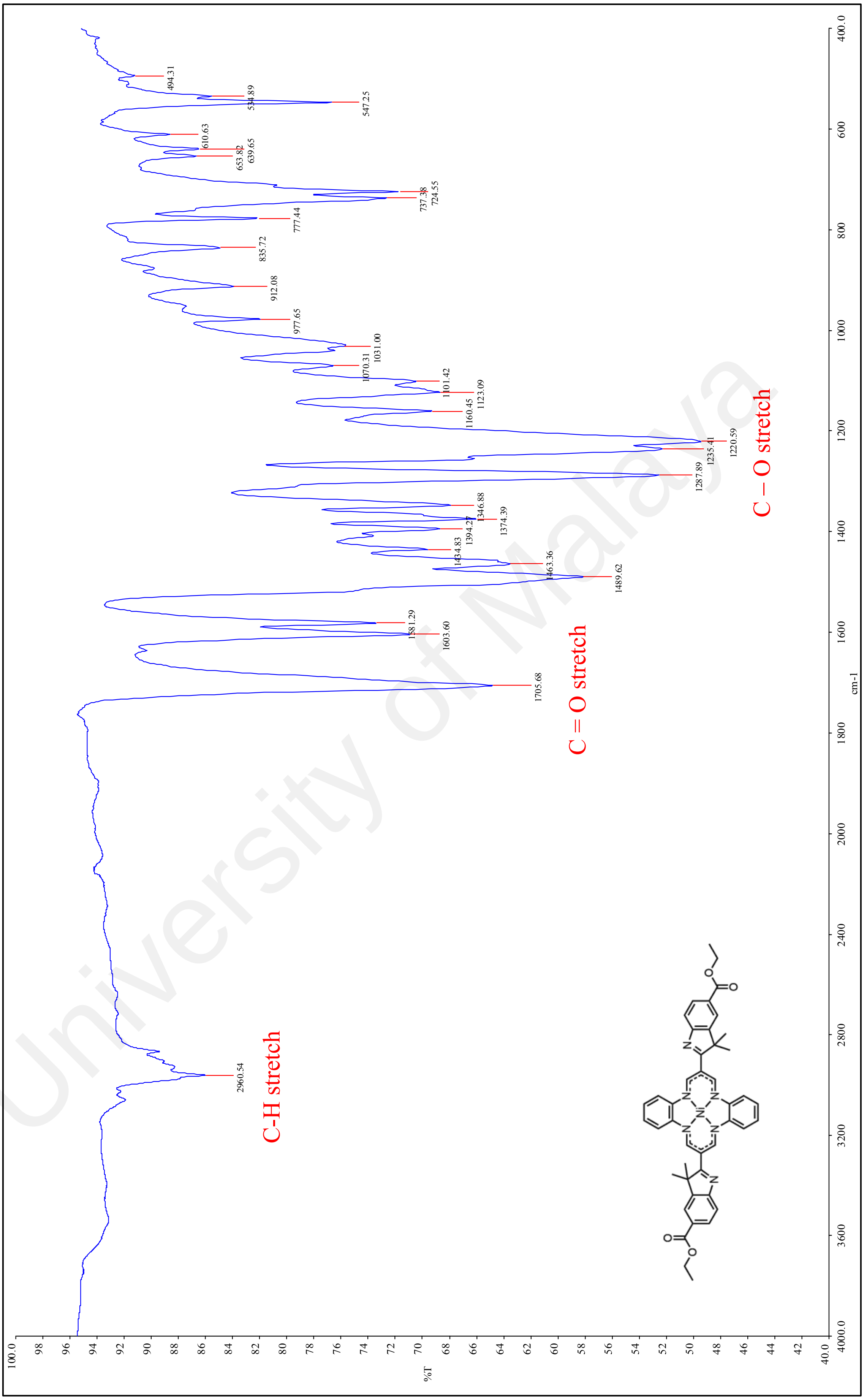

Appendix B.11: FT-IR (ATR) spectrum of **8a**.

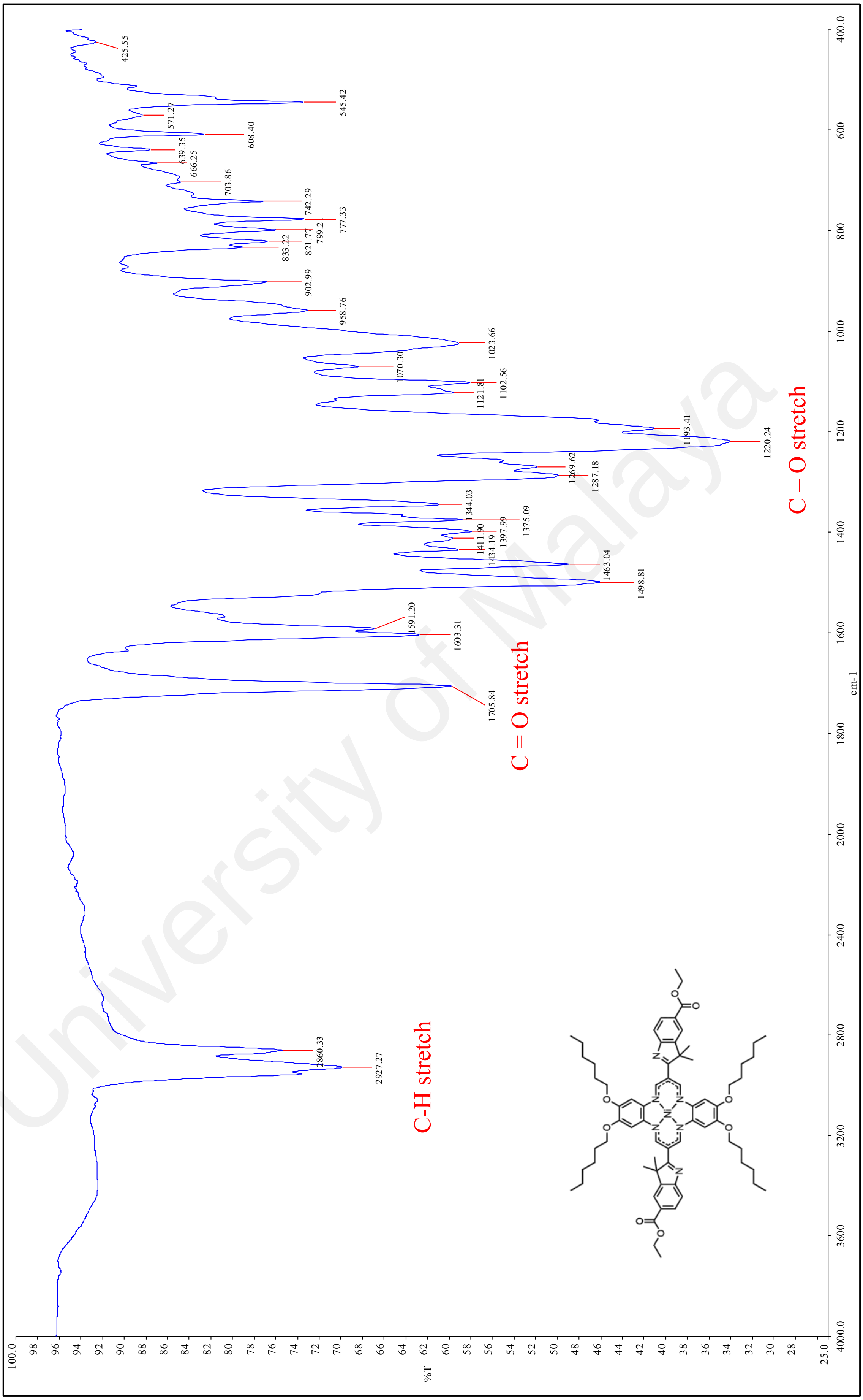

Appendix B.12: FT-IR (ATR) spectrum of **8b**.

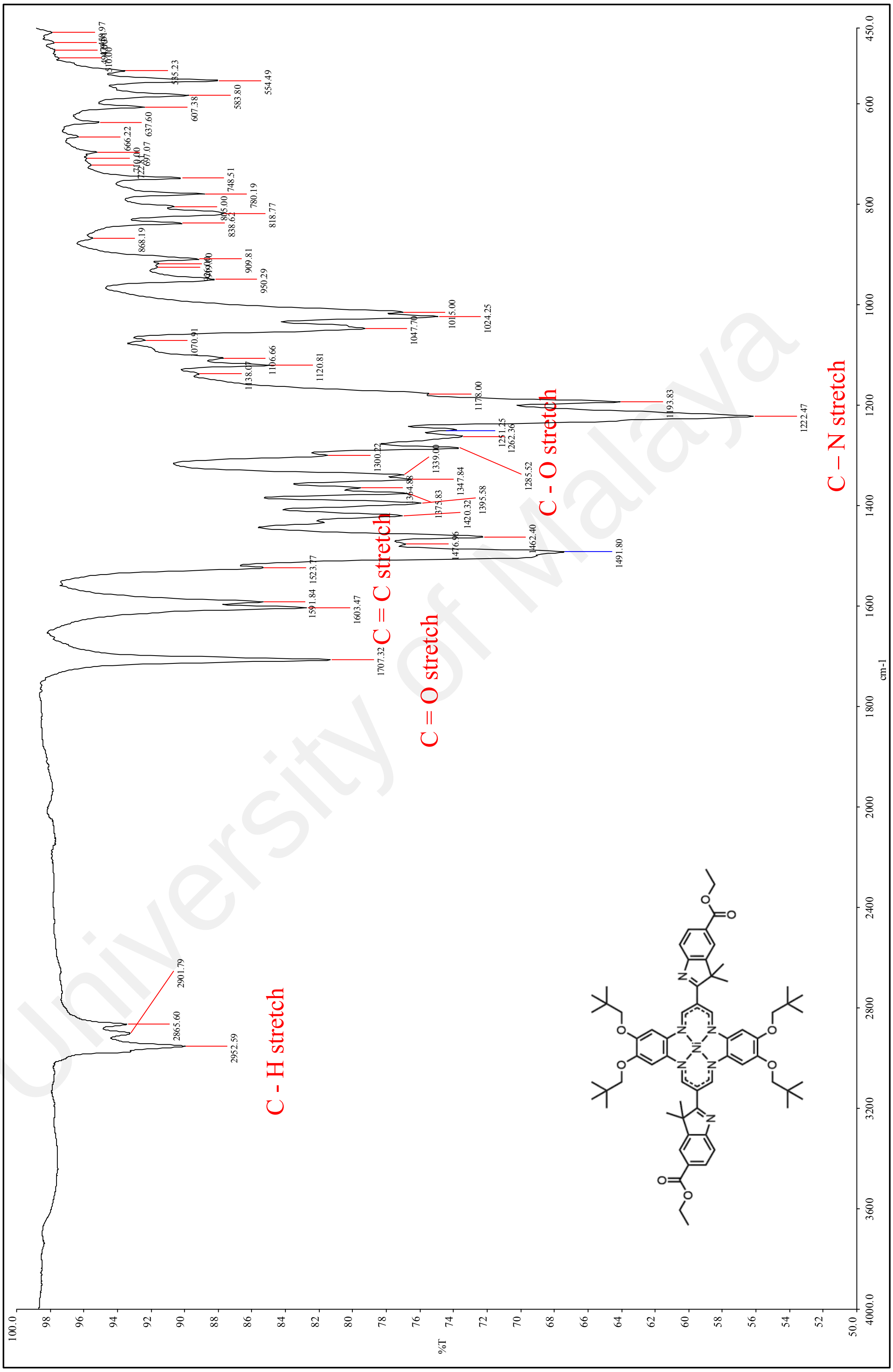

Appendix B.13: FT-IR (ATR) spectrum of **8c**.

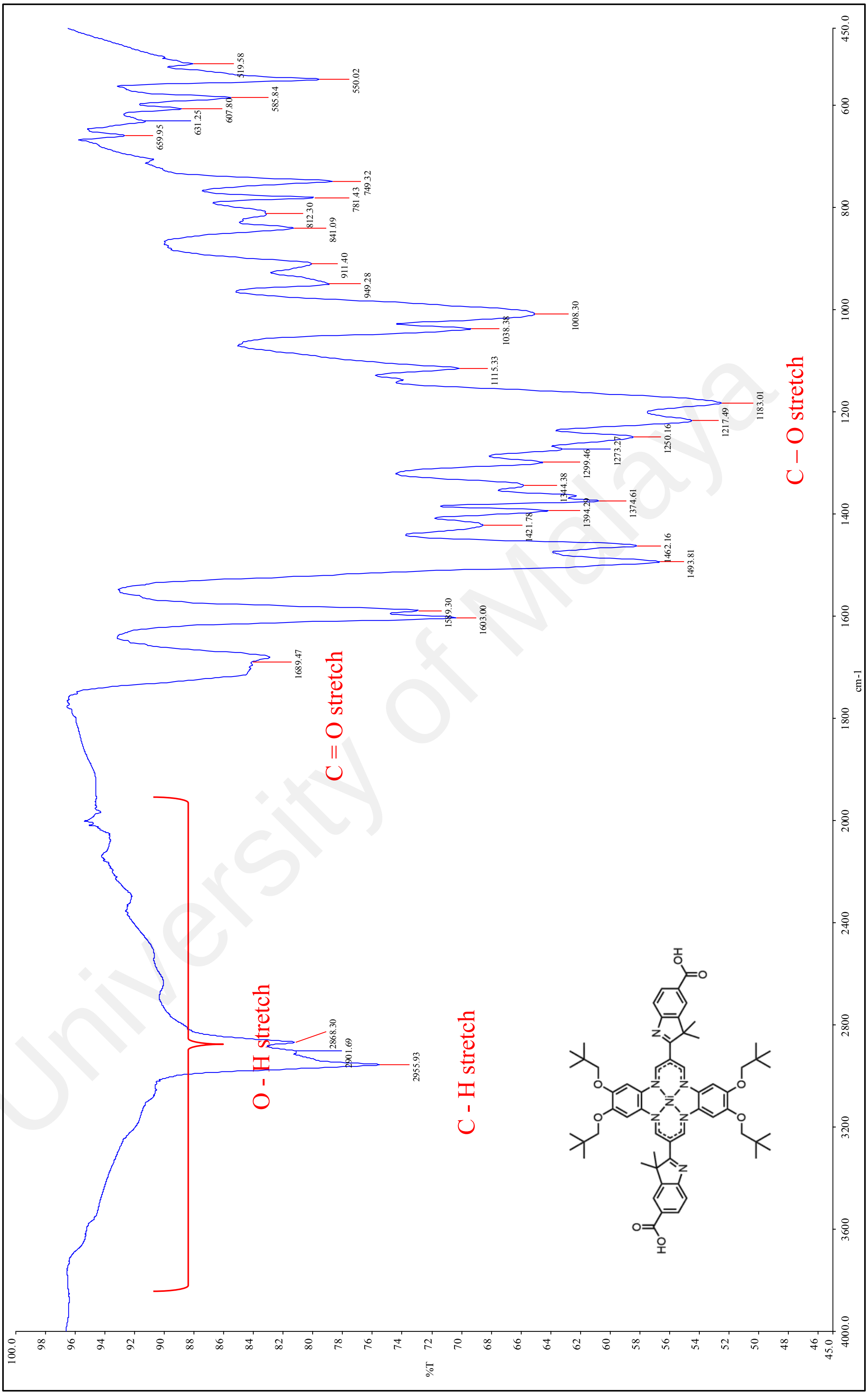

Appendix B. 14: FT-IR (ATR) spectrum of **9c**.

APPENDIX C: CARTESION COORDINATES

Cartesion coordinate of **8a**.

8a	**Coordinates (Å)**		
Element	*x*	*y*	*z*
C	0	9.341195	-0.41783
C	1.373443	9.040643	-0.40737
C	1.819322	7.72462	-0.28738
C	0.864319	6.711837	-0.1768
C	-0.51108	7.005449	-0.18706
C	-0.95347	8.308406	-0.30689
C	-0.50903	10.7311	-0.54329
O	-1.6892	11.03352	-0.56306
O	0.484986	11.64716	-0.63406
N	1.109413	5.341171	-0.04613
C	-0.04371	4.72611	0.030423
C	-1.2595	5.690937	-0.04849
C	-0.08642	3.271702	0.179488
C	-1.29507	2.55922	0.258233
C	1.164708	2.611675	0.257341
N	-1.41758	1.248092	0.378409
N	1.352463	1.316737	0.374039
C	-2.68959	0.638375	0.480756
C	-2.65671	-0.77084	0.476259
N	-1.35246	-1.31674	0.374039
C	-1.16471	-2.61168	0.257341
C	0.086418	-3.2717	0.179488
C	1.295073	-2.55922	0.258233
N	1.417583	-1.24809	0.378409
C	2.65671	0.770844	0.476259
C	2.689587	-0.63838	0.480756
C	-3.84903	-1.49856	0.580516
C	-5.0672	-0.83067	0.680548
C	-5.10256	0.565954	0.687977
C	-3.92163	1.298615	0.593834
C	3.849025	1.498557	0.580516
C	5.067202	0.830665	0.680548
C	5.102556	-0.56595	0.687977
C	3.92163	-1.29862	0.593834
C	0	-9.3412	-0.41783
C	-1.37344	-9.04064	-0.40737
C	-1.81932	-7.72462	-0.28738
C	-0.86432	-6.71184	-0.1768
C	0.511079	-7.00545	-0.18706
C	0.953468	-8.30841	-0.30689
C	0.509028	-10.7311	-0.54329
O	-0.48499	-11.6472	-0.63406
O	1.689203	-11.0335	-0.56306
N	-1.10941	-5.34117	-0.04613
C	0.043707	-4.72611	0.030423

C	1.259501	-5.69094	-0.04849
C	-2.10241	5.698059	1.248996
C	-2.13882	5.448427	-1.29833
C	2.102409	-5.69806	1.248996
C	2.138821	-5.44843	-1.29833
H	2.089082	9.850407	-0.49426
H	2.878035	7.484977	-0.27863
H	-2.00666	8.573925	-0.31853
H	-2.21162	3.133666	0.213399
H	2.026469	3.271338	0.210687
H	-2.02647	-3.27134	0.210687
H	2.211615	-3.13367	0.213399
H	-3.83855	-2.58261	0.59595
H	-3.97475	2.381376	0.624299
H	3.838554	2.582605	0.59595
H	3.974752	-2.38138	0.624299
H	-2.08908	-9.85041	-0.49426
H	-2.87804	-7.48498	-0.27863
H	2.006661	-8.57393	-0.31853
H	-2.64234	4.758582	1.404549
H	-2.84309	6.503985	1.202775
H	-1.46909	5.872223	2.124669
H	-2.68968	4.503712	-1.24902
H	-1.52955	5.437368	-2.20765
H	-2.87275	6.256198	-1.3941
H	2.642342	-4.75858	1.404549
H	2.843094	-6.50399	1.202775
H	1.469091	-5.87222	2.124669
H	2.689684	-4.50371	-1.24902
H	1.529551	-5.43737	-2.20765
H	2.872745	-6.2562	-1.3941
H	-6.05025	1.088659	0.778652
H	-5.98669	-1.40229	0.763944
H	6.050251	-1.08866	0.778652
H	5.986687	1.402291	0.763944
C	-0.06279	-13.021	-0.75758
H	0.570609	-13.2756	0.098447
H	0.548545	-13.1242	-1.66027
C	-1.31361	-13.8789	-0.81613
H	-1.93492	-13.6075	-1.67591
H	-1.03678	-14.9347	-0.91075
H	-1.91216	-13.7598	0.092913
C	0.062788	13.02103	-0.75758
H	-0.54855	13.12418	-1.66027
H	-0.57061	13.27558	0.098447
C	1.313609	13.87889	-0.81613
H	1.036777	14.9347	-0.91075
H	1.912161	13.75983	0.092913
H	1.934915	13.60748	-1.67591
Ni	0	0	0.382015

Cartesian coordinate of **8b**.

8b		**Coordinates (Å)**	
Element	*x*	*y*	*z*
C	0.045076	-9.35544	-0.63287
C	-1.3303	-9.06409	-0.60788
C	-1.78472	-7.75014	-0.49898
C	-0.83723	-6.72688	-0.41454
C	0.540422	-7.01219	-0.43918
C	0.991157	-8.31296	-0.54741
C	0.563166	-10.7428	-0.74719
O	1.757575	-11.0419	-0.7747
O	-0.4285	-11.6677	-0.81894
N	-1.09165	-5.35841	-0.30049
C	0.05932	-4.7313	-0.24835
C	1.28072	-5.69063	-0.32744
C	0.097071	-3.278	-0.12873
C	1.304644	-2.5581	-0.0672
C	-1.15693	-2.61903	-0.06485
N	1.423247	-1.24615	0.027415
N	-1.34927	-1.32372	0.027298
C	2.690473	-0.62349	0.109906
C	2.652132	0.774091	0.110529
N	1.349267	1.323723	0.027298
C	1.156932	2.619031	-0.06485
C	-0.09707	3.278004	-0.12873
C	-1.30464	2.558101	-0.0672
N	-1.42325	1.246151	0.027415
C	-2.65213	-0.77409	0.110529
C	-2.69047	0.623491	0.109906
C	3.847353	1.510699	0.197426
C	5.073754	0.862562	0.275608
C	5.11586	-0.55999	0.27363
C	3.93138	-1.28321	0.195239
C	-3.84735	-1.5107	0.197426
C	-5.07375	-0.86256	0.275608
C	-5.11586	0.55999	0.27363
C	-3.93138	1.283212	0.195239
C	-0.04508	9.355444	-0.63287
C	1.330304	9.064091	-0.60788
C	1.784718	7.750139	-0.49898
C	0.837226	6.726881	-0.41454
C	-0.54042	7.012192	-0.43918
C	-0.99116	8.312959	-0.54741
C	-0.56317	10.74276	-0.74719
O	0.4285	11.66769	-0.81894
O	-1.75758	11.04189	-0.7747
N	1.09165	5.358406	-0.30049
C	-0.05932	4.7313	-0.24835
C	-1.28072	5.690628	-0.32744
C	2.13774	-5.67648	0.960774
C	2.144855	-5.45982	-1.58966

C	-2.13774	5.676478	0.960774
C	-2.14486	5.45982	-1.58966
H	-2.04105	-9.88018	-0.67477
H	-2.84529	-7.51913	-0.47945
H	2.046359	-8.56992	-0.56936
H	2.222544	-3.13113	-0.10211
H	-2.01614	-3.28252	-0.10041
H	2.016136	3.28252	-0.10041
H	-2.22254	3.131127	-0.10211
H	3.820798	2.591403	0.213483
H	3.978518	-2.36329	0.214191
H	-3.8208	-2.5914	0.213483
H	-3.97852	2.36329	0.214191
H	2.041053	9.880176	-0.67477
H	2.845291	7.519127	-0.47945
H	-2.04636	8.569924	-0.56936
H	2.675247	-4.73277	1.097844
H	2.880358	-6.48099	0.91823
H	1.514093	-5.84026	1.845354
H	2.683208	-4.50703	-1.56265
H	1.52621	-5.47177	-2.49263
H	2.887656	-6.26045	-1.67949
H	-2.67525	4.732773	1.097844
H	-2.88036	6.480991	0.91823
H	-1.51409	5.840264	1.845354
H	-2.68321	4.507025	-1.56265
H	-1.52621	5.471773	-2.49263
H	-2.88766	6.260451	-1.67949
C	0	13.03973	-0.93219
H	-0.6242	13.28928	-0.06771
H	-0.62236	13.14497	-1.82705
C	1.247015	13.90246	-1.00153
H	1.858473	13.63728	-1.87027
H	0.965753	14.95791	-1.0873
H	1.857374	13.78076	-0.10068
C	0	-13.0397	-0.93219
H	0.622361	-13.145	-1.82705
H	0.624196	-13.2893	-0.06771
C	-1.24702	-13.9025	-1.00153
H	-0.96575	-14.9579	-1.0873
H	-1.85737	-13.7808	-0.10068
H	-1.85847	-13.6373	-1.87027
Ni	0	0	0.030735
O	-6.35643	1.107514	0.36243
O	-6.27896	-1.48357	0.366867
O	6.278961	1.483567	0.366867
O	6.35643	-1.10751	0.36243
C	-6.48243	2.527147	0.3533
H	-5.92997	2.957849	1.202301
H	-6.04847	2.934305	-0.57264
C	6.482429	-2.52715	0.3533
H	5.929969	-2.95785	1.202301

H	6.048471	-2.93431	-0.57264
C	6.312567	2.909674	0.386029
H	5.858306	3.306409	-0.53419
H	5.727787	3.285409	1.238958
C	-6.31257	-2.90967	0.386029
H	-5.85831	-3.30641	-0.53419
H	-5.72779	-3.28541	1.238958
C	-7.96462	2.863919	0.449374
H	-8.48695	2.385153	-0.38862
H	-8.366	2.416004	1.367328
C	7.964618	-2.86392	0.449374
H	8.486952	-2.38515	-0.38862
H	8.366004	-2.416	1.367328
C	-7.76898	-3.34019	0.499369
H	-8.32669	-2.91775	-0.3462
H	-8.19488	-2.89863	1.409401
C	7.768975	3.340189	0.499369
H	8.326692	2.917751	-0.3462
H	8.194877	2.898633	1.409401
C	7.926047	4.866181	0.527619
H	7.488797	5.297465	-0.38498
H	7.347963	5.279465	1.36734
C	-7.92605	-4.86618	0.527619
H	-7.4888	-5.29747	-0.38498
H	-7.34796	-5.27947	1.36734
C	-8.22448	4.376022	0.440543
H	-7.6848	4.84734	1.275321
H	-7.80887	4.815193	-0.47851
C	8.224475	-4.37602	0.440543
H	7.684802	-4.84734	1.275321
H	7.808867	-4.81519	-0.47851
C	-9.38698	-5.31962	0.649879
H	-9.96721	-4.90642	-0.18839
H	-9.82494	-4.89055	1.563202
C	-9.71427	4.730622	0.53966
H	-10.2559	4.257966	-0.29292
H	-10.1305	4.294145	1.459582
C	9.386978	5.31962	0.649879
H	9.967211	4.906418	-0.18839
H	9.824942	4.890547	1.563202
C	9.714267	-4.73062	0.53966
H	10.25592	-4.25797	-0.29292
H	10.13051	-4.29415	1.459582
C	-9.98462	6.240852	0.52762
H	-9.44294	6.71247	1.359884
H	-9.56759	6.67594	-0.39178
C	9.984618	-6.24085	0.52762
H	9.567593	-6.67594	-0.39178
H	9.442936	-6.71247	1.359884
C	-9.55201	-6.84471	0.677015
H	-9.11553	-7.2724	-0.2368
H	-8.96988	-7.25681	1.513571

C	9.552011	6.844706	0.677015
H	9.115534	7.272403	-0.2368
H	8.969879	7.256807	1.513571
C	11.47402	-6.58732	0.626266
H	11.63351	-7.67151	0.614683
H	12.03714	-6.15866	-0.21196
H	11.91187	-6.19599	1.552897
C	11.01261	7.291026	0.802588
H	11.61341	6.923384	-0.03852
H	11.09697	8.383627	0.819446
H	11.46624	6.90751	1.724903
C	-11.474	6.587318	0.626266
H	-11.6335	7.671505	0.614683
H	-12.0371	6.158655	-0.21196
H	-11.9119	6.195987	1.552897
C	-11.0126	-7.29103	0.802588
H	-11.6134	-6.92338	-0.03852
H	-11.097	-8.38363	0.819446
H	-11.4662	-6.90751	1.724903

Cartesian coordinate of **8c**.

8c	**Coordinates (Å)**		
Element	*x*	*y*	*z*
C	-0.04107	9.352236	-0.62226
C	1.334175	9.059712	-0.60323
C	1.787538	7.745747	-0.49165
C	0.839168	6.724034	-0.39859
C	-0.53832	7.010505	-0.41728
C	-0.98807	8.311291	-0.52821
C	-0.5579	10.73884	-0.73946
O	-1.73975	11.03548	-0.76278
O	0.430993	11.66271	-0.81936
N	1.092636	5.355565	-0.28073
C	-0.05857	4.730023	-0.22066
C	-1.2793	5.690048	-0.29768
C	-0.09681	3.277123	-0.09323
C	-1.30452	2.55791	-0.02759
C	1.157017	2.618199	-0.02605
N	-1.42304	1.246106	0.072326
N	1.349012	1.323439	0.074129
C	-2.68988	0.62378	0.159415
C	-2.65142	-0.77414	0.161405
N	-1.34901	-1.32344	0.074129
C	-1.15702	-2.6182	-0.02605
C	0.096806	-3.27712	-0.09323
C	1.304519	-2.55791	-0.02759
N	1.423043	-1.24611	0.072326
C	2.651418	0.774139	0.161405
C	2.689876	-0.62378	0.159415
C	-3.84567	-1.51139	0.254134

C	-5.07149	-0.86272	0.335376
C	-5.11394	0.559467	0.331703
C	-3.93033	1.283835	0.248368
C	3.845673	1.511385	0.254134
C	5.071489	0.862716	0.335376
C	5.113935	-0.55947	0.331703
C	3.930326	-1.28384	0.248368
C	0.041072	-9.35224	-0.62226
C	-1.33418	-9.05971	-0.60323
C	-1.78754	-7.74575	-0.49165
C	-0.83917	-6.72403	-0.39859
C	0.538315	-7.01051	-0.41728
C	0.988074	-8.31129	-0.52821
C	0.557904	-10.7388	-0.73946
O	-0.43099	-11.6627	-0.81936
O	1.739753	-11.0355	-0.76278
N	-1.09264	-5.35557	-0.28073
C	0.058574	-4.73002	-0.22066
C	1.279303	-5.69005	-0.29768
C	-2.13094	5.679934	0.994207
C	-2.1494	5.455896	-1.55525
C	2.130938	-5.67993	0.994207
C	2.149399	-5.4559	-1.55525
H	2.045365	9.874778	-0.67677
H	2.84789	7.513492	-0.47662
H	-2.04302	8.569628	-0.54578
H	-2.22264	3.130644	-0.06403
H	2.016524	3.281248	-0.06569
H	-2.01652	-3.28125	-0.06569
H	2.222638	-3.13064	-0.06403
H	-3.81851	-2.59195	0.272937
H	-3.97785	2.363838	0.266061
H	3.818511	2.591947	0.272937
H	3.977845	-2.36384	0.266061
H	-2.04537	-9.87478	-0.67677
H	-2.84789	-7.51349	-0.47662
H	2.043023	-8.56963	-0.54578
H	-2.66667	4.736028	1.136734
H	-2.87473	6.483375	0.951807
H	-1.50376	5.847644	1.875523
H	-2.69392	4.506844	-1.51947
H	-1.53418	5.457856	-2.46063
H	-2.88739	6.260577	-1.6476
H	2.66667	-4.73603	1.136734
H	2.874727	-6.48338	0.951807
H	1.503755	-5.84764	1.875523
H	2.693919	-4.50684	-1.51947
H	1.534182	-5.45786	-2.46063
H	2.88739	-6.26058	-1.6476
C	0	-13.0339	-0.93516
H	0.63026	-13.282	-0.0748
H	0.616961	-13.1373	-1.83402

C	-1.2453	-13.8996	-0.99754
H	-1.8635	-13.6342	-1.86143
H	-0.96187	-14.9541	-1.08754
H	-1.8497	-13.7815	-0.0922
C	0	13.03389	-0.93516
H	-0.61696	13.13735	-1.83402
H	-0.63026	13.28197	-0.0748
C	1.245301	13.89961	-0.99754
H	0.961867	14.95411	-1.08754
H	1.849698	13.78145	-0.0922
H	1.863497	13.6342	-1.86143
Ni	0	0	0.076974
O	6.355451	-1.10506	0.423387
O	6.277104	1.482477	0.432721
O	-6.2771	-1.48248	0.432721
O	-6.35545	1.105064	0.423387
C	6.491358	-2.52366	0.429725
H	5.933367	-2.94487	1.279875
H	6.068159	-2.93879	-0.49774
C	-6.49136	2.523656	0.429725
H	-5.93337	2.944868	1.279875
H	-6.06816	2.938793	-0.49774
C	-6.31848	-2.90812	0.463632
H	-5.86713	-3.3105	-0.45561
H	-5.73408	-3.27487	1.320742
C	6.318478	2.908116	0.463632
H	5.86713	3.310497	-0.45561
H	5.734082	3.274872	1.320742
C	7.981191	-2.88539	0.542948
C	-7.98119	2.885394	0.542948
C	7.780561	3.367051	0.582713
C	-7.78056	-3.36705	0.582713
C	-8.08543	4.422309	0.540341
H	-7.54191	4.864703	1.384634
H	-7.68252	4.852231	-0.38529
H	-9.13314	4.733524	0.621089
C	-8.75182	2.307163	-0.65885
H	-8.36912	2.709441	-1.60538
H	-8.66282	1.217181	-0.69407
H	-9.81568	2.56366	-0.59271
C	-8.55499	2.325363	1.85816
H	-8.46018	1.235888	1.895378
H	-8.03012	2.741309	2.727531
H	-9.61654	2.581859	1.954476
C	-8.39551	-2.82016	1.884699
H	-8.37789	-1.72611	1.897765
H	-9.43657	-3.14875	1.986123
H	-7.84444	-3.17859	2.763365
C	-8.58593	-2.86937	-0.63219
H	-9.62976	-3.19764	-0.56227
H	-8.57303	-1.7767	-0.69079
H	-8.17321	-3.26394	-1.56926

C	-7.77853	-4.90734	0.613216
H	-7.34348	-5.32767	-0.30205
H	-7.20748	-5.29209	1.467389
H	-8.80262	-5.28805	0.699929
C	8.751824	-2.30716	-0.65885
H	8.662816	-1.21718	-0.69407
H	9.81568	-2.56366	-0.59271
H	8.369121	-2.70944	-1.60538
C	8.55499	-2.32536	1.85816
H	8.030122	-2.74131	2.727531
H	9.616544	-2.58186	1.954476
H	8.460176	-1.23589	1.895378
C	8.085425	-4.42231	0.540341
H	7.541913	-4.8647	1.384634
H	7.682518	-4.85223	-0.38529
H	9.133137	-4.73352	0.621089
C	8.585925	2.869369	-0.63219
H	9.629757	3.197639	-0.56227
H	8.57303	1.776703	-0.69079
H	8.173206	3.263939	-1.56926
C	8.395513	2.820163	1.884699
H	7.844443	3.178588	2.763365
H	8.377889	1.726111	1.897765
H	9.43657	3.148749	1.986123
C	7.778532	4.907342	0.613216
H	7.343478	5.327672	-0.30205
H	7.207482	5.292086	1.467389
H	8.802618	5.288049	0.699929

Cartesian coordinate of **9c**.

9c	**Coordinates (Å)**		
Element	*x*	*y*	*z*
C	-0.04107	9.352236	-0.62226
C	1.334175	9.059712	-0.60323
C	1.787538	7.745747	-0.49165
C	0.839168	6.724034	-0.39859
C	-0.53832	7.010505	-0.41728
C	-0.98807	8.311291	-0.52821
C	-0.5579	10.73884	-0.73946
O	-1.73975	11.03548	-0.76278
O	0.430993	11.66271	-0.81936
N	1.092636	5.355565	-0.28073
C	-0.05857	4.730023	-0.22066
C	-1.2793	5.690048	-0.29768
C	-0.09681	3.277123	-0.09323
C	-1.30452	2.55791	-0.02759
C	1.157017	2.618199	-0.02605
N	-1.42304	1.246106	0.072326
N	1.349012	1.323439	0.074129
C	-2.68988	0.62378	0.159415

C	-2.65142	-0.77414	0.161405
N	-1.34901	-1.32344	0.074129
C	-1.15702	-2.6182	-0.02605
C	0.096806	-3.27712	-0.09323
C	1.304519	-2.55791	-0.02759
N	1.423043	-1.24611	0.072326
C	2.651418	0.774139	0.161405
C	2.689876	-0.62378	0.159415
C	-3.84567	-1.51139	0.254134
C	-5.07149	-0.86272	0.335376
C	-5.11394	0.559467	0.331703
C	-3.93033	1.283835	0.248368
C	3.845673	1.511385	0.254134
C	5.071489	0.862716	0.335376
C	5.113935	-0.55947	0.331703
C	3.930326	-1.28384	0.248368
C	0.041072	-9.35224	-0.62226
C	-1.33418	-9.05971	-0.60323
C	-1.78754	-7.74575	-0.49165
C	-0.83917	-6.72403	-0.39859
C	0.538315	-7.01051	-0.41728
C	0.988074	-8.31129	-0.52821
C	0.557904	-10.7388	-0.73946
O	-0.43099	-11.6627	-0.81936
O	1.739753	-11.0355	-0.76278
N	-1.09264	-5.35557	-0.28073
C	0.058574	-4.73002	-0.22066
C	1.279303	-5.69005	-0.29768
C	-2.13094	5.679934	0.994207
C	-2.1494	5.455896	-1.55525
C	2.130938	-5.67993	0.994207
C	2.149399	-5.4559	-1.55525
H	2.045365	9.874778	-0.67677
H	2.84789	7.513492	-0.47662
H	-2.04302	8.569628	-0.54578
H	-2.22264	3.130644	-0.06403
H	2.016524	3.281248	-0.06569
H	-2.01652	-3.28125	-0.06569
H	2.222638	-3.13064	-0.06403
H	-3.81851	-2.59195	0.272937
H	-3.97785	2.363838	0.266061
H	3.818511	2.591947	0.272937
H	3.977845	-2.36384	0.266061
H	-2.04537	-9.87478	-0.67677
H	-2.84789	-7.51349	-0.47662
H	2.043023	-8.56963	-0.54578
H	-2.66667	4.736028	1.136734
H	-2.87473	6.483375	0.951807
H	-1.50376	5.847644	1.875523
H	-2.69392	4.506844	-1.51947
H	-1.53418	5.457856	-2.46063
H	-2.88739	6.260577	-1.6476

H	2.66667	-4.73603	1.136734
H	2.874727	-6.48338	0.951807
H	1.503755	-5.84764	1.875523
H	2.693919	-4.50684	-1.51947
H	1.534182	-5.45786	-2.46063
H	2.88739	-6.26058	-1.6476
C	0	-13.0339	-0.93516
H	0.63026	-13.282	-0.0748
H	0.616961	-13.1373	-1.83402
C	-1.2453	-13.8996	-0.99754
H	-1.8635	-13.6342	-1.86143
H	-0.96187	-14.9541	-1.08754
H	-1.8497	-13.7815	-0.0922
C	0	13.03389	-0.93516
H	-0.61696	13.13735	-1.83402
H	-0.63026	13.28197	-0.0748
C	1.245301	13.89961	-0.99754
H	0.961867	14.95411	-1.08754
H	1.849698	13.78145	-0.0922
H	1.863497	13.6342	-1.86143
Ni	0	0	0.076974
O	6.355451	-1.10506	0.423387
O	6.277104	1.482477	0.432721
O	-6.2771	-1.48248	0.432721
O	-6.35545	1.105064	0.423387
C	6.491358	-2.52366	0.429725
H	5.933367	-2.94487	1.279875
H	6.068159	-2.93879	-0.49774
C	-6.49136	2.523656	0.429725
H	-5.93337	2.944868	1.279875
H	-6.06816	2.938793	-0.49774
C	-6.31848	-2.90812	0.463632
H	-5.86713	-3.3105	-0.45561
H	-5.73408	-3.27487	1.320742
C	6.318478	2.908116	0.463632
H	5.86713	3.310497	-0.45561
H	5.734082	3.274872	1.320742
C	7.981191	-2.88539	0.542948
C	-7.98119	2.885394	0.542948
C	7.780561	3.367051	0.582713
C	-7.78056	-3.36705	0.582713
C	-8.08543	4.422309	0.540341
H	-7.54191	4.864703	1.384634
H	-7.68252	4.852231	-0.38529
H	-9.13314	4.733524	0.621089
C	-8.75182	2.307163	-0.65885
H	-8.36912	2.709441	-1.60538
H	-8.66282	1.217181	-0.69407
H	-9.81568	2.56366	-0.59271
C	-8.55499	2.325363	1.85816
H	-8.46018	1.235888	1.895378
H	-8.03012	2.741309	2.727531

H	-9.61654	2.581859	1.954476
C	-8.39551	-2.82016	1.884699
H	-8.37789	-1.72611	1.897765
H	-9.43657	-3.14875	1.986123
H	-7.84444	-3.17859	2.763365
C	-8.58593	-2.86937	-0.63219
H	-9.62976	-3.19764	-0.56227
H	-8.57303	-1.7767	-0.69079
H	-8.17321	-3.26394	-1.56926
C	-7.77853	-4.90734	0.613216
H	-7.34348	-5.32767	-0.30205
H	-7.20748	-5.29209	1.467389
H	-8.80262	-5.28805	0.699929
C	8.751824	-2.30716	-0.65885
H	8.662816	-1.21718	-0.69407
H	9.81568	-2.56366	-0.59271
H	8.369121	-2.70944	-1.60538
C	8.55499	-2.32536	1.85816
H	8.030122	-2.74131	2.727531
H	9.616544	-2.58186	1.954476
H	8.460176	-1.23589	1.895378
C	8.085425	-4.42231	0.540341
H	7.541913	-4.8647	1.384634
H	7.682518	-4.85223	-0.38529
H	9.133137	-4.73352	0.621089
C	8.585925	2.869369	-0.63219
H	9.629757	3.197639	-0.56227
H	8.57303	1.776703	-0.69079
H	8.173206	3.263939	-1.56926
C	8.395513	2.820163	1.884699
H	7.844443	3.178588	2.763365
H	8.377889	1.726111	1.897765
H	9.43657	3.148749	1.986123
C	7.778532	4.907342	0.613216
H	7.343478	5.327672	-0.30205
H	7.207482	5.292086	1.467389
H	8.802618	5.288049	0.699929